SCENARIOS OF PHYSICS BEYOND THE STANDARD MODEL

by

RICKY FOK

A DISSERTATION

Presented to the Department of Physics
and the Graduate School of the University of Oregon
in partial fulfillment of the requirements
for the degree of
Doctor of Philosophy

September 2011

DISSERTATION APPROVAL PAGE

Student: Ricky Fok

Title: Scenarios of Physics Beyond the Standard Model

This dissertation has been accepted and approved in partial fulfillment of the requirements for the Doctor of Philosophy degree in the Department of Physics by:

Dr. Davison Soper	Chair
Dr. Graham Kribs	Advisor
Dr. Ray Frey	Member
Dr. Michael Kellman	Outside Member

and

Kimberly Andrews Espy	Vice President for Research & Innovation/ Dean of the Graduate School

Original approval signatures are on file with the University of Oregon Graduate School.

Degree awarded September 2011

DISSERTATION ABSTRACT

Ricky Fok

Doctor of Philosophy

Department of Physics

September 2011

Title: Scenarios of Physics Beyond the Standard Model

Approved: _____
                    Dr. Graham Kribs

This dissertation discusses three topics on scenarios beyond the Standard Model.

Topic one is the effects from a fourth generation of quarks and leptons on electroweak baryogenesis in the early universe. The Standard Model is incapable of electroweak baryogenesis due to an insufficiently strong enough electroweak phase transition (EWPT) as well as insufficient CP violation. We show that the presence of heavy fourth generation fermions solves the first problem but requires additional bosons to be included to stabilize the electroweak vacuum. Introducing supersymmetric partners of the heavy fermions, we find that the EWPT can be made strong enough and new sources of CP violation are present.

Topic two relates to the lepton flavor problem in supersymmetry. In the Minimal Supersymmetric Standard Model (MSSM), the off-diagonal elements in the slepton mass matrix must be suppressed at the 10^{-3} level to avoid experimental bounds from lepton flavor changing processes. This dissertation shows that an enlarged R-parity can alleviate the lepton flavor problem. An analysis of all sensitive parameters was performed in the mass range below 1 TeV, and we find that slepton maximal

mixing is possible without violating bounds from the lepton flavor changing processes: $\mu \to e\gamma, \mu \to e$ conversion, and $\mu \to 3e$.

Topic three is the collider phenomenology of quirky dark matter. In this model, quirks are particles that are gauged under the electroweak group, as well as a "dark" color $SU(2)$ group. The hadronization scale of this color group is well below the quirk masses. As a result, the dark color strings never break. Quirk and anti-quirk pairs can be produced at the LHC. Once produced, they immediately form a bound state of high angular momentum. The quirk pair rapidly shed angular momentum by emitting soft radiation before they annihilate into observable signals. This dissertation presents the decay branching ratios of quirkonia where quirks obtain their masses through electroweak symmetry breaking.

This dissertation includes previously published and unpublished co-authored material.

<center>CURRICULUM VITAE</center>

NAME OF AUTHOR: Ricky Fok

GRADUATE AND UNDERGRADUATE SCHOOLS ATTENDED:
    University of Oregon, Eugene, Oregon
    University of Sydney, Australia

DEGREES AWARDED:
    Doctor of Philosophy in Physics, 2011, University of Oregon
    Bachelor of Science in Physics, 2003, University of Sydney

AREAS OF SPECIAL INTEREST:
    Particle Physics

PROFESSIONAL EXPERIENCE:

    Research Assistant,
      Theoretical High-Energy Group, University of Oregon, 06/2007 - Current

    Teaching Assistant
      Univeristy of Oregon, 09/2005 - 06/2007

GRANTS, AWARDS AND HONORS:

    Summer Research Scholarship, University of Sydney, 2002/2003

    Summer Research Scholarship, University of Sydney, 2003/2004

PUBLICATIONS:

    R. Fok and G. D. Kribs,"$\mu \rightarrow e$ in R-symmetric Supersymmetry," Phys. Rev.
    D **82**, 035010 (2010) [arXiv:1004.0556 [hep-ph]].

R. Fok and G. D. Kribs, "Four Generations, the Electroweak Phase Transition, and Supersymmetry," Phys. Rev. D **78**, 075023 (2008) [arXiv:0803.4207]

D. B. Melrose, R. Fok and D. P. Menezes, Mon. Not. Roy. Astron. Soc. **371**, 204 (2006) [arXiv:astro-ph/0607553].

ACKNOWLEDGEMENTS

I would like to thank Graham Kribs for being an excellent advisor. Without his assistance, I would have been in downtown Chicago asking rich people for change, rather than performing postdoctoral research in the murder capital of Toronto. I would also like to thank those who attempted to make this world a better place for me.

TABLE OF CONTENTS

LIST OF FIGURES

LIST OF TABLES

CHAPTER I

INTRODUCTION: THE NEED FOR NEW PHYSICS

Even though the Standard Model gives an accurate picture of Nature thus far, it cannot be the complete description of Nature. The missing piece of the puzzle is related to the mechanism that generates fermion and gauge boson masses. In the Standard Model this is achieved by introducing the Higgs scalar. The Higgs field breaks electroweak symmetry spontaneously, acquiring a non-zero vacuum expectation value (VEV). The fermions then receive masses via their interactions with the Higgs field. Even if the Higgs exists, unknown physics must exist at a scale not far above the electroweak scale for our description to be natural, in the sense of [1]. This places the Standard Model in a theoretically awkward position; the theory describing electroweak physics is very likely dependent on unknown physics not far above the electroweak scale. In the literature, this unnaturalness is usually called "the Hierarchy Problem". It can be understood in terms of the perturbativity of the Higgs sector. Consider the Standard Model Higgs potential,

$$V = -m_H^2 \phi^2 + \lambda \phi^4, \tag{1.1}$$

where m_H is the Higgs mass, ϕ is the Higgs field. The VEV, v, measured to be 246 GeV, is

$$v = \sqrt{\frac{m_H^2}{2\lambda}}. \tag{1.2}$$

If we require the theory to be perturbative, then $\lambda \lesssim O(1)$, implying the Higgs mass is less than 350 GeV. However, the Higgs mass receives quantum corrections from, notably, its interactions with itself and the top quark. At one loop level, with $\lambda \sim O(1)$, the largest contribution comes from the top, due to its color enhancement factor of $N_c = 3$,

$$\delta m_H^2 = \frac{N_c y_t^2}{8\pi^2} \Lambda_{NP}^2,$$

(1.3)

where $y_t \sim 1$ is the top yukawa, Λ_{NP} is the scale of new physics. Perturbativity requires $m_H^2 \lesssim \delta m_H^2$. One finds $\Lambda_{NP} \sim O(\text{TeV})$. This implies two possibilities. First, we could allow non-perturbative physics above Λ_{NP}. We will not consider this scenario. Second, there exists new physics at a scale of order 1 TeV to reduce the size of loop corrections to the Higgs mass. An example of new physics is supersymmetry, a symmetry between fermions and bosons. This introduces a bosonic partner to each fermion, and vice versa. Therefore, for each fermion loop contributing to the Higgs mass, there is a corresponding bosonic loop (almost) canceling the contribution from the fermion, rendering the correction small.

This dissertation contains a study of various scenarios of new physics and their implications on observable phenomena. This chapter reviews the physics that will be discussed in the following chapters. Section 1.1. presents a mechanism which generates baryons during the early universe, through an electroweak phase transition. Section 1.2. gives a brief introduction to supersymmetry and lepton flavor violation. Section 1.3. discusses the physics of quirks. Then, an outline of the following chapters is given in section 1.4..

1.1. Electroweak Baryogenesis

Electroweak baryogenesis is a mechanism to generate baryon number through the electroweak phase transition in the early universe. It requires many ingredients. The most relevant to this disseration is: a description of the breaking of electroweak symmetry as the universe cools down. This involves the calculation of the effective potential at finite temperature. A detailed review of electroweak baryogenesis is given in [2]. Here is a summary of the relevant physics for the subsequent sections.

1.1.1. Conditions for Electroweak Baryogenesis

These three conditions, formulated by Sakharov [3], must be satisfied for electroweak baryogenesis (EWB) to proceed:

- Baryon number violation

- C and CP violation

- Out of thermal equilibrium

Baryon number violation can proceed through the chiral anomaly of the weak $SU(2)_L$ group. The anomaly gives a non-zero divergence of the baryon current.[1]

$$\partial_\mu j_B^\mu = \frac{N_f g^2}{32\pi^2} F\tilde{F},\tag{1.4}$$

where N_f is the number of fermion generations, and $F\tilde{F}$ can also be written as a divergence,

---

[1]Neglecting the $U(1)_Y$ contribution as it does not involve in the baryon number violation process, since $U(1)_Y$ does not contain the axial-vector interaction with fermions which leads to the violation of baryon number.

$$F\tilde{F} = \partial_\mu \epsilon^{\mu\nu\rho\sigma} \left(F^a_{\nu\rho} A^a_\sigma - \frac{g}{3} \epsilon_{abc} A^a_\nu A^b_\rho A^c_\sigma \right). \tag{1.5}$$

The second term in equation (1.5) is related to the baryon violating process in vacuum, where $F^a_{\nu\rho} = 0$, while the first term gives no contributions as it is proportional to the field strength tensor. Consider all field configurations A^a_μ corresponding to zero field strength, and choose the temporal gauge, $A^a_0 = 0$. Then, integrating equation (1.4) over all spacetime gives the change of baryon number from $t = -\infty$ to $t = \infty$,

$$\Delta B = N_f \Delta N_{CS}, \tag{1.6}$$

where N_{CS} is the Chern-Simons number corresponding to the topology of the gauge field,

$$N_{CS} = -\frac{g^3}{96\pi^2} \int d^3x \epsilon^{ijk} \epsilon_{abc} A^a_i A^b_j A^c_k. \tag{1.7}$$

Therefore, the topology of the gauge field must change for baryon number violation to occur. In the space of all gauge field configurations, there are infinite numbers of degenerate vacua corresponding to $F_{\mu\nu} = 0$, each with a different Chern-Simons number. Each vacuum is separated by an energy barrier. In Euclidean spacetime, the path connecting two vacua with $\Delta N_{CS} = 1$ is called the instanton. The unstable classical solution for the field configuration at the top of barrier with energy E_{sph} is called the sphaleron. At zero temperature, the probability of tunneling through the potential barrier via the instanton is $\sim \exp(-4\pi/\alpha_W) \sim 10^{-162}$, essentially zero. However, at finite temperature, the suppression factor is replaced by the Boltzmann factor, $\exp(-E_{sph}/T)$. From this factor, it is shown in [2] that in order to prevent too

4

many of the baryons from being washed out, during the electroweak phase transition, the criterion $\phi_c/T_c \gtrsim 1$, must be satisfied, where ϕ_c is the VEV of the electroweak broken vacuum at the temperature T_c where it is degenerate with the symmetric vacuum. This also implies that the phase transition must be of first order, because $\phi_c/T_c \sim 0$ for a second order phase transition.

The Standard Model contains C and CP violating interactions, and in principle, could satisfy the second condition. However, the CP violation provided by the Standard Model generally considered to be too small. New physics must be introduced to produce sufficient CP violation for electroweak baryogenesis [2].

The third condition, out of thermal equilibrium, can be realized in a first order phase transition. In this case, there is an energy barrier separating the electroweak symmetric and broken vacua near the critical tempeature T_c. As a result, the symmetric vacuum is supercooled, bubbles of electroweak broken vacuum start to nucleate, and expand throughout the universe during the phase transition. Baryon number violating processes are out of equilibrium if they occur inside the bubble walls as they propagate out [4]. In the following sections, it will be shown that the electroweak phase transition from the Standard Model is too weak to prevent the washout of baryons, even if a mechanism were present to generate them.

1.1.2. The 1-loop Effective Potential at Finite Temperature

To understand the electroweak phase transition, the behavior of the Higgs potential at high temperatures must be understood. The formalism of field theory at finite temperature is discussed in detail in [2, 5]. It describes interactions of particles with the thermal bath at temperature T. In comparison to field theory at zero temperature, the expectation value of operators at zero temperature is replaced by

the grand canonical average of the operators, $\langle O \rangle = Tr(\rho O)$, where ρ is the grand canonical density operator

$$\rho = \frac{\exp[\sum_i \beta \mu_i Q_i - \beta H]}{Tr \exp[\sum_i \beta \mu_i Q_i - \beta H]}, \tag{1.8}$$

where the trace is over all states in the ensemble, the sum is over all species in the thermal bath, μ_i is the chemical potential of species i, $\beta = 1/T$, and H is the Hamiltonian. One sees that $Tr(\rho) = 1$, as expected. Once $\langle O \rangle$ is identified with the grand canonical average, the generating function and the n-point Green's function can be defined analogously to their counterparts at zero temperature. And the effective potential at finite temperature can be calculated in the same way, only with modified Feynman rules.

The thermal properties of the theory are manifest in the two-point Green's function. Only real scalar fields are considered in the following discussion. For fermionic fields the formalism is similar and is discussed in [2] – In many cases the results for fermionic fields differ from the bosonic cases only by a sign. The following text will keep track of this sign when appropriate.

Separating into the advanced and retarded Green's functions,

$$G_C(x - y) = \theta_C(x^0 - y^0)G_+(x - y) + \theta_C(y^0 - x^0)G_-(x - y), \tag{1.9}$$

where $G_+(x - y) = \langle \phi(x)\phi(y) \rangle$ and $\theta_C(t)$ is a to-be-determined function with contour C in the complex t plane. The retarded Green's function satisfy $G_-(x - y) = G_+(y - x)$. Using $\phi(x) = e^{ix_0 H}\phi(0, \mathbf{x})e^{-ix_0 H}$, and taking $\mu_i = 0$, $\mathbf{x} = 0$ for simplicity, the advanced Green's function is

$$G_+(x-y) = \frac{1}{N} \sum_{m,n} |\langle m|\phi(0)|n\rangle|^2 \exp[iE_m(x^0 - y^0 + i\beta)] \exp[-iE_n(x^0 - y^0)], \quad (1.10)$$

where $|m\rangle$ and $|n\rangle$ are the eigenstates of Hamiltonian with eigenvalues E_m and E_n respectively, and N is the normalization constant of the grand canonical partition function ρ. To ensure convergence, we see that $-\beta < Im(t) < 0$. Therefore, $\theta_C(t)$ must vanish outside of this range to ensure that the advanced Green's function converges for all t. The same analysis can be done for the retarded Green's function $G_-(t)$ and the result is similar. This is summarized in figure 1.1. In addition, advanced and retarded Green's functions are related for both bosonic and fermionic fields, it is

$$G_+(t - i\beta, \mathbf{x}) = \eta G_-(t, \mathbf{x}), \quad (1.11)$$

where $\eta = +1$ for bosons, and -1 for fermions. This is the Kubo-Martin-Schwinger relation [6, 7]. Now, choose a contour C to be on the imaginary axis, and parametrize $t = -i\tau$, $\tau \in (0, \beta)$. Write the above as $G_-(-t + i\beta) = \eta G_-(t)$. Then, one sees that the retarded Green's function is symmetric for bosons and anti-periodic for fermions about the midpoint of 0 and $i\beta$. A similar argument holds for the advanced Green's function which is valid in the strip $(0, -i\beta)$. One can then analytically continue the Green's function to the whole complex t plane, with period β in Euclidean time. As the observables are proportional to the square of amplitudes, this implies that the observables return to its original value after a time scale set by the inverse of the temperature, consistent with thermal equilibrium.
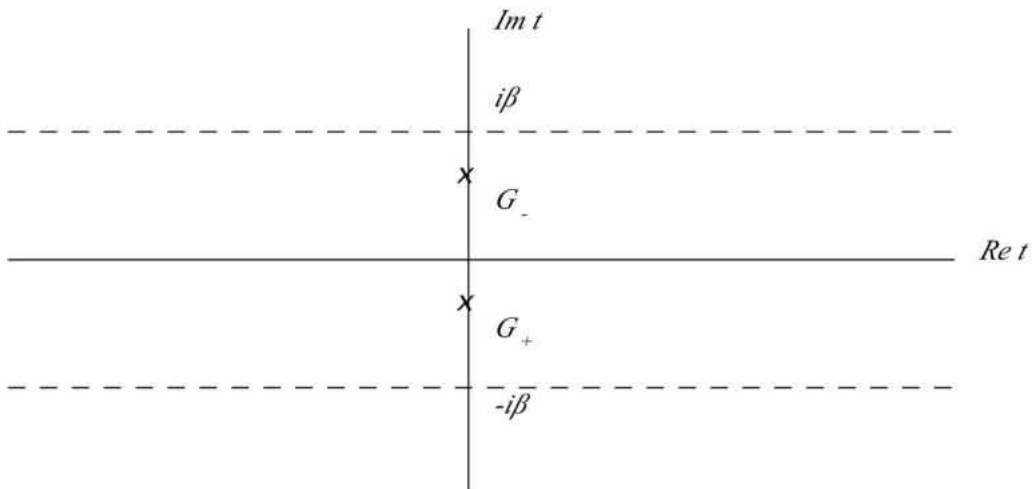
FIGURE 1.1: The region of convergence for $G_-(x-y)$ and $G_+(x-y)$ in the complex t plane. The crosses on the imaginary axis denotes the points related by the periodicity condition $G_+(t-i\beta, \mathbf{x}) = \eta G_-(t, \mathbf{x})$. The region of convergence for $G_-(x-y)$ is in the region between the top dashed line and the real axis. The strip below the real axis is the region of convergence for $G_+(x-y)$.

We are now in a position to write the two-point Green's function in a more illuminating form and derive the thermal Feynman rules for real scalar fields. First, expand the scalar field into creation and annihilation operators and define the Hamiltonian of the system (consisting of n scalar fields in a thermal bath) to be

$$H = \int \frac{d^3\mathbf{p}}{(2\pi)^3} \omega_p N \tag{1.12}$$

where $\omega_p = \sqrt{\mathbf{p}^2 + m^2}$ and $N = a^\dagger a$ is the number operator. Then, consider a state where n scalars have energy ω and call this state $|n\rangle$. The annihilation and creation operators act on this state. In this basis, the ensemble averages corresponding to the number operator N can be computed, $\langle a_{\mathbf{q}}^\dagger a_{\mathbf{p}} \rangle = n_B(\omega_{\mathbf{p}})\delta^3(\mathbf{q} - \mathbf{p})$ and $\langle a_{\mathbf{q}} a_{\mathbf{p}}^\dagger \rangle = [1 + n_B](\omega_{\mathbf{p}})\delta^3(\mathbf{q} - \mathbf{p})$, where n_B is the Bose distribution

8

$$n_B = \frac{1}{e^{\beta \omega_p} - 1}. \tag{1.13}$$

Then the Green's function can be written in a form that contains a vacuum term and a thermal term explicitly

$$G_C(x - y) = \int \frac{d^4 p}{(2\pi)^4} \rho(p) e^{-ip(x-y)} [\theta_C(x^0 - y^0) + n_B(p^0)], \tag{1.14}$$

where $\rho = 2\pi [\theta(p^0) - \theta(-p^0)] \delta(p^2 - m^2)$. To find the Green's function in momentum space, the contour C is chosen to be on the imaginary axis, it is

$$G(\omega_n, \mathbf{p}) = \frac{1}{\mathbf{p}^2 + m^2 + \omega_l^2}, \tag{1.15}$$

where $\omega_l = 2l\pi\beta^{-1}$. This is the Matsubara frequency [8]. The derivation for other modifications to the Feynman rules can be found in [5]. Here is a summary

Boson propagator	$\dfrac{-i}{\mathbf{p}^2 + m^2 + [2l\pi\beta^{-1}]^2}$
Fermion propagator	$\dfrac{-i}{\mathbf{p}^2 + m^2 + [(2l+1)\pi\beta^{-1}]^2}$
Loop integral	$\dfrac{i}{\beta} \displaystyle\sum_{n=-\infty}^{\infty} \int \frac{d^3\mathbf{p}}{(2\pi)^3}$
Vertex function	$-i\beta(2\pi)^3 \delta(\sum_i l_i) \delta^3(\sum_i \mathbf{p_i}),$

where the delta functions in the vertex function corresponds to the conservation of Matsubara frequency and momentum. Comparing to zero temperature Feynman rules, the loop integral over the temporal component of the loop momentum is replaced by a sum over Matsubara modes l_i. Also, the phase space volume $(2\pi)^4$

is replaced by $\beta(2\pi)^3$. Using this set of modifications to the Feynman rules and coupling constants from the Lagrangian it is sufficient to calculate the 1-loop effective potential for the Higgs field at finite temerpature.

Remarkably, the zero temperature and the finite temperature contributions can be separated in the 1-loop effective potential,

$$V_{eff}(\phi, T) = V_0(\phi, 0) + V_1(\phi, 0) + V_T(\phi, T), \tag{1.16}$$

where

$$V_0(\phi, 0) = -\frac{m^2}{2}\phi^2 + \frac{\lambda}{4}\phi^4 \tag{1.17}$$

is the tree level potential,

$$V_1(\phi, 0) + \delta V = \frac{1}{64\pi^2} \sum_i n_i \left[m_i^4(\phi) \left(\log \frac{m_i^2(\phi)}{m_i^2(v)} - \frac{3}{2} \right) + 2m_i^2(\phi)m_i^2(v) \right] \tag{1.18}$$

is the 1-loop correction term [9] with the counterterms δV determined by the cutoff regularization and the following renormalization conditions:

$$\left. \frac{d(V_1 + \delta V)}{d\phi} \right|_{\phi=v} = 0, \qquad \left. \frac{d^2(V_1 + \delta V)}{d\phi^2} \right|_{\phi=v} = 0, \tag{1.19}$$

with $v = 246$ GeV being the zero temperature VEV. The sum is over relevant particle species with number of degrees of freedom n_i (the convention I use here is such that for a fermion f, n_f is negative due to the fermion loop). The field dependent mass squared for species i is $m_i^2(\phi) = d^2V_0/d\phi^2$. Finally, the thermal contribution to the effective potential is

$$V_T(\phi, T) = \sum_i n_i \frac{T^4}{2\pi^2} J_\pm\left(\frac{m_i^2(\phi)}{T^2}\right), \tag{1.20}$$

10

where

$$J_{\pm}\left(\frac{m_i^2(\phi)}{T^2}\right) = \int_0^{\infty} dx \ x^2 \log\left[1 \pm e^{-\sqrt{x^2 + m_i^2(\phi)/T^2}}\right], \tag{1.21}$$

with $+$ for fermions and $-$ for bosons. The functions $J_{\pm}$ can be expanded in the limit where $m^2/T \to 0$, where the ϕ dependence on m has been neglected for convenience. The result is [2]

$$J_-\left(\frac{m^2}{T^2}\right) = -\frac{\pi^4}{45} + \frac{\pi^2}{12}\frac{m^2}{T^2} - \frac{\pi}{6}\frac{m^3}{T^3} - \frac{1}{32}\frac{m^4}{T^4}\log\frac{m^2}{a_b T^2} + O\left(\frac{m^6}{T^6}\right), \quad \text{and}$$

$$\tag{1.22}$$

$$J_+\left(\frac{m^2}{T^2}\right) = \frac{7}{8}\frac{\pi^4}{45} - \frac{\pi^2}{24}\frac{m^2}{T^2} - \frac{1}{32}\frac{m^4}{T^4}\log\frac{m^2}{a_f T^2} + O\left(\frac{m^6}{T^6}\right), \tag{1.23}$$

with $\log a_b = 3/2 - 2\gamma_E + 2\log 4\pi = 5.4076$ and $\log a_f = 3/2 - 2\gamma_E + 2\log\pi = 2.6351$. The constant term in $J_{\pm}$ corresponds to the free energy of a boson or fermion gas, respectively. Figure 1.2 shows the 1-loop effective potential at different temperatures for a four generation supersymmetric standard model that will be considered in chapter III. At zero temperature, the VEV of the Higgs field is fixed at 246 GeV. At higher temperatures, the VEV becomes smaller, and eventually becomes zero at sufficiently high temperatures - the electroweak symmetry is restored. This phenomenon is called symmetry restoration.

1.1.3. Electroweak Phase Transition for the Standard Model

To avoid washout of excess baryons after the electroweak phase transition, the phase transition must be sufficiently strong. This is parametrized by the criterion $\phi_c/T_c \gtrsim 1$ [2], where the critical temperature T_c is the temperature at which the two minima are degenerate, and ϕ_c is the value of ϕ at the degenerate minimum. In
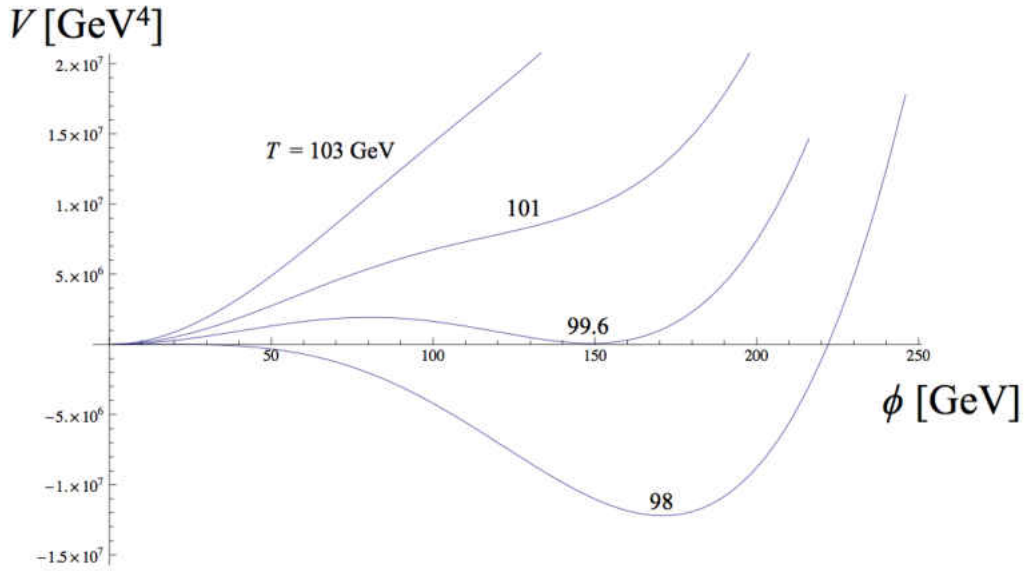
FIGURE 1.2: An illustration of the 1-loop effective Higgs potential at different temperatures. The zero point energy of the potential at $\phi = 0$ has been shifted to be zero. In this case, the electroweak phase transition occurs at $T_c = 99.6$ GeV, when a degenerate vacuum is developed at $\phi \neq 0$. Above that temperature the absolute minimum of the potential is at $\phi = 0$, the electroweak unbroken vacuum. Notice that there is a potential barrier between the electroweak symmetric vacuum and the electroweak broken vacuum at $T = T_c$, a characteristic feature of first order phase transitions.

the Standard Model, the order parameter ϕ_c/T_c can be calculated analytically in the high temperature limit of the 1-loop potential, equations (1.20) and (1.21), which is [2]

$$V_{eff}(\phi, T) = D(T^2 - T_0^2)\phi^2 - ET\phi^3 + \frac{\lambda(T)}{4}\phi^4, \tag{1.24}$$

where

$$D = \frac{2m_W^2 + m_Z^2 + 2m_t^2}{8v^2} \tag{1.25}$$

$$E = \frac{6m_W^3 + 3m_Z^3}{12\pi v^3} \tag{1.26}$$

$$B = \frac{3}{64\pi^2 v^4}(2m_W^4 + m_Z^4 - 4m_t^4) \tag{1.27}$$

$$T_0^2 = \frac{m_h^2 - 8Bv^2}{4D} \tag{1.28}$$

$$\lambda(T) = \lambda - \frac{1}{16\pi^2 v^4}\left(6m_W^4 \log\frac{m_W^2}{A_B T^2} + 3m_Z^4 \log\frac{m_Z^2}{A_B T^2} - 12m_t^4 \log\frac{m_t^2}{A_F T^2}\right), \tag{1.29}$$

where $A_B = -2\gamma_E + 2\log 4\pi$ and $A_F = -2\gamma_E + 2\log\pi$. This gives

$$\frac{\phi_c}{T_c} = \frac{2E}{\lambda(T)} \sim O(0.1), \tag{1.30}$$

for Higgs mass $m_h = O(100)$ GeV. The electroweak phase transition from the Standard Model is too weak to be able to explain the observed baryon asymmetry today. In chapter II, we will see how this can be modified by including a fourth generation of chiral fermions supersymmetry.

1.2. Supersymmetry and the Lepton Flavor Problem

Supersymmetry is a symmetry that relates the bosonic and fermionic degrees of freedom. A supersymmetric Lagrangian must contain the same number of bosonic and fermionic degrees of freedom. Among supersymmetry's many virtues, weak scale supersymmetry leads to a solution to the Higgs hierarchy problem; each scalar loop giving large radiative corrections to the Higgs mass is canceled by a corresponding fermion loop. This section reviews the structure of a supersymmetric Lagrangian, the simplest supersymmetric extension of the Standard Model, and a brief review on the lepton flavor problem. The formalism of supersymmetry in this section follows closely to the lectures given by N. Arkani-Hamed [10]. Other reviews on supersymmetry include [11] and [12].

1.2.1. Supersymmetric Lagrangian

In a supersymmetric theory, a field with its corresponding superpartner can be written in a single superfield. A supersymmetric Lagrangian can be written in terms of superfields, an element in the superspace. The coordinates of the superspace can be written in terms of Grassmann numbers and their conjugates $\{\theta^\alpha, \bar{\theta}^\alpha\}$, with $\alpha = 1, 2$.

We consider two types of superfields, chiral superfields and vector superfields in the Wess-Zumino gauge. A chiral superfield X with scalar component ϕ and fermion component ψ is

$$X = \phi + \sqrt{2}\theta_\alpha \psi^\alpha + \theta^2 F, \tag{1.31}$$

where F is an auxiliary field, and $\theta_\alpha \psi^\alpha = \epsilon_{\alpha\beta}\theta^\alpha \psi^\beta$. It is replaced by its classical solution to the equation of motion in the Lagrangian, resulting in interaction terms

among the scalar ϕ. The kinetic terms for ϕ and ψ can be derived from

$$\int d^4\theta X^\dagger X, \tag{1.32}$$

to get derivative terms from the above, write $\phi = \phi(y^\mu) = \phi(x^\mu + i\theta\sigma^\mu\bar\theta)$, and expand in $i\theta\sigma^\mu\bar\theta$. Similarly for ψ. The supersymmetric Lagrangian is then

$$\partial^\mu\phi^\dagger\partial_\mu\phi + i\psi^\dagger\bar\sigma^\mu\partial_\mu\psi + F^\dagger F. \tag{1.33}$$

This is called the Wess-Zumino Lagrangian. The auxiliary field F does not have a kinetic term and it can be 'integrated out' and be replaced by its solution to the classical equation of motion. Then, the F-term $F^\dagger F$ can be written as a polynomials in ϕ.

In order to include gauge bosons and their interactions to the Lagrangian, vector superfields must be included. We consider vector superfields in the Wess-Zumino gauge. A vector superfield, V, with a vector field v_μ, a fermion field and its conjugate $\lambda, \lambda^\dagger$, and an auxiliary field D, is

$$V^a = \theta\sigma^\mu\bar\theta v_\mu^a + i\theta^2\bar\theta\lambda^{\dagger a} - i\bar\theta^2\theta\lambda^a + \frac{1}{2}\theta^2\bar\theta^2 D^a, \tag{1.34}$$

where a is a guage index. The interactions between chiral superfields and vector superfields are contained in the gauge invariant term

$$\int d^4\theta \bar{X} e^{2gV^a\tau^a} X, \tag{1.35}$$

15

where τ^a is a generator of the gauge group. In component form, the above is

$$|D_\mu\phi|^2 + i\psi^\dagger\bar{\sigma}^\mu D_\mu\psi + F^\dagger F + i\sqrt{2}g(\phi^\dagger\tau^a\psi\lambda^a - \phi\tau^a\psi^\dagger\lambda^{\dagger a}) + g\phi^\dagger\tau^a\phi D^a. \qquad (1.36)$$

The above contains the usual covariant derivatives of the scalar and the fermion, as well as interaction terms that have no counterparts in the Standard model, $i\sqrt{2}g\phi^\dagger\tau^a\psi\lambda^a + c.c.$. These terms describe the interaction between the gaugino, fermion and sfermion, the superpartner of the fermion. The last term consists of the auxiliary field D^a, which will be integrated out.

All that remains is to find a supersymmetric term that describes the propagation of gauge bosons. To do this, we need to form a field strength chiral superfield from the vector superfield. The result is

$$W_\alpha^a = 4i\lambda_\alpha^a + [4\delta_\alpha^\beta D^a + 2i(\sigma^\mu\bar{\sigma}^\nu)_\alpha^\beta F_{\mu\nu}^a]\theta_\beta + 4\theta^2\sigma_{\alpha\dot{\alpha}}D_\mu\lambda^{a\dot{\alpha}}. \qquad (1.37)$$

The field strength term can be formed by integrating over W^aW^a, this term is called the superpotential.

$$\int d^2\theta^2 \frac{1}{64}W^aW^a + \int d^2\bar{\theta}^2 \frac{1}{64}W^{\dagger a}W^{\dagger a}. \qquad (1.38)$$

In component form, it is

$$-\frac{1}{4}F_{\mu\nu}^a F^{a\mu\nu} + i\lambda^{\dagger a}\bar{\sigma}^\mu D_\mu\lambda^a + \frac{1}{2}D^aD^a. \qquad (1.39)$$

The above includes the kinetic term for the gauge boson and the gauginos, and a D-term. A supersymmetric fermion mass term can also be included in the

superpotential. The superpotential for the Minimal Supersymmetric Standard Model is given in section 1.2.4.. In general, given a superpotential W and a kinetic potential K, the supersymmetric Lagrangian is given by

$$L_{SUSY} = \int d^4\theta K + \left(\int d^2\theta W + h.c. \right). \tag{1.40}$$

If the theory contains n chiral superfields, the i-th auxiliary field $F_i^\dagger$ is replaced by

$$F_i^\dagger = -\frac{\partial W(\phi)}{\partial \phi_i}, \tag{1.41}$$

its solution to the classical equation of motion, where $W(\phi)$ is the superpotential with all its chiral superfields replaced by its scalar components. Similarly, the auxiliary field D_G^a for a gauge group G is given by

$$D_G^a = -g_G \sum_i \phi_i^\dagger \tau^a \phi_i, \tag{1.42}$$

where g_G is the coupling constant of the gauge group.

1.2.2. Supersymmetry Breaking

As a consequence of supersymmetry, all components within a superfield must have the same mass. This cannot be true in Nature. For instance, LEP puts a lower limit of ~ 100 GeV on the masses of sleptons, and none of them has been discovered. Therefore, supersymmetry must be broken.

17

Consider an infinitesimal SUSY transformation, with parameter ξ, on a chiral superfield. The changes in its components are

$$\delta\phi = \sqrt{2}\xi\psi, \tag{1.43}$$

$$\delta\psi = \sqrt{2}\xi F + i\sqrt{2}\partial_\mu\phi\sigma^\mu\bar{\xi}, \tag{1.44}$$

$$\delta F = \frac{1}{\sqrt{2}}\partial_\mu\psi\sigma^\mu\bar{\xi}. \tag{1.45}$$

In a supersymmetric broken vacuum, the VEV of any one of the above terms can be non-zero. But only $\langle 0|F|0\rangle$ can be allowed to be non-zero while preserving Lorentz invariance. Similarly, a non-zero VEV for the D field results in supersymmetry breaking.

Supersymmetry breaking must be "soft". This means radiative corrections do not induce a quardratically divergent correction to scalar masses. There is a finite set for soft breaking terms and these are listed below.

1.2.3. R-parity

In a supersymmetric theory, one can write several operators in the superpotential $u_R d_R d_R$, leading to baryon and lepton number violation. Such terms can be avoided by introducing a $U(1)$ R-symmetry on the superfields. Under an R-symmetry transformation, a chiral superfield X with R-charge R_X transforms as

$$X \to e^{-iR_X\delta}X, \tag{1.46}$$

where δ is the transformation parameter. Its components transform as,

$$\theta^\alpha \quad \rightarrow \quad e^{i\delta}\theta^\alpha, \tag{1.47}$$

$$\phi \quad \rightarrow \quad e^{-iR_X\delta}\phi, \tag{1.48}$$

$$\psi^\alpha \quad \rightarrow \quad e^{-i(R_X-1)\delta}\psi^\alpha, \tag{1.49}$$

$$F \quad \rightarrow \quad e^{-i(R_X-2)\delta}F. \tag{1.50}$$

In other words, the scalar component has R-charge R_X and the fermion component has R-charge R_X-1. A Z_2 parity, with $\delta=\pi$ is sufficient to forbid the presence of R-parity violating operators. In the minimal supersymmetric standard model discussed below, superfields in the quark and lepton sector have R-charge $+1$, and in the gauge and Higgs sector, 0.

1.2.4. Minimal Supersymmetric Standard Model

The Minimal Supersymmetric Standard Model (MSSM) is the simplest supersymmetric extension of the Standard Model. The chiral superfields in the MSSM are, in the quark sector Q, u_R, d_R and in the lepton sector L, e_R. The Higgs sector contains two chiral superfields, H_u and H_d, with hypercharges $1/2$ and $-1/2$, respectively. The MSSM superpotential is [12]

$$W_{MSSM} = Y_u Q H_u u_R - Y_d Q H_d d_R - Y_l L H_d e_R + \mu H_u H_d. \tag{1.51}$$

Soft supersymmetry breaking can be achieved by a number of terms. These are

− scalar masses $m_\phi \phi^\dagger \phi$ for the squarks and sleptons

– gaugino masses $M_a\lambda^a\lambda^a$ for the bino, wino, and gluino

– trilinear scalar couplings $a_u\tilde{Q}\phi_u\tilde{u}_R$, $a_d\tilde{Q}\phi_d\tilde{d}_R$ and $a_e\tilde{L}\phi_d\tilde{e}_R$

– Higgs masses $m_{Hu}^2\phi_u^*\phi_u + m_{Hd}^2\phi_d^*\phi_d + (b\phi_u\phi_d + c.c.)$

Electroweak symmetry is broken by having the two Higgs scalars acquiring non-zero VEVs, $\langle\phi_u\rangle = v_u$ and $\langle\phi_d\rangle = v_d$, with $v_u^2 + v_d^2 = v^2 = 246$ GeV. The ratio between the two VEVs is parametrized as $\tan\beta = v_u/v_d$. There exists an upper limit on the tree level mass of the lightest netural Higgs, h, in the MSSM

$$m_h^0 < m_Z\cos 2\beta, \tag{1.52}$$

which is below the experimental lower limit [14] $m_h \gtrsim 115$ GeV. Radiative corrections can relax equation (1.52) so that it is consistent with the experimental bound. However, it requires heavy squarks as well as large $\tan\beta$.

1.2.5. Lepton Flavor Problem

Experimental bounds on flavor changing neutral currents (FCNC) in the lepton sector place severe constraints on lepton mixing. With the absence of right handed neutrinos, the Standard Model naturally avoids this bound. This can be seen clearly by comparing the quark and lepton sectors in the Standard Model. The mass terms in the quark sector are

$$-\bar{U}_L\mathbf{M_U}u_R - \bar{D}_L\mathbf{M_D}d_R, \tag{1.53}$$

where the mass matrices $\mathbf{M_U}$ and $\mathbf{M_D}$ are 3×3 in family space. To diagonalize these matrices, we need to fix the phases of all four quark fields by separate unitary transformations. This leads to unavoidable flavor mixing in the quark sector via the

interaction with the W boson,

$$gW^\mu \bar{U}_L \mathbf{V} \gamma_\mu D_L, \qquad (1.54)$$

where $\mathbf{V}$ is a 3×3 matrix in flavor space, called the CKM matrix. This matrix is in general, non-diagonal in the mass eigenstates of the quarks and cannot be rotated away. Therefore it leads to flavor mixing in the quark sector. In the lepton sector, however, only one mass term is present,

$$-\bar{\nu}_L \mathbf{M_L} l_R. \qquad (1.55)$$

Notice that there is no mass terms involving l_L. Diagonalizing the lepton mass matrix by fixing the phases of ν_L and l_R, the interaction term with the W becomes $gW^\mu \bar{\nu}_L \mathbf{V}' \gamma_\mu l_L$. We still have the freedom to fix the phase of l_L to absorb the mixing matrix $\mathbf{V}$. Therefore, any lepton mixing in the Standard Model is physically unobservable, and it naturally avoids the experimental bound on lepton mixing.

In the MSSM, sleptons can mix to give significant contributions to FCNCs, and there are no symmetries to regulate the size of the mixings. The bound on the branching ratio of $\mu \to e\gamma$ alone sets an upper limit on the slepton mixing $\delta_{ij} \lesssim 10^{-3}$. This is one manifestation of the supersymmetric flavor problem.

1.3. Quirks

The idea of quirks was first proposed by [13] and more recently, by [15]. A quirk is a fermion that transforms under the electroweak $SU(2) \times U(1)$, as well as a confining gauge group $SU(2)_{ic}$ with scale Λ_{ic} much less than the quirk mass

m_Q, $\Lambda_{ic} \ll m_Q$. This new confining force is referred as the infracolor force. This hierarchy between Λ_{ic} and m_Q is a sufficient condition to ensure that fragmentation of quirky strings under this confining group does not occur. To see this, consider a very simplified model, where the flux tube connecting two quirks breaks, transferring the energy over the quirk compton wavelength $\lambda_c = m_Q^{-1}$ to pop out a virtual quirk pair. For this process to go on-shell, the flux tube energy over λ_c must be larger than $2m_Q$. From dimensional analysis, the energy per unit length of the flux tube must be of order Λ_{ic}^2. The flux tube energy integrated over a compton wavelength is then $m_Q(\Lambda_{ic}/m_Q)^2 \ll m_Q$. Therefore, quirky strings do not break.

As Standard Model particles do not transform under infracolor, only infracolor singlets can be produced through Standard Model interactions at colliders. As the quirky string connecting the pair of quirks cannot fragment, they form a meson with high angular momentum after being produced. The meson then sheds its angular momentum by emitting soft radiation before annihilating. The annihilation products can be reconstructed into resonances corresponding to the quirkonium mass at the detector.

If the up and down type quirks are very nearly degenerate in mass, quirky baryons can be a candidate of dark matter [16], and this provides added motivation for understanding the signals of quirks in colliders.

1.4. Outline

In the previous sections, the motivations for new physics, and the difficulties faced by the Standard Model and its simplest supersymmetric extension were discussed. It was shown that the Standard Model itself cannot produce a sufficiently strong electroweak phase transition to explain the observed baryon asymmetry.

Furthermore, the mechanism that suppresses the MSSM lepton flavor changing neutral currents is far from obvious. In the follow chapters, this dissertation will provide possible solutions to these problems. In chapter II, it will be shown that the strength of the electroweak phase transition from the inclusion of a fourth generation of quarks and supersymmetry together is sufficiently strong to explain the observed baryon asymmetry in the universe. In chapter III, it is shown that by promoting the Z_2 R-parity in the MSSM to a continuous $U(1)$ R-symmetry, the mixing angles of the sleptons can be of order unity, while evading the severe constraints posed by $\mu \to e$ experiments, thus solving the MSSM lepton flavor problem. In chapter IV, the branching ratios of quirkonium decays are calculated and the decay branching ratios of quirkonia are shown.

Chapters II, III, and IV include previously published and unpublished co-authored material with Graham Kribs.

CHAPTER II

FOURTH GENERATION, SUPERSYMMETRY & ELECTROWEAK BARYOGENESIS

This work was published in volume 78 of the journal *Physical Review D* in October, 2008. Graham Kribs initiated this project; Ricky Fok performed all the calculation and produced the tables and plots that appear in this chapter.

The origin of the antimatter-matter asymmetry is a deep mystery that remains unsolved. Conditions that can lead to a dynamical asymmetry between baryons and anti-baryons were articulated years ago by Sakharov [3]: baryon number violation, C and CP violation, and out-of-thermal-equilibrium processes. All three conditions are satisfied by the Standard Model as it passes through the electroweak phase transition. But, the CP violation is too small [17], and the phase transition is not strongly first-order (e.g., [2, 4, 18–20]), given the direct search bounds on the Higgs from LEP. New physics with large CP violation is trivial to introduce into the model; weak scale supersymmetry is an obvious example (care needs only to be taken to ensure that induced electric dipole moments are within the experimental bounds). Even with a new source of CP violation, if the phase transition is not strong enough, any generated baryon asymmetry will be washed out. New physics that enhances the first order phase transition, however, is generally much more tricky to achieve.

In the early 1990s it was realized that the electroweak phase transition could be enhanced by modifying the effective cubic coupling in the thermal potential [18]. Nontrivial modifications of the cubic coupling require additional scalars with order one couplings to the Higgs. In the minimal supersymmetric standard model (MSSM),

the scalar superpartners to the top quarks stop can play precisely this role [21–23]. It has long been advocated that the region of MSSM parameter space with a light stop (and a light Higgs) can yield a strong enough phase transition. Unfortunately, the combination of direct searches for the Higgs and direct searches for stops have virtually ruled out this possibility. The remaining parameter space [24] requires a large hierarchy between the left-handed and right-handed stops to ensure the Higgs satisfies the LEP bound.

The necessity to go beyond the MSSM as a means to strengthen the first order phase transition is now widely discussed [25–33]. Several of these ideas add a singlet field, such as in the NMSSM or nMSSM. Another related idea is to simply cut off the SM at a low scale, adding the effects of higher dimensional operators [34] (which can be equivalent to integrating out a singlet).

Yet another interesting possibility, and the one we will focus on in this chapter, is to add more particles with modestly strong couplings to the Higgs. This was proposed in [29]; the additional particles have quantum numbers such that they mix with the MSSM charginos and neutralinos. Heavy particles that receive their mass entirely or dominantly from electroweak symmetry breaking can have a substantial impact on the electroweak phase transition. In this chapter we consider a modification to the MSSM similar in spirit to [29] to enhance the phase transition. Namely, we add a fourth generation of particles (and sparticles) to the MSSM. Larger couplings to the Higgs are automatic simply due to the direct search bounds from LEP and Tevatron on the Yukawa couplings of these new heavy fermions.

A fourth generation has historically been strongly disfavored by the absence of flavor mixing, the $Z \to \nu\bar{\nu}$ constraint, and electroweak precision data (for instance, see [35]). All of these objections can be straightforwardly overcome, as was recently

emphasized in [36]. Below we summarize these results in the form of the parameter space that is allowed. It is interesting that the constraints from electroweak precision data can be overcome without or with an electroweak scale Majorana mass for the fourth generation right-handed neutrinos. In the case that a Majorana mass does indeed exist, lepton number is violated at the electroweak scale, and so scenarios of baryogenesis that rely on an earlier generation of $B-L$ number (such as leptogenesis) do not work here [37]. Electroweak baryogenesis is one of the few mechanisms not sensitive to this source of lepton number violation, and thus becomes even more interesting to study.

2.1. Setup

We consider a low energy supersymmetric theory with a fourth chiral generation of matter (the "4MSSM"). A fourth chiral generation of matter does affect electroweak precision observables. One of the main results of [36] was to show that it can be made completely consistent with electroweak precision data so long as there are modest mass splittings between the isospin partners in the quark and lepton doublets. This splitting causes a modest reduction in S simultaneous with a positive contribution to T, allowing ensembles of parameters that are within the 68% CL ellipse of the LEP Electroweak Working Group [38]. For example, the mass spectrum $m_{\nu'} = 100$ GeV, $m_{\ell'} = 155$ GeV, $m_{t'} = 310$ GeV, $m_{b'} = 260$ GeV, and $m_h = 115$ GeV is perfectly acceptable. There is strong sensitivity to the mass *differences* while only mild sensitivity to the overall scale of the particles. We will present results for both the electroweak preferred ratio $m_{t'}/m_{b'} \sim 1.2$ as well as $m_{t'} = m_{b'}$ for comparison.

With supersymmetry, there are additional contributions to electroweak precision observables from superpartners (e.g., [39]). We have not included these contributions

26

to optimize the parameter set to match electroweak data, simply because many more parameters enter the fit that can be freely adjusted without affecting our results for the electroweak phase transition. We therefore take fourth generation Yukawa couplings consistent with [36] and take the scalar partner masses to be equal, eliminating this potential additional contribution to isospin violation.

We will neglect all sub-leading contributions to the zero-temperature and finite temperature effective potential. Sub-leading for us means couplings smaller than about 1. We retain, of course, the contributions from gauge bosons. But we neglect light fermions (u,d,c,s,b,e,μ,τ), Higgs bosons (the quartic is small), and all superpartners other than $\tilde{t}'_{1,2}, \tilde{b}'_{1,2}, \tilde{t}_{1,2}$. We also neglect contributions from fourth generation leptons because the number of degrees of freedom per particle is only $1/3$ that of quarks and the bounds on the mass from the non-observation in experiment are much weaker than for quarks.

2.2. Supersymmetry with $\tan\beta = 1$

In the limit $\tan\beta \to 1$, several aspects of supersymmetry drastically simplify. From the definition of $\tan\beta \equiv \langle H_u \rangle / \langle H_d \rangle$, we see the vevs are equal, $v_u = v_d = v/\sqrt{2}$, where $v = 246$ GeV. Yukawa couplings,

$$y_f = \frac{2m_f}{v} \, , \tag{2.1}$$

are the same for the up-type and down-type fermions.

In the 4MSSM, the fourth generation quarks have large Yukawa couplings,

$$y_{t',b'} = 2.1 \left(\frac{m_{t',b'}}{260 \text{ GeV}} \right) \, , \tag{2.2}$$

27
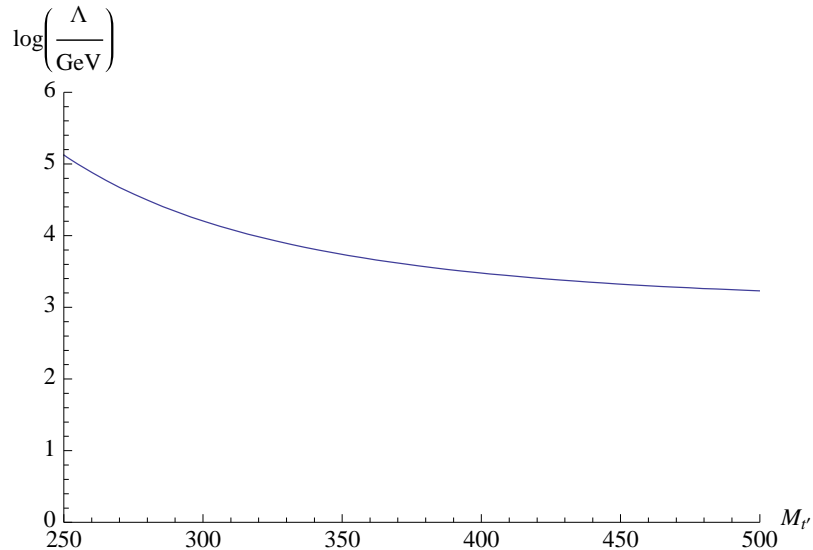
FIGURE 2.1: An estimate of the cutoff scale of the 4MSSM as a function of the fourth generation fermion mass by running the one-loop RGEs of the quark Yukawas up to where they encounter a Landau pole ($y_{f'} \sim 4\pi$).

where 260 GeV is shown for convenience in comparison to the current direct search bounds from the Tevatron [40, 41]. Note that these Yukawa couplings are a factor of $\sqrt{2}$ larger than in a non-supersymmetric model, since the t' and b' acquire their mass only through couplings to the up-type and down-type Higgs, respectively. If $\tan\beta \neq 1$, either the up-type or down-type Higgs vev is reduced, and thus to hold the masses of the fermions fixed, one of $y_{t'}, y_{b'}$ must increase. The choice $\tan\beta = 1$ therefore allows the largest possible physical fourth generation fermion masses with the smallest Yukawa couplings. Since y_f cannot be arbitrarily large for perturbation theory to be valid, the parameter choice $\tan\beta = 1$ is really just maximizing the cutoff scale of the model. Even with this adjustment, the cutoff scale is low. This can be estimated by running the one-loop renormalization group equations for the Yukawa couplings up to $\sim 4\pi$. We show this scale as function of fermion mass in Fig. 2.1. Note that requiring $y_f^2/(4\pi) \lesssim 1$, implies $y_f \lesssim 3.5$, corresponding to $m_f \lesssim 450$ GeV;

28

we will not consider fermion masses that much exceed this value.

In the limit $\tan\beta \to 1$ the Higgs sector also drastically simplifies. The tree-level potential in the MSSM with $\tan\beta = 1$ is

$$V = \left(m^2_{H_u} + \mu^2\right)|H^0_u|^2 + \left(m^2_{H_d} + \mu^2\right)|H^0_d|^2$$
$$-(bH^0_u H^0_d + \text{c.c.}) + \frac{1}{8}\left(g^2 + g'^2\right)\left(|H^0_u|^2 - |H^0_d|^2\right)^2. \tag{2.3}$$

Expand the neutral components as

$$\begin{pmatrix} H^0_u \\ H^0_d \end{pmatrix} = \frac{1}{\sqrt{2}}\begin{pmatrix} v \\ v \end{pmatrix} + \frac{1}{\sqrt{2}}\begin{pmatrix} \cos\alpha & \sin\alpha \\ -\sin\alpha & \cos\alpha \end{pmatrix}\begin{pmatrix} h \\ H \end{pmatrix} \tag{2.4}$$

where the α rotation matrix diagonalizes the Higgs fluctuations (h, H) into mass eigenstates. In the limit that the second Higgs doublet "decouples" $(m_{A^0, H, H^{\pm}} \gg m_h)$, the mixing angle $\alpha \to \beta$, and thus the lightest Higgs is simply $h = (H^0_u - H^0_d)$. In this limit the tree-level Higgs potential vanishes, since h corresponds to the excitation of a D-flat direction.

Since electroweak precision data prefers $m_{t'}/m_{b'} \simeq 1.2$, this could be arranged either by adjusting just these two Yukawa couplings $y_{t'}/y_{b'} = 1.2$ or instead adjusting $\tan\beta = 1.2$. These two scenarios are nearly equivalent for our purposes, and so we choose to set $\tan\beta = 1$. Notice that even if $\tan\beta = 1.2$, this would correspond to the addition of $0.03M^2_Z$ to the (mass)^2 of the Higgs potential. As we will see, the one-loop contributions will be far larger than this, so it is safe to completely neglect tree-level contributions even if $\tan\beta$ were allowed to vary slightly from 1.

In addition to taking $\tan\beta = 1$, we also choose supersymmetric parameters such that the mass eigenstates of $\tilde{t}'_{1,2}$ and $\tilde{b}'_{1,2}$ correspond to the gauge eigenstates $\tilde{t}'_{L,R}$

and $\tilde{b}'_{L,R}$. This is done purely to simplify our calculation. It is a rather conservative approximation, since it is well known that increasing the off-diagonal contribution to the squark mass matrix leads to an enhancement in the one-loop contribution to the Higgs mass (e.g., see [42]). We expect that the parameter space with a strong first-order phase transition will enlarge as this restriction is relaxed. Note that since the off-diagonal left-right contribution to the up-type and down-type squark mass matrix is equal to $m_f(A_f - \mu)$ (where again, $\tan \beta = 1$), this simplification corresponds to the specific parameter choice $A_f = \mu$.

Finally, as we discussed above, the Higgs potential simplifies in the limit $m_{A^0}, m_{H^\pm}, m_{H^0} \gg m_h$. This is a common assumption in the electroweak phase transition literature: The calculational advantage is that the low energy theory is effectively a one-Higgs-doublet model that is drastically simpler to analyze at finite temperature.

2.3. One-loop Effective Potential

In the 4MSSM with $\tan \beta = 1$, loop corrections entirely determine the Higgs potential. We are interested in the loop corrections to just the scalar fluctuation $\phi = (h+v)/\sqrt{2}$. At one-loop the effective potential for the Higgs is simply determined from the Coleman-Weinberg potential

$$V_1 = \sum_i \frac{n_i}{64\pi^2} M_i(\phi)^4 \left(\log \frac{M_i(\phi)^2}{\mu^2} - c_i \right) \tag{2.5}$$

where $M_i(\phi)$ are the field-dependent masses, μ is the renormalization scale ($\overline{\text{MS}}$ scheme), and c_i's are constants corresponding to 5/6 for gauge bosons and 3/2 for

fermions and scalars. The degeneracies per particle are $n_q = -12$ (for each $q = t, t', b'$), $n_{\tilde{q}_L} = n_{\tilde{q}_R} = 6$, $n_{W_T} = 4$, $n_{Z_T} = 2$, $n_{W_L} = 2$, $n_{Z_L} = 1$.

Expanding the effective potential as given above, evidently the minimum is not necessarily located at the proper electroweak breaking scale $v = 246$ GeV. This is easily remedied by imposing a renormalization condition on the mass parameter such that the minimum is enforced to be at v. This amounts to adding the v-dependent contribution to the effective potential,

$$\Delta V = -\frac{dV_1(\phi = v)}{dv^2}\phi^2 =$$
$$-\sum_i \frac{n_i}{32\pi^2} M_i^2(v) \frac{dM_i^2(v)}{dv^2} \left(\log \frac{M_i^2(v)}{\mu^2} + \frac{1}{2} - c_i \right) \phi^2. \qquad (2.6)$$

The masses used in the effective potential are $\overline{\text{MS}}$ masses that differ from the physical (pole) masses through finite and log-dependent corrections. The running fermion masses are given at one-loop by

$$m_f|_{\text{pole}} = m_f(\mu) \left[1 + \frac{\alpha_s}{\pi} \left(\frac{4}{3} + \log \frac{\mu^2}{m_f^2} \right) \right]. \qquad (2.7)$$

Since the fourth generation fermions overwhelmingly dominate the contributions to the (zero and finite-temperature) effective potential, we take $\mu = \sqrt{m_{t'} m_{b'}}$, i.e., the scale of the largest electroweak breaking masses in the problem. This tends to minimize the higher order corrections to the potential, though are calculations are not particularly sensitive to the precise choice of renormalization scale.

The running scalar masses also differ from their physical pole masses through one-loop corrections depending on not only the gluon but also gluino diagrams [39]. This correction is generally numerically smaller than the correction to the

31
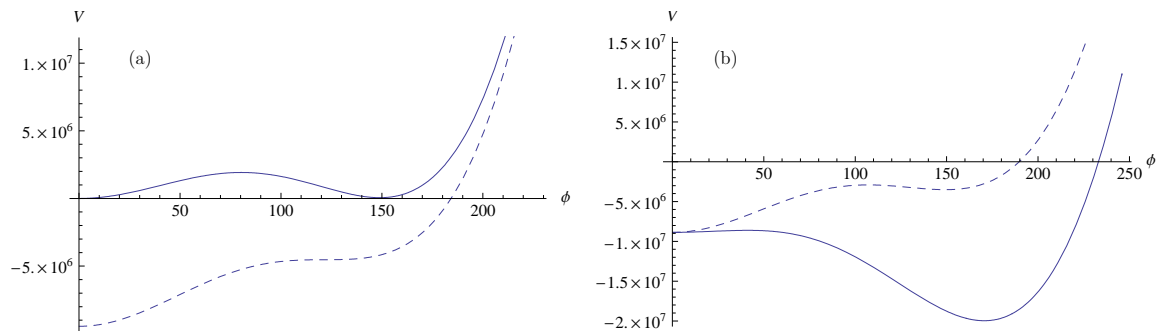
FIGURE 2.2: An illustration of the effect of adding one additional heavy fermion that obtains a mass of 300 GeV entirely from electroweak symmetry breaking. The figure (a) on the left shows an effective potential at the critical temperature T_c (solid line) and the new effective potential with an additional heavy fermion (dashed-line), except that *only* the thermal contribution, V_{T1}, is included in (a). Figure (b) on the right shows the the effect of including just the thermal contribution (dashed-line), identical to Figure (a), and then the effect of including both the thermal contribution as well as the zero-temperature contribution V_1 (solid-line). The net effect shown in Figure (b) solid-line is that the global minimum at $\phi \simeq \phi_c$ decreases and thus T_c increases.

fermion mass, typically less than a few %. Moreover, since the correction is gluino mass-dependent, relating the pole mass to the running mass requires specifying an otherwise unfixed parameter in our model. We choose instead to simply take $m_{\tilde{f},\mathrm{pole}} = m_{\tilde{f}}(m_{\tilde{f}})$, thus neglecting the difference between the pole and running mass for the squarks.

2.4. Finite Temperature One-loop Effective Potential

The finite-temperature contributions to the effective potential are [2, 4, 18–20]

$$V_T = V_{T1} + V_{\mathrm{ring}} \tag{2.8}$$

where

$$V_{T1} = \sum_i \frac{n_i}{2\pi^2} J_i \left(\frac{M_i^2}{T^2} \right) T^4 \qquad (2.9)$$

$$V_{\text{ring}} = -\frac{T}{12\pi} \sum_{k=W_L, Z_L} n_k \left(\bar{M}_k^3 - M_k^3 \right) \qquad (2.10)$$

and

$$\bar{M}_k^2 = M_k^2 + \Pi_k . \qquad (2.11)$$

The field-dependent fermion and scalar masses are

$$M_f(\phi)^2 = 2y_f^2 \phi^2 \qquad (2.12)$$

$$M_{\tilde{f}}(\phi)^2 = M_{\text{soft}}^2 + M_f(\phi)^2 . \qquad (2.13)$$

Explicit expressions for the thermal masses of the SM gauge bosons can be found in, e.g., Ref. [43]. The thermal contributions depend on the thermal functions

$$J_{B,F}(y^2) = \int_0^\infty dx\, x^2 \log \left[1 \mp \exp \left(-\sqrt{x^2 + y^2} \right) \right] . \qquad (2.14)$$

Often a high temperature approximation is employed to estimate these integrals. In our case, due to the large Yukawa couplings, this approximation is generally not appropriate. Consequently, all computations given below evaluate the thermal functions $J_{B,F}$ numerically. The ring contribution (2.10) is only relevant for the longitudinal components of the W and Z. No contributions from scalars are included

here since the squarks receive a contribution from soft supersymmetry breaking, and thus they remain heavy in the $\phi \to 0$ limit.

The contributions included in the thermal effective potential are exactly the same as those included in the zero-temperature effective potential. Namely, we include t', b', t, their superpartners $\tilde{t}'_{L,R}, \tilde{b}'_{L,R}, \tilde{t}_{L,R}$, as well as the transverse and longitudinal components of W, Z. All other contributions to the finite-temperature effective potential can be safely neglected.

In the Standard Model, the phase transition becomes second order when the Higgs mass approaches 70 GeV [44]. Qualitatively, this is because the transverse modes of W and Z, which drive the first order phase transition in the standard model, develop a thermal mass from non-perturbative effects. If the transverse thermal masses are large, they effectively remove the cubic term from the thermal potential when the effective potential is reset to zero at $\phi = 0$, and the phase transition becomes second order. In our model, the first order phase transition is mostly driven by squarks. In fact, when W and Z are neglected in our model, ϕ_c and T_c changes very little and the phase transition remains first order. Therefore, we expect non-perturbative effects encountered in the standard model have negligible effects in our calculations.

2.5. Effects of New Heavy Particles

The effects of heavy particles (that receive their mass dominantly from electroweak symmetry breaking) on the electroweak phase transition can be broadly characterized as follows. Consider the effective potential at T_c, where there are two degenerate minima $V_{eff}(0, T_c) = V_{eff}(\phi_c, T_c)$ located at $\phi = 0$ and $\phi = \phi_c$. Now add to this a new particle that satisfies $m(\phi_c)/T_c \gg 1$. The phase transition strength

can be modified via two ways from this new particle. One is through corrections to the thermal contribution $J_{B,F}(m^2/T^2)$; the other is through the zero-temperature Coleman-Weinberg potential.

2.5.1. Thermal Effects

The contributions from bosons and fermions with masses larger than the critical temperature, $m \gg T_c$, can be characterized by how they contribute at large field values $\phi \gg T$ and small field values $\phi \ll T$. At large field values, we can take a *low temperature* approximation to the thermal effective potential. In this limit, the contribution from fermions or bosons becomes

$$V_{T1}|_{T \ll m} = |n| \left(\frac{M(\phi)}{2\pi T} \right)^{3/2} T^4 \exp\left[-\frac{M(\phi)}{T} \right] \tag{2.15}$$

where n counts the number of degrees of fermion per boson or fermion with field-dependent mass $M(\phi)$. Clearly, when $M(\phi) \gg T$, which is equivalent to $\phi \gg T$ (with order one or larger Yukawa couplings), the contribution to the effective potential from fermions or bosons is exponentially suppressed.

At small field values, we can take a high-temperature approximation to the thermal contribution to the effective potential. The leading order contribution is the field-independent constant

$$V_{T1}|_{T \gg m} = -|n| c_{B,F} \frac{\pi^2}{90} T^4 \tag{2.16}$$

where $c_{B,F} = (1, 7/8)$ for a boson or fermion contribution.
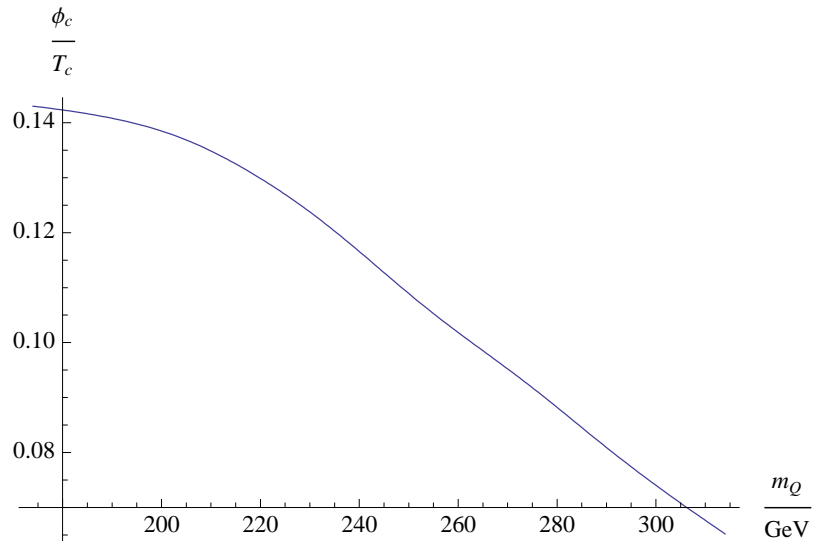
FIGURE 2.3: This plot shows that the electroweak phase transition order parameter decreases if a new heavy chiral quark is added to the theory.

The combination of equations (2.15) and (2.16) imply that the introduction of a heavy fermion or boson causes a substantial negative shift in the potential at $\phi = 0$ while causing a negligible shift in the potential at $\phi = \phi_c$. As an illustration, we show in Fig. 2.2(a) the effect of adding one additional heavy degree of fermion that obtains a mass of 300 GeV entirely from electroweak symmetry breaking. Readjusting the minimum $V_{\text{eff}}(\phi = 0) = 0$ shifts the potential up for all field values, thereby removing the second minimum at $\phi = \phi_c$, and thus restoring electroweak symmetry. We must *lower* the temperature further in order to have the second minimum reappear in the effective potential with the new heavy fermion or boson.
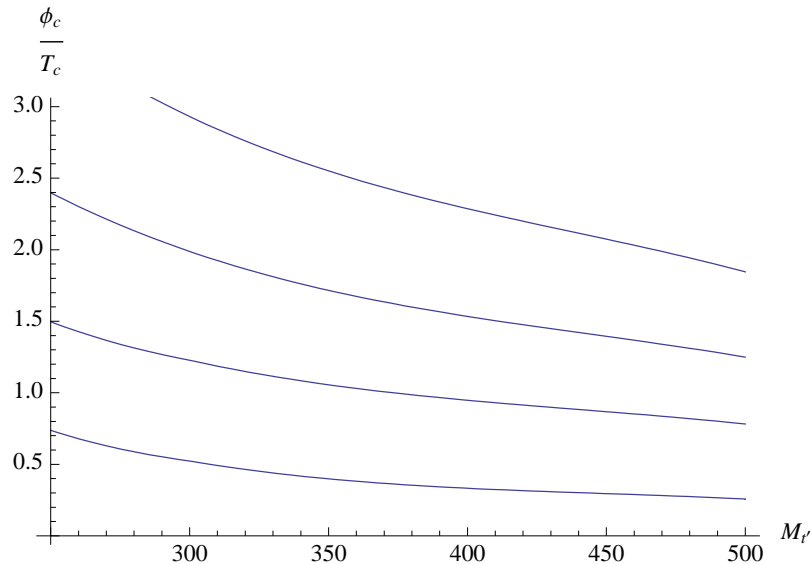
FIGURE 2.4: Contour plot with the ratio $m_{\tilde{q}'}/m_{q'}$ fixed, from top to bottom, as $1.05, 1.1, 1.15, 1.2$. The masses of the fourth generation quarks are taken to be equal.

2.5.2. Zero-temperature Effects

The second effect of heavy bosons and fermions is that they also modify the zero temperature effective potential. Here, however, the effect of fermions and bosons is different. There are two contributions whose origin is ultimately the Coleman-Weinberg potential. One contribution is to the quartic coupling (2.5), while the second contribution is the quadratic term (2.6). For smaller field values, i.e., $\phi \lesssim \mu$, the dominant contribution is from the quadratic term. Since we choose $\mu \simeq m_{q'}$, the log term drops out, giving an overall *negative* (*positive*) contribution to the effective potential from fermions (bosons).

The negative contribution from fermions at modest field values actually overpowers the effect from the thermal contributions discussed above. This is illustrated in Fig. 2.2(b). The net result is that introducing new heavy chiral fermions causes a *decrease* in ϕ_c/T_c as the mass of the fermion is increased. The resulting
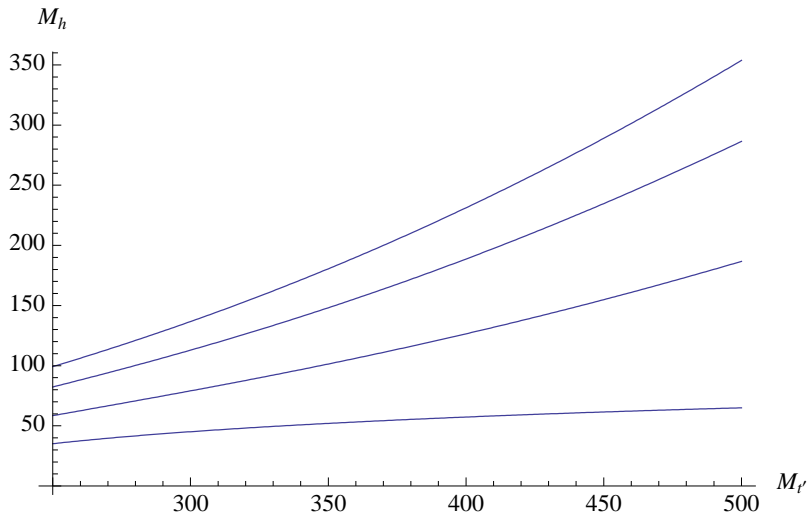
FIGURE 2.5: Contour plot of the lightest Higgs mass as a function of the fourth generation quark mass. Each contour corresponds to a fixed ratio $m_{\tilde{q}'}/m_{q'}$, from top to bottom, 1.2, 1.1, 1.0, 0.95 with $m_{t'} = m_{b'}$ and $m_{\tilde{t}} = m_{\tilde{q}'}$.

decrease in the order parameter of the SM with one additional chiral fermion is shown in Fig. 2.3.

Adding bosonic contributions cancels the contribution from fermions in the Coleman-Weinberg potential. This cancellation is one-loop exact in the limit $m_{\tilde{f}'} = m_{f'}$, i.e., no SUSY breaking contribution to the scalar mass. This makes it clear that we need both heavy fermions *and* scalars with equal numbers of degrees of freedom and similar masses to utilize the mechanism of Ref. [29] to lower ϕ_c/T_c.

Ref. [29] estimated that of order ten or more degrees of freedom is needed to enhance the phase transition sufficiently to achieve $\phi_c/T_c \gtrsim 1$. A fourth generation quarks corresponds to adding fifteen degrees of freedom. (We could have equivalently added degrees of freedom in other ways, such as several pairs of vector-like lepton doublets that only get mass through the Higgs mechanism. This is anohter interesting possibility that we will not explore here [45].) We have calculated the strength of
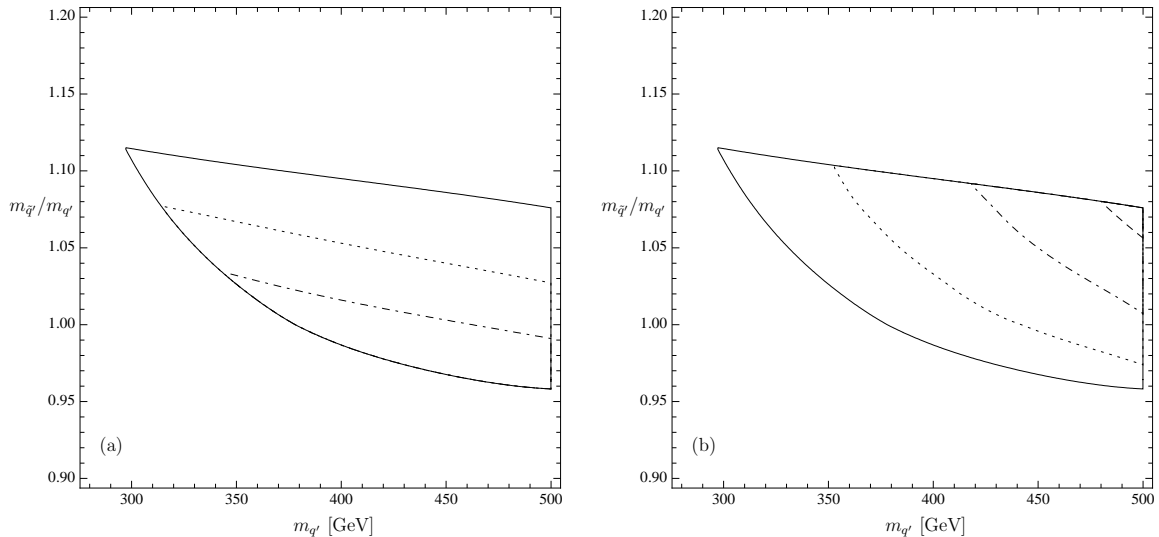
FIGURE 2.6: The region in the quark/squark mass plane where the electroweak phase transition is strongly first-order is shown. The regions shown in the left- and right-hand side figures (a) and (b) are identical: the upper boundary (the solid line) is determined by $\phi_c/T_c = 1$ while the lower boundary is determined by $m_h = 115$ GeV. The dotted and dot-dashed contours on the left-hand side figure (a) corresponding to $\phi_c/T_c = 1.5, 2.0$ respectively. The dotted, dot-dashed and dashed contours on the right-hand side figure (b) correspond to the Higgs masses $m_h = 150, 200, 250$ GeV respectively.

the phase transition for a range of quark and squark masses. The results are shown in Fig. 2.4.

2.6. Lightest Higgs Mass in the 4MSSM

Given the parameter choice $\tan \beta = 1$, the tree-level Higgs potential vanishes, and thus the lightest Higgs mass also vanishes at leading order. It is well known that loop corrections from splitting the tops from stops in the Coleman-Weinberg potential provide large corrections to the tree-level value. In the 4MSSM, we can split not only the top and stops, but also split the fourth generation quarks from squarks. Since the one-loop contribution to the Higgs quartic coupling is proportional

to y_f^4, even a small splitting between f and $\tilde{f}$ has a very important effect. A one-loop estimate of the lightest Higgs mass in the 4MSSM can be obtained by taking $d^2(V_0 + V_1)/d\phi^2$ at $\phi = v$. This gives our rough estimate for the Higgs mass

$$m_h^2 = \sum_{f=t,t',b'} \frac{3}{2\pi^2} \frac{m_f^4}{v^2} \log \frac{m_{\tilde{f}}^2}{m_f^2} , \qquad (2.17)$$

where again $v = 246$ GeV. In Fig. 2.5 we show Higgs mass plotted against different $m_{t'} = m_{b'}$ masses, where we fixed all squark masses to be equal $m_{\tilde{t}'} = m_{\tilde{b}'} = m_{\tilde{t}}$. Each contour has the fourth generation squark-to-quark mass ratio fixed $m_{\tilde{f}'}/m_{f'}$. Clearly, when the splitting between the fourth generation squarks and quarks vanishes, there is an insufficient one-loop contribution from top/stop loops to raise the Higgs mass much above about 60 GeV. Nevertheless, for even a small splitting between fourth generation squarks and quarks, one can easily obtain a one-loop contribution to the Higgs mass that far exceeds the LEP bound so long as $m_f \gtrsim 300$ GeV.

2.7. Results

Combining our calculation of the phase transition with our calculation of the Higgs mass, we can find the allowed region in parameter space where the first order phase transition is strong $\phi_c/T_c \gtrsim 1$ while the Higgs mass satisfies the LEP bound $m_h > 115$ GeV. We have computed this for the mass ratio $m_{t'}/m_{b'} = 1$ in Fig. 2.6 and $m_{t'}/m_{b'} = 1.2$ in Fig. 2.7. In Fig. 2.6(a) we show contours of increasing ϕ_c/T_c, illustrating that it is straightforward to obtain values that significantly exceed $\phi_c/T_c = 1$. In Fig. 2.6(b) we show contours of increasing Higgs mass, illustrating that it is also straightforward to to obtain values that significantly exceed $m_h = 115$ GeV.
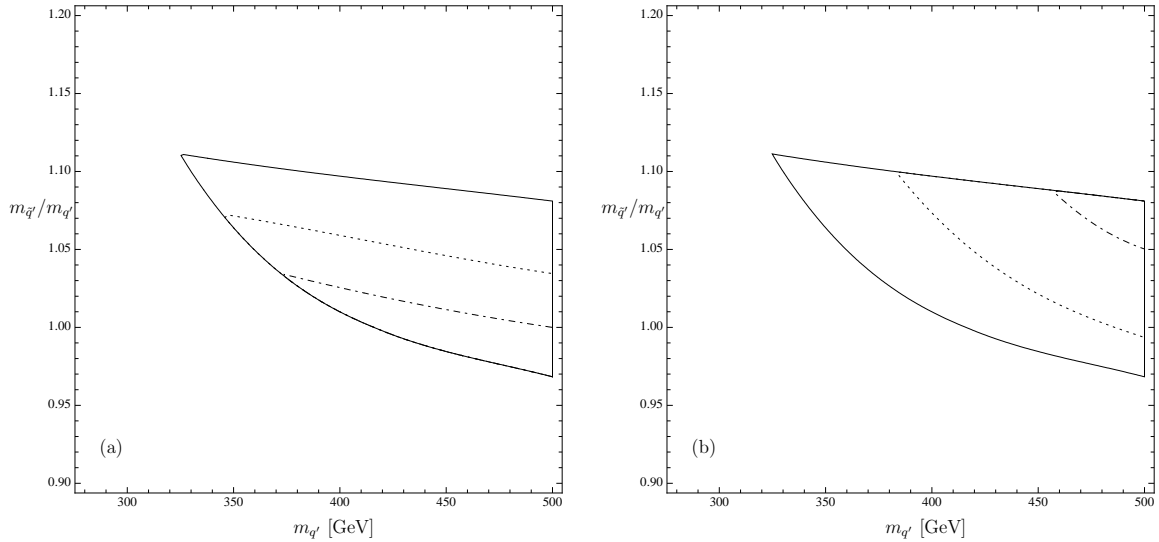
FIGURE 2.7: Same as Fig. 2.6 but we take $m_{t'}/m_{b'} = 1.2$, as favored by electroweak precision data The basic shape and size of the region is the same, illustrating that our results are not particularly sensitive to the heavy fourth generation quark mass ratios.

Note that our plots are with respect to the pole masses of quarks and squarks (as well as the ratio $m_{q'}/m_{\tilde{q}'}$). The quantities that enter the effective potential are $\overline{\mathrm{MS}}$-renormalized masses, which differ (as we discussed above) for fermion masses. Since the fermion pole mass is larger than its $\overline{\mathrm{MS}}$-renormalized counterpart by about 5%, the ratio of pole masses can be as small as 0.95 while the ratio of $\overline{\mathrm{MS}}$ masses is still larger than one. This is why the fourth generation contributions to the Higgs mass (2.17) remains positive even when the ratio of pole masses $m_{q'}/m_{\tilde{q}'}$ is smaller than one.

These results suggest that even though only one-loop approximations for the effective potential and the Higgs mass calculation were employed, we are not near any critical boundary, and so a more refined calculation is expected to only modestly adjust the parameter regions we have shown. For instance, there are several much

41

higher precision calculations of the Higgs mass that could be employed; since we choose $A_f = \mu$, the off-diagonal contribution to the squark mass matrix vanished. This choice of parameters underestimates the Higgs mass that could be obtained (all other parameters equal), and so we expect that a more exhaustive scan of the parameter space including the latest two-loop expressions for the Higgs mass will only relax the constraints we have shown. We expect similar statements also hold for the thermal effective potential, since again our results show that there are model parameters where the 4MSSM model has an electroweak phase transition with ϕ_c/T_c that is is far above the critical first-order boundary $\simeq 1$.

In the next chapter, a method to suppress unnaturally large slepton flavor mixing by introducing supersymmetry will be discussed.

CHAPTER III

μ TO e IN R-SYMMETRIC SUPERSYMMETRY

This work was published in volume 82 of the journal *Physical Review D* in August, 2010. Graham Kribs initiated this project; Ricky Fok performed all the calculation and produced the tables and plots that appear in this chapter.

Lepton flavor violation (LFV) is predicted to occur at an unobservably small rate in the Standard Model (SM). In low energy supersymmetric theories, new sources of lepton flavor violation are generic in the soft breaking sector. The experimental non-observation of $\mu \to e$ processes is particularly restrictive, given the impressive bounds on $\mu \to e\gamma$ from MEGA [47] and MEG [48]; on $\mu \to e$ conversion from SINDRUM II [49], and to a lesser extent from $\mu \to 3e$ from SINDRUM [50]. Further progress is expected from the varied experiments that are ongoing as well as planned future experiments such as Mu2e [51] and other proposals utilizing Project X at Fermilab [52].

In the minimal supersymmetric standard model (MSSM), $\mu \leftrightarrow e$ mixing is severely constrained by these bounds (e.g. [53–57]). The size of the mixing can be characterized by the quantity $\delta^\ell_{XY} \equiv \delta m^2_{XY}/m^2$ where δm^2_{XY} is the off-diagonal (12)-entry appearing in the sfermion mass matrix connecting the X-handed slepton to the Y-handed slepton, and m^2 is the average slepton mass. Ref. [57] found $\delta^\ell_{LR} \lesssim 3 \times 10^{-5}$, while $\delta^\ell_{LL} \lesssim 6 \times 10^{-4}$ over a scan of the mSUGRA parameter space. Similarly strong bounds on δ^ℓ_{RR} can also be found, though cancellations between diagrams in the amplitude can in some cases allow for much larger mixing [55–57].

Recently, a new approach to weak scale supersymmetry that incorporates an extended R-symmetry [58], suggests large flavor violation in the supersymmetry breaking parameters may be present *without* exceeding the flavor-violating bounds. This is possible for several reasons: R-symmetric supersymmetry has no flavor-violating LR mixing, solving the worst of the problem trivially. R-symmetric supersymmetry has Dirac gauginos, and no Majorana masses, removing all dimension-5 flavor-violating operators. Finally R-symmetric supersymmetry also has no flavor-conserving LR mixing, and so there are no "large $\tan \beta$ enhanced" effects. These benefits were found to virtually eliminate constraints on the slepton flavor mixing [58].

In this chapter we reconsider the constraints on slepton mixing, specifically, $\mu \leftrightarrow e$ mixing. Unlike the MSSM, the most important constraint is not necessarily $\mu \rightarrow e\gamma$. This is easily seen by inspection of the R-symmetric flavor-violating operators: $\mu \rightarrow e\gamma$ requires a chirality-flip via a muon Yukawa coupling, whereas $\mu \rightarrow e$ conversion has no such requirement. We find that $\mu \rightarrow e$ conversion rules out maximal mixing throughout the right-handed slepton mixing parameter space for sub-TeV superpartner masses. This is complementary to $\mu \rightarrow e\gamma$, where we find cancellations between the bino and Higgsino diagrams, analogous to what was found before in the MSSM [55–57]. For left-handed slepton mixing, we find possible cancellations in the amplitudes for $\mu \rightarrow e$ conversion, and instead $\mu \rightarrow e\gamma$ provides generally the strongest constraint. We also calculated $\mu \rightarrow 3e$ and find it provides the weakest constraint on both left-handed and right-handed slepton mixing throughout the parameter space we consider.

This chapter is organized in as follows: We review the relevant characteristics of a model with an extended R-symmetry, and the super GIM mechanism in Sec. 3.1..

In Sec. 3.2., we begin the discussion of experimental constrains on the parameters from $\mu \to e\gamma$, in Sec. 3.2.1., $\mu \to e$ conversion in Sec. 3.2.2., and finally, $\mu \to 3e$ in Sec. 3.2.3.. In Sec. 3.3. we briefly discuss implications for slepton flavor violation to be observed at LHC.

3.1. A Simplified R-symmetric Model

We are interested in analyzing LFV in the minimal R-symmetric standard model (MRSSM). The gaugino structure of the MRSSM has been studied in detail in Ref. [59], where the mixings and couplings of the four Dirac neutralinos and four Dirac charginos are given. Weak scale supersymmetry with Dirac gauginos is a possibility that was contemplated some time ago [60–62] and more recently [58, 59, 63–78]. A fully general analysis of LFV in the MRSSM would be a substantial undertaking. Fortunately, there are several simplifications we can employ to gain a fairly general understanding of the allowed parameter space of LFV in the MRSSM. One important restriction is that the Dirac wino cannot be light in the MRSSM, due to the structure of the wino supersoft operator [63]. Essentially there is an unavoidable contribution to the vev of the $SU(2)_L$-triplet scalar that causes a contribution to the ρ parameter that is too large unless the wino is above about a TeV. Secondly, since there is no coupling between up-type Higgs and leptons, the contribution from the up-type Higgsino eigenstates is suppressed by the small mixing between bino or $\tilde{H}_d$ and $\tilde{H}_u$, and so can be ignored.

Itemizing the simplifications, we take:

1. The wino mass, M_2, is taken to be sufficiently large so as to give negligible contribution to flavor violating interactions. This simplification means that the ρ-parameter is automatically safe throughout the parameter space we consider.

2. The up-type Higgsino mass μ_u, is also taken to be large for convenience. Since the up-type Higgsinos play no role whatsoever in charged lepton flavor-violation (given also point 1), this is done simply to keep the gaugino sector to a 2×2 structure and thus easily understood. (We will, however, consider effects of a light up-type Higgsino on flavor-violating signals at LHC in Sec. 3.3..)

3. We consider left-handed and right-handed slepton mixing separately. This is standard practice when considering flavor-violation in the MSSM (e.g., [57]). We will see that there are qualitative differences between the allowed parameter space of left-handed and right-handed slepton mixing.

4. We assume the slepton mixing is purely in the 2×2 flavor space of e, μ. Enlarging this mixing to the full 3×3 mixing does not qualitatively change any of our results, and instead simply dilutes the effect of the mixing, while adding more mixing angles and thus more parameters to the model. Since the focus of this chapter is to explore $\mu \leftrightarrow e$ mixing, no further discussion of the 3×3 case will be given.

5. For our numerical results, we take $m_{\tilde{l}_2} = 1.5 m_{\tilde{l}_1}$. This seems a far more drastic assumption than it actually is. Our motivation is to consider slepton flavor violation when there is essentially *no degeneracy* among the sleptons, and so we took the slepton mass ratio to be "order one" but not near one. Taking the ratio much larger than one does not appreciably increase the flavor violation,

46

while taking it smaller causes the super-GIM mechanism to suppress the flavor-violating signal. Our compromise is the above number.

In Appendix A, we provide more details on the gaugino structure and flavor-violating interactions as directly relevant to this chapter. With the above assumptions, there is only one light Dirac chargino (which is $\tilde{H}_d^\pm$-like) and two light Dirac neutralinos (which are mixtures of $\tilde{H}_d^0$ and $\tilde{B}$).

A few more comments on the slepton mass eigenstate hierarchy are in order. MSSM analyses of slepton flavor violation have, by necessity of LFV constraints, concentrated on the case where the mass difference between the different states is small, $\Delta^2 \equiv m_{\tilde{l}_2}^2 - m_{\tilde{l}_1}^2 \ll m_{\tilde{l}_{1,2}}^2$. In this limit, it is straightforward to show that the contribution to LFV can be expanded in powers of Δ^2, taking the form

$$\sin 2\theta_l \left(\frac{\Delta^2}{M_{\text{SUSY}}^2} + \dots \right) , \qquad (3.1)$$

where M_{SUSY} is typically the largest mass sparticle in the diagram that dominates the process. There is no Δ-independent contribution within the parentheses due to the super GIM mechanism (see the next section). Since $\sin 2\theta_l = 2m_{e\mu}^2/\Delta^2$, one factor of Δ^2 cancels, giving proportionality to the δ parameter mentioned in the introduction and used in many other papers on LFV in the MSSM (at least up to a possible further suppression of $|m_{\tilde{l}_1} m_{\tilde{l}_2}|/m_{N,C}^2$ if $m_{N,C} \gg m_{\tilde{l}_{1,2}}$).

In this chapter, Δ^2 is not small, and so using the "δ parameter" is simply not appropriate. Instead, it is easy to see that in the opposite limit, $\Delta^2 \gg m_{\tilde{l}_1}^2$, the contributions to LFV are proportional to simply $\sin 2\theta_l/m_{\tilde{l}_1}^2$. Hence, the relevant parameters we show in most of our numerical results are bounds on $\sin 2\theta_l$ as a

function of the slepton, gaugino, and Higgsino masses. Reducing the splitting can be roughly approximated by relaxing the constraint on $\sin 2\theta_l$ by ratios of $\Delta^2_{\text{old}}/\Delta^2_{\text{new}}$.

3.1.1. The Super GIM Mechanism

The "super-GIM mechanism" – the GIM mechanism [79] applied to flavor in the superpartner sector – is important in understanding the phenomena of flavor violation. As is well known, the super-GIM mechanism arises as a consequence of the unitarity of the slepton mixing matrices that diagonalize the mass matrix; $U^\dagger_{ik}U_{kj} = \delta_{ij}$, where the sum over repeated indices is performed. This combination of mixing matrix elements always appears as a prefactor in the calculation of amplitudes of flavor violating processes. Specifically for our case of slepton flavor violation, we have $U^\dagger_{ek}U_{k\mu} = 0$, corresponding to an incoming muon, and an outgoing electron, with internal sleptons labeled by k. The sum over k corresponds to summing over all mass eigenstate sleptons $\tilde{l}_k$ in the loop. There are two immediate consequences of the super-GIM mechanism.

First, terms that do not depend on the slepton masses do not contribute. Let $f(m_k)$ be some function that depends on the mass of the sleptons and α be some quantity that does not depend on m_k, then

$$\sum_k U^\dagger_{ek}U_{k\mu}[\alpha + f(m_k)] = \sum_k U^\dagger_{ek}U_{k\mu}f(m_k). \tag{3.2}$$

The form of Eq. (3.2) appears when a logarithmic divergent loop integral is dimensionally regularized, and one finds the $1/\epsilon$ term appearing as a constant term α in the above equation. This leads to an important result: the would-be logarithmic UV divergence in flavor-conserving processes is, in fact, UV finite in flavor-violating

48

processes. In this chapter, unless otherwise stated, we will omit the terms in our expressions that are canceled by the super-GIM mechanism.

The other well known consequence is that, when all the sleptons are degenerate, there is no flavor violation. This can be seen again in Eq. (3.2) with $m_k = m$, the sum over all slepton flavors in a flavor-violating process vanishes.

3.2. Experimental Constraints

There are three $\mu \to e$ conversion processes with experimental bounds: $\mu \to e\gamma$, $\mu \to e$ conversion, and $\mu \to 3e$. In this section we present our calculations of the rates of these processes and present results in terms of a series of contour plots showing the allowed parameter space.

The rate for $\mu \to e\gamma$ was estimated in Ref. [58] in the slepton flavor-violating mass-insertion approximation with a pure bino and wino and a specific gaugino hierarchy. In this chapter we have neglected the wino, due to the ρ parameter constraint, and instead included the down-type Higgsino $\tilde{H}_d^0$. Since we have considered large mixing angles, up to and including maximal mixing, we have diagonalized the slepton masses explicitly and done our loop calculations involving the slepton mass eigenstates.

As stated in our simplifications, we have not included contributions from the wino or up-type Higgsino. We focus on the case where the sleptons and the lighter neutralinos are in the sub-TeV range where wino contributions can be reasonably ignored. The up-type Higgsino does not couple to leptons, and we take the light quark Yukawa couplings to vanish. Thus, the up-type Higgsino does not give a significant contribution to any of $\mu \to e\gamma$, $\mu \to e$ conversion in nuclei and $\mu \to 3e$.

With these simplifications, the amplitudes of LFV processes are sensitive to just two neutralinos, mixtures of $\tilde{B}$ and $\tilde{H}_d^0$ inside the loops. We can also neglect the contributions due to charginos because the only light chargino is $\tilde{H}_d^0$-like. Hence, all types of diagrams we consider involving a chargino are suppressed not only by one power of muon Yukawa, but also one power of either the electron Yukawa, or the tiny wino content of the light chargino at the lepton-chargino-sneutrino vertex. This also means that sneutrino mixing does not contribute to LFV processes, and thus the difference in the amplitudes between left-handed and right-handed slepton mixing is due solely to the hypercharges and masses of the left-handed and right-handed charged leptons.

3.2.1. $\mu \to e\gamma$

The neutrinoless muon decay $\mu \to e\gamma$ occurs through the effective magnetic dipole moment operator, $\bar{e}\sigma_{\mu\nu}F^{\mu\nu}\mu$, and requires a chirality flip of fermions. There are no tree level operators that lead to this decay, and the lowest order is at one loop. In the MRSSM, there are only two types of contributions to the $\mu \to e\gamma$ amplitude: one where the chirality flip occurs on the external muon line, and the other where the flip occurs as a result of a muon-smuon-Higgsino vertex proportional to the muon Yukawa coupling. The diagrams are shown in Fig. 3.1.

We calculated the amplitudes in the mass eigenstate basis of the sleptons and neutralinos, and as a check we derived the results obtained in Ref. [54] (replacing their $\tilde{\mu}$-$\tilde{\tau}$ mixing with $\tilde{e}$-$\tilde{\mu}$ mixing). The effective Lagrangian is

$$\mathscr{L}_{eff} = \frac{m_\mu}{2}\bar{e}\sigma_{\mu\nu}F^{\mu\nu}(A^L_{\gamma\mathrm{dip}}P_L + A^R_{\gamma\mathrm{dip}}P_R)\mu. \tag{3.3}$$
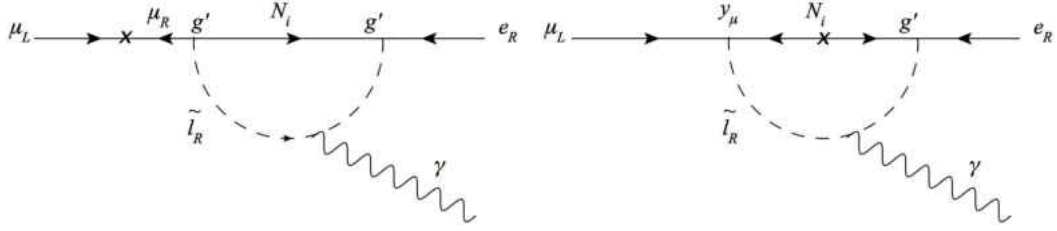
(a) Chirality flip on the external muon line.   (b) Chirality flip at the Yukawa vertex.

FIGURE 3.1: Feynman diagrams for $\mu \to e\gamma$ corresponding to the amplitudes (a) A_{Rin1} and (b) A_{Rin2} mediated by right-handed slepton flavor mixing. The diagrams for left-handed slepton flavor mixing are obtained by swapping $L \leftrightarrow R$.

We rewrite the amplitudes $A_{\gamma\mathrm{dip}}^{L}$ and $A_{\gamma\mathrm{dip}}^{R}$, as

$$A_{\gamma\mathrm{dip}}^{L} = \sum_{i=1}^{2} (A_{Lin1} + A_{Lin2}) \tag{3.4}$$

$$A_{\gamma\mathrm{dip}}^{R} = \sum_{i=1}^{2} (A_{Rin1} + A_{Rin2}) \,, \tag{3.5}$$

where the sum is over the i-th neutralinos. The subscripts 1 and 2 denote the locations of the chirality flip on the muon line and at the muon-slepton-gaugino vertex, respectively. As we shall see below, for right-handed sleptons there can be an accidental cancellation between amplitudes involving these diagrams.

The $\mu \to e\gamma$ branching ratio is given by

$$BR(\mu \to e\gamma) = \frac{48\alpha\pi^3 m_\mu^2}{G_F^2}\left[|A_{\gamma\mathrm{dip}}^{L}|^2 + |A_{\gamma\mathrm{dip}}^{R}|^2 \right], \tag{3.6}$$

with the amplitudes involving a neutralino N_i and sleptons $\tilde{l}_1$ and $\tilde{l}_2$ with the sleptons mass-ordered as $m_{\tilde{l}_1} < m_{\tilde{l}_2}$. The amplitudes involving right-handed sleptons are

$$A_{Rin1} = \frac{(Y_R^l)^2 g'^2}{3(16\pi^2)}(O_{Li\tilde{B}})^2 \cos\theta_{\tilde{l}} \sin\theta_{\tilde{l}} \left[\frac{f_{n1}(x_{1i})}{m_{\tilde{l}_{R1}}^2} - \frac{f_{n1}(x_{2i})}{m_{\tilde{l}_{R2}}^2}\right], \tag{3.7}$$

$$A_{Rin2} = \frac{Y_R^l g'^2 m_{N_i}}{2(16\pi^2) M_Z \sin\theta_w \cos\beta}O_{Ri\tilde{H}_d^0}O_{Li\tilde{B}} \cos\theta_{\tilde{l}} \sin\theta_{\tilde{l}} \left[\frac{f_{n2}(x_{1i})}{m_{\tilde{l}_{R1}}^2} - \frac{f_{n2}(x_{2i})}{m_{\tilde{l}_{R2}}^2}\right],$$
$$\tag{3.8}$$

where A_{Rin1} is the amplitude that involves an external chirality flip of the muon and A_{Rin2} involves a flip at the Higgsino vertex. Here $O_{Ri\tilde{H}_d^0}$ and $O_{Li\tilde{B}}$ are the Higgsino and bino content of N_i, respectively (i.e., the corresponding elements in the orthogonal matrices that diagonalize the gaugino mass matrix squared), and $Y_R^l = Y^{l^c} = +1$. To lowest non-vanishing order in M_Z, the neutralino mixings are (dropping the subscripts L and R from now on):

$$O_{1\tilde{B}}(\mu_d \ll M_1) = O_{1\tilde{H}_d^0}(\mu_d \gg M_1) = \frac{\cos\beta \sin\theta_w M_Z \mu_d}{M_1^2 - \mu_d^2}, \tag{3.9}$$

$$O_{2\tilde{B}}(\mu_d \gg M_1) = O_{2\tilde{H}_d^0}(\mu_d \ll M_1) = -\frac{\cos\beta \sin\theta_w M_Z M_1}{M_1^2 - \mu_d^2}, \tag{3.10}$$

and $O_{i(\tilde{B},\tilde{H}_d^0)} = 1$ in the appropriate limits. The functions $f_{nj}(x_i)$, with $x_{ik} = m_{N_k}^2/m_{\tilde{l}_{Ri}}^2$, with $j = 1, 2$, come from integrating over the loops in the diagrams:

$$f_{n1}(x) = \frac{1}{2(1-x)^4}(1 - 6x + 3x^2 + 2x^3 - 6x^2 \ln x), \tag{3.11}$$

$$f_{n2}(x) = \frac{1}{(1-x)^3}(1 - x^2 + 2x \ln x). \tag{3.12}$$

Finally, the amplitudes for the left-handed sleptons can be obtained from the right-handed slepton results by doing the replacements

$$A_{\gamma\text{dip}}^R \to A_{\gamma\text{dip}}^L \quad \text{upon} \quad (Y_R^l, m_{\tilde{l}_{Ri}}^2) \to (Y_L^l, m_{\tilde{l}_{Li}}^2). \tag{3.13}$$

Inserting the results in Eqs. (3.9)-(3.10) into (3.7)-(3.8), we see that to lowest vanishing order in M_Z, $BR(\mu \to e\gamma)$ is independent of $\tan\beta$. We can also see explicitly that when the two slepton masses are degenerate, the branching ratio vanishes, as expected from the super GIM mechanism.

As an aside, it is also straightforward to see what happens to the results when the mass hierarchy between the slepton and the neutralino are inverted. The loop functions satisfy the identities,

$$f_{n1}(x) + f_{n1}\left(\frac{1}{x}\right) = \frac{1}{2}, \tag{3.14}$$

$$x f_{n2}(x) - f_{n2}\left(\frac{1}{x}\right) = 0. \tag{3.15}$$

We are now in a position to discuss the amplitudes in various limits. In the bino-like limit $M_1 \ll \mu_d$, one sees that A_{R1n1} dominates, as A_{Rin2} is of order M_1/μ_d.

When N_1 becomes $\tilde{H}_d^0$-like, there is a cancellation between the amplitudes involving a chirality flip on the external muon line, and the one with the flip occurring at the muon Yukawa vertex. The dominant diagram in the $\tilde{B}$-like case, A_{R1n1}, is now suppressed by μ_d^2/M_1^2, the same suppression factor appears A_{R1n2}. So the dominant amplitudes come from the diagrams involving a $\tilde{B}$-like neutralino exchange. Note that A_{R2n2} has an opposite sign compared to A_{R2n1} and the total amplitude can vanish for some choice of parameters.

In Figs. 3.2(a)-3.2(d), we show the allowed regions in MRSSM parameter space with right-handed slepton mixing that satisfy the bound $BR(\mu \to e\gamma) < 1.2 \times 10^{-11}$ [47, 48].

The situation is drastically different in the case of left-handed slepton mixing. The hypercharge of the left-handed leptons ($Y_L^l = -1/2$), has an opposite sign to the right-handed lepton hypercharge, and so the amplitudes interfere constructively, instead of destructively as in the case of right-handed slepton mixing. This leads to a more severe bound on the allowable regions in parameter space for left-handed slepton mixing. This is shown in Figs. 3.3(a)-3.3(d).

3.2.2. $\mu \to e$ Conversion in a Nucleus

The conversion of a muon into an electron can give a qualitatively distinct bound on $\mu \leftrightarrow e$ slepton mixing because there are several types of operators beyond those that contribute to $\mu \to e\gamma$. We discuss the operators for $\mu \to e$ conversion, one-by-one, in this section.

The $\mu \to e$ conversion amplitude is dominated by coherent processes, and so we only took the quark vector currents into account. The operators that contribute to the incoherent terms, $\bar{q}\gamma^5 q$, $\bar{q}\gamma^\mu\gamma^5 q$, and $\bar{q}\sigma^{\mu\nu}q$ have been neglected. This leaves us with the scalar and vector current, $\bar{q}q$ and $\bar{q}\gamma^\mu q$, respectively [53].

The only diagram that can contribute to a scalar quark current is the box diagram. Without left-right mixing of sleptons in the MRSSM, the dominant term, with bino couplings at each vertex, contains no chirality flip of the quarks, and is therefore a vector current. We also take the quark current to be non-relativistic to simplify the calculation involving the magnetic dipole term. Thus, the amplitude
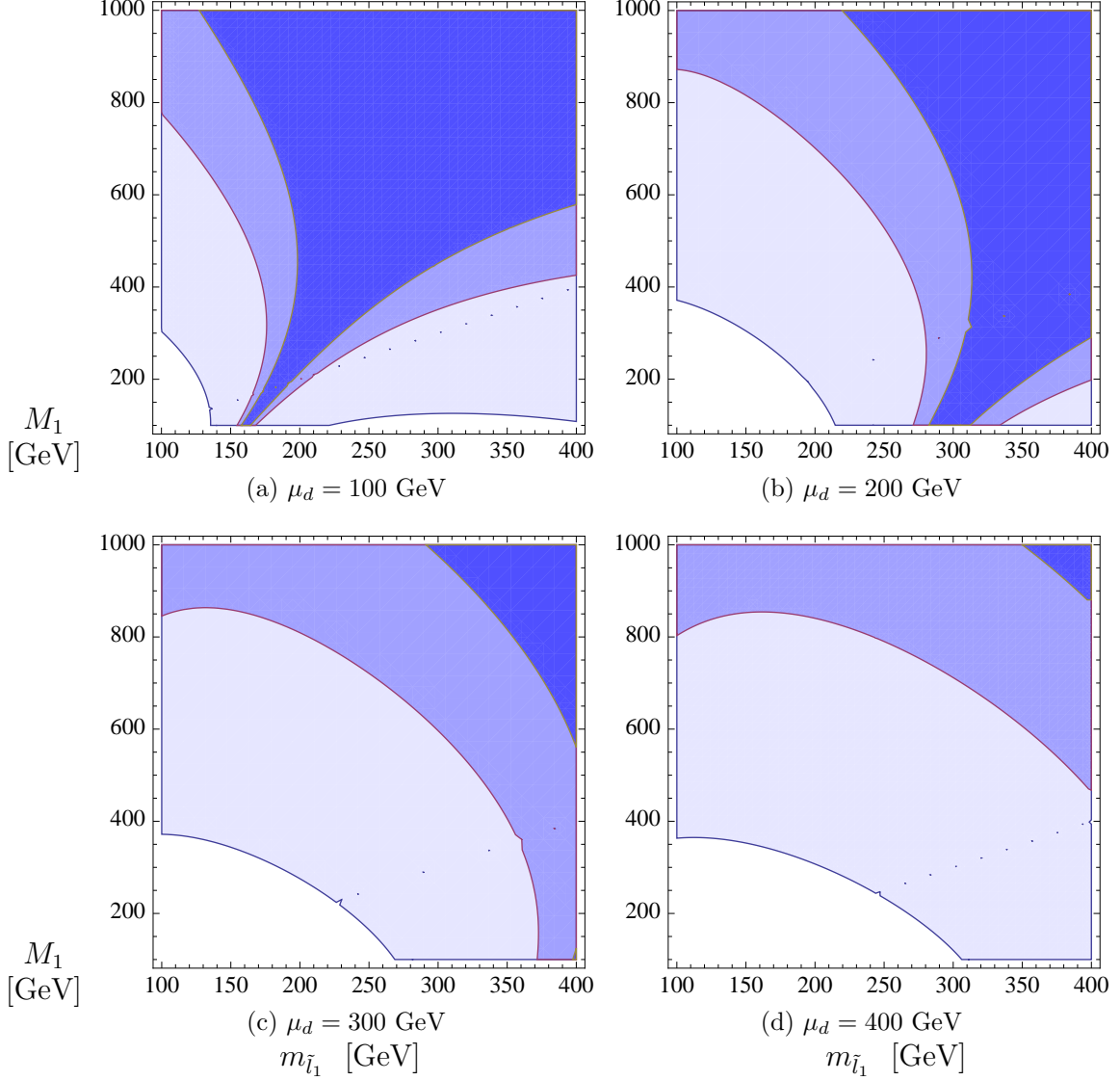
FIGURE 3.2: Regions in parameter space (shaded) that satisfy the $\mu \to e\gamma$ bound for right-handed slepton mixing. The mass of the heavier slepton is set to $1.5m_{\tilde{l}_1}$. From light to dark, the shaded areas denote mixing with $\sin 2\theta_{\tilde{l}} = 0.1, 0.5$ and 1, respectively. The funnel regions in the plots with $\mu_d = 100, 200$ GeV is caused by the cancellation between the amplitudes involving the bino-like and the $\tilde{H}_d^0$-like neutralinos.
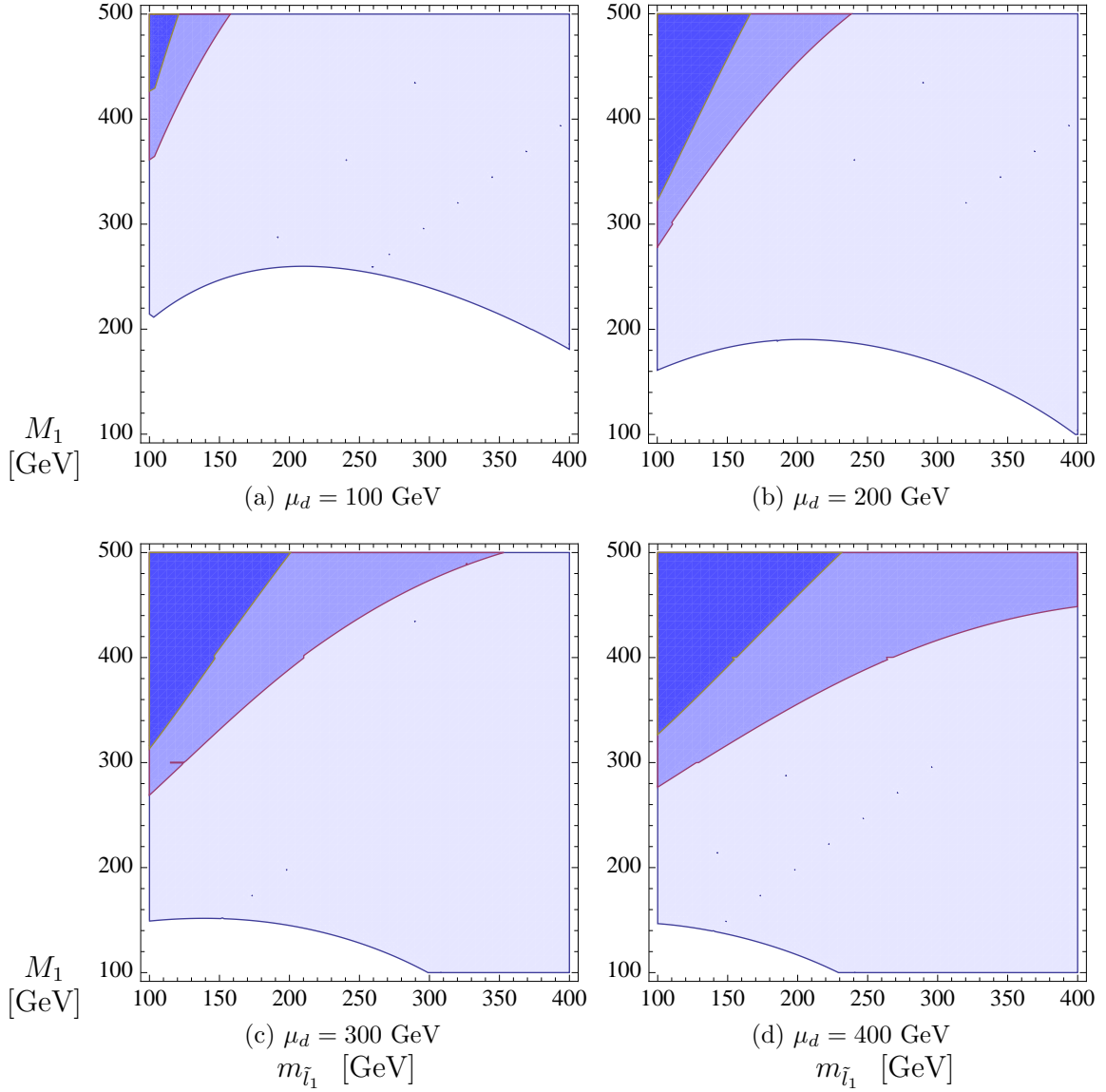
FIGURE 3.3: Same as Fig. 3.2 but for left-handed slepton mixing. We have restricted $M_1 < 500$ GeV since contributions from wino-like charginos not been included (see Sec. 3.1. for a discussion).

for $\mu \to e$ conversion is well approximated, for our purposes, by only taking quark vector currents into account.

The diagrams we consider are the photon penguin, the Z penguin, and the box diagram shown in Figs. 3.4,3.5,3.6,3.7. We only take the dominant terms of the box and the Z penguin amplitude into account: that is, the terms involving the bino coupling at each vertex which does not contain any chirality flips of the external fermions. The effective Lagrangian at the parton level can be written as [53]

$$
\begin{aligned}
\mathscr{L}_{eff} &= \sum_{q=u,d} -Q_q e^2 \bar{e} \left[\gamma^\mu (A_\gamma^L P_L + A_\gamma^R P_R) + \frac{m_\mu}{k^2} i\sigma^{\mu\nu} k_\nu (A_{\gamma\mathrm{dip}}^L P_L + A_{\gamma\mathrm{dip}}^R P_R) \right] \mu \bar{q}\gamma_\mu q \\
&\quad + e^2 \sum_{q=u,d} \bar{e}\gamma^\mu[(A_Z^L + A_{\mathrm{box}}^{qL})P_L + (A_Z^R + A_{\mathrm{box}}^{qR})P_R]\mu \bar{q}\gamma_\mu q, \quad\quad\quad (3.16)
\end{aligned}
$$

where Q_q is the quark electric charge, $k^2 \sim -m_\mu^2$ is the momentum transfer, $A_{\gamma,Z}^{L,R}$ and $A_{\gamma\mathrm{dip},Z}^{L,R}$ correspond to the γ-penguin and Z-penguin, respectively, and $A_{\mathrm{box}}^{q(L,R)}$ corresponds to the box diagram.

The most severe upper bound to date is on the conversion rate ratio with a gold nucleus $BR(\mu \to e)_{Au} \equiv \Gamma(\mu^- \, \mathrm{Au} \to e^- \, \mathrm{Au})/\Gamma(\mu^- \, \mathrm{Au})_{\mathrm{capture}} < 7 \times 10^{-13}$ from SINDRUM II [49]. Because of the large number of protons in the gold nucleus, the distortion to the muon wave function from a plane wave must be taken into account when evaluating the overlap between the muon and nucleus wavefunctions. This has been done in Ref. [80], and we will use their overlap integrals, with the neutron density determined from pionic atom experiments (method 2 in [80]). Other nuclei could also be of interest, particularly as a way to distinguish different models [81]. The conversion rate is

$$
\Gamma_{\mu \to e} = 4m_\mu^5 e^4 |\mathscr{A}_{\gamma\mathrm{dip}}^L + \mathscr{A}_\gamma^R + \mathscr{A}_{box}^R + \mathscr{A}_Z^R|^2 + (L \leftrightarrow R), \quad\quad\quad (3.17)
$$

where,

$$\mathscr{A}_{\gamma\text{dip}}^{L} = -\frac{1}{8e}A_{\gamma\text{dip}}^{L}D, \qquad (3.18)$$

$$\mathscr{A}_{\gamma}^{R} = A_{\gamma}^{R}V^{(p)}, \qquad (3.19)$$

$$\mathscr{A}_{box}^{R} = -(2A_{\text{box}}^{uR} + A_{\text{box}}^{dR})V^{(p)} - (A_{\text{box}}^{uR} + 2A_{\text{box}}^{dR})V^{(n)}, \qquad (3.20)$$

$$\mathscr{A}_{Z}^{R} = [(2Z_{u} + Z_{d})V^{(p)} + (2Z_{d} + Z_{u})V^{(n)}]A_{Z}^{R}, \qquad (3.21)$$

where $Z_{q} = (Z_{q_{R}} + Z_{q_{L}})/2$, with $Z_{q_{(L,R)}} = I_{L,R}^{q} - Q\sin^{2}\theta_{w}$, $I_{L}^{u} = 1/2$, $I_{L}^{d} = -1/2$ for up and down type quarks, and $I_{R}^{q} = 0$. The first term in Eq. (3.17), proportional to $|\mathscr{A}_{\gamma\text{dip}}^{L} + \mathscr{A}_{\gamma}^{R} + \mathscr{A}_{box}^{R} + \mathscr{A}_{Z}^{R}|^{2}$, corresponds to slepton mixing in the right-handed sector, while the second term proportional to $|\mathscr{A}_{\gamma\text{dip}}^{R} + \mathscr{A}_{\gamma}^{L} + \mathscr{A}_{box}^{L} + \mathscr{A}_{Z}^{L}|^{2}$, corresponds to to slepton mixing in the left-handed sector. The coefficients D and $V^{(p,n)}$ are to the overlap integrals of the muon and the nucleus for the leptonic dipole and vector (proton, neutron) operators. We used, for a gold nucleus, $D = 0.167$, $V^{(p)} = 0.0859$, $V^{(n)} = 0.108$ from Ref. [80].

Now we will discuss each diagram below. We will present the results for both left- and right-handed slepton mixing. But, for simplicity, we will only discuss the case of right-handed slepton mixing explicitly. The amplitudes corresponding to left-handed slepton mixing can be obtained from the right-handed ones by replacing the appropriate hypercharges and slepton masses. Note that for the Z-penguin, there is also an additional minus sign after the replacement of hypercharges and slepton masses.
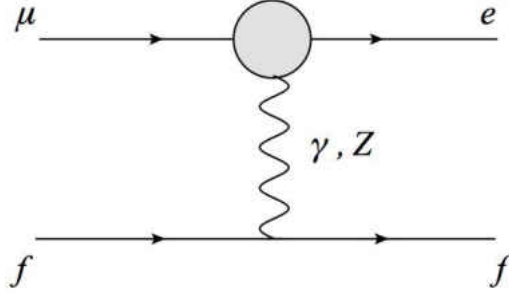
FIGURE 3.4: Schematic diagram illustrating the set of penguin contributions to $\mu \to e$ conversion (for $f = q$) as well as $\mu \to 3e$ (for $f = e$). The blob in the figure arises from both charge radius subdiagrams shown in Fig. 3.5, as well as Z penguin subdiagrams, the dominant ones shown in Fig. 3.6.

3.2.2.1. Charge Radius

The charge radius amplitude $A_\gamma^{L,R}$ comes from the γ-penguin, without a chirality flip of the leptons. The dominant term is the one involving the $\tilde{B}$-like neutralino in the loop, with $\tilde{B}$ coupling at each vertex connecting a lepton. The other terms are suppressed either by the muon Yukawa or by two powers of the small bino content in the $\tilde{H}_d^0$-like neutralino. The contributions to the effective vertex of the charge radius is shown in Fig. 3.5. Summing over these contributions give[1],

$$A_\gamma^R = \frac{g'^2 (Y_R^l)^2}{576\pi^2} \frac{\sin 2\theta_{\tilde{l}}}{m_{\tilde{l}_1}^2} f_\gamma \left(\frac{M_1^2}{m_{\tilde{l}_1}^2} \right) - (m_{\tilde{l}_1} \to m_{\tilde{l}_2}), \tag{3.22}$$

with

$$f_\gamma(x) = \frac{1}{1 - x^4} (2 - 9x + 18x^2 - 11x^3 + 6x^3 \ln x). \tag{3.23}$$

---

[1]We have checked that, even when $\mu_d = M_1$, the value given by this expression differs to the exact one by $\lesssim 1\%$. So this expression is valid over all ranges of M_1 and μ_d. The discrepancy comes from the small mass splitting of the neutralinos when the gaugino and Higgsino masses are degenerate. We have used the exact expression in our numerical analysis.
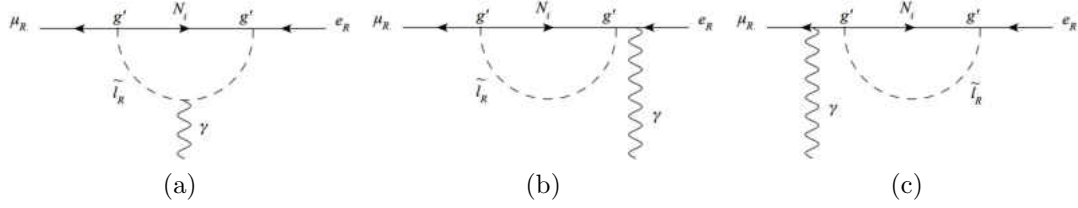
FIGURE 3.5: Contributions to the effective vertex from the charge radius operator. Graph (c) is suppressed by a factor of m_e^2/m_μ^2 compared to (b), and can be ignored in the limit of vanishing electron mass. Also in this limit, graph (b) exactly cancels graph (a) for vanishing photon momentum, satisfying the Ward identity. Only right-handed slepton flavor mixing diagrams are shown, while left-handed slepton flavor mixing diagrams are obtained by swapping $L \leftrightarrow R$.

3.2.2.2. Magnetic Dipole

The magnetic dipole amplitude $A_{\gamma\text{dip}}^{L,R}$ is the one that appears in $\mu \to e\gamma$, which was discussed in detail in the last section. For right-handed slepton mixing, the amplitude of the dipole term is smaller than the charge radius term, $A_\gamma^{L,R}$, due to the destructive interference between amplitudes involving chirality flips at different locations in the diagram. The situation reverses in the case of left-handed slepton mixing, where both terms contributes and the magnitude becomes larger than the charge radius term.

3.2.2.3. Z-penguin

The Z-penguin contribution contains diagrams in Fig. 3.5, with the photon replaced by the Z boson. The contribution coming from this set of diagrams is suppressed by $O(m_\mu^2/M_Z^2)$ compared to the charge radius so is negligible. Then, the dominant term is the one involving a Higgsino-Higgsino-Z vertex, shown in Fig. 3.6.

We find that the Z-penguin is sub-dominant in a large region of the parameter space. The Z-penguin is the only amplitude that is sensitive to $\tan \beta$, and in the

(a) (b)
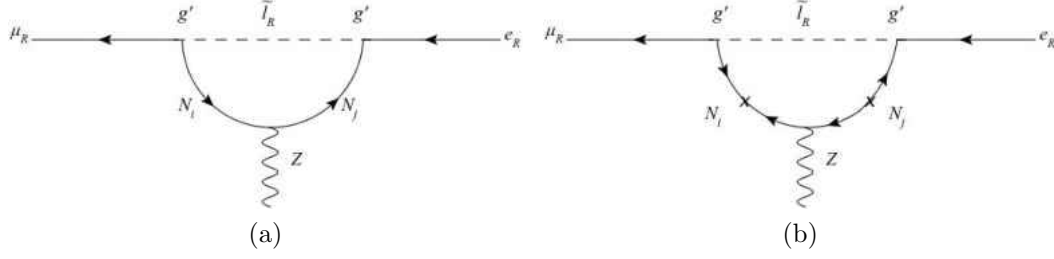
FIGURE 3.6: Contributions to the effective vertex from the Z penguin. Diagram (a) gives the term proportional to f_Z in which the Z boson couples to the R-partner of the down type Higgsino, $\psi_{\tilde{H}_d^0}$, and (b) gives the term proportional to g_Z, with Z coupling to $\tilde{H}_d^0$. Only right-handed slepton flavor mixing diagrams are shown, while left-handed slepton flavor mixing diagrams are obtained by swapping $L \leftrightarrow R$.

limit $M_Z \ll M_N$, it scales as $\cos^2 \beta$. The Z-penguin amplitude is

$$A_Z^R = \frac{(Y_R^l)^2 g'^2}{64\pi^2} \frac{\sin 2\theta_{\tilde{l}}}{M_Z^2 \sin^2 \theta_w \cos^2 \theta_w} \sum_{i,j=1}^{2} \omega_{ij}, \tag{3.24}$$

where

$$\omega_{ij} = O_{Li1}O_{Lj1}\left[O_{Li2}O_{Lj2}f_Z\left(\frac{M_{N_i}^2}{m_{\tilde{l}_1}^2}, \frac{M_{N_j}^2}{m_{\tilde{l}_1}^2}\right) - 2O_{Ri2}O_{Rj2}g_Z\left(\frac{M_{N_i}^2}{m_{\tilde{l}_1}^2}, \frac{M_{N_j}^2}{m_{\tilde{l}_1}^2}\right)\right] - (m_{\tilde{l}_1} \to m_{\tilde{l}_2}). \tag{3.25}$$

The functions $f_Z(x_i, x_j)$ and $g_Z(x_i, x_j)$ are[2]

$$f_Z(x_i, x_j) = \ln x_i + \frac{1}{x_i - x_j}\left[\frac{x_i^2 \ln x_i}{1 - x_i} - \frac{x_j^2 \ln x_j}{1 - x_j}\right], \tag{3.26}$$

$$g_Z(x_i, x_j) = \frac{\sqrt{x_i x_j}}{x_i - x_j}\left[\frac{x_i \ln x_i}{1 - x_i} - \frac{x_j \ln x_j}{1 - x_j}\right]. \tag{3.27}$$

---

[2]Note that the function f_Z appears to contain a log term that is asymmetric in the two neutralino lines in the loop, not as one would expect. But remember that this log term is subtracted by one containing the heavier slepton mass, and the final result is symmetric in the neutralinos and anti-symmetric in the sleptons, as expected.
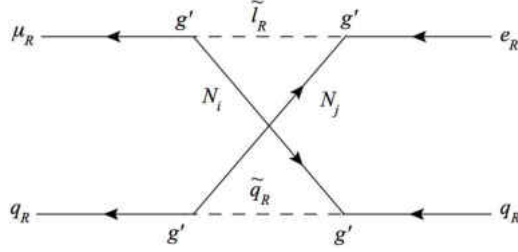
FIGURE 3.7: The box Feynman diagram for $\mu \to e$ conversion. Due to the conservation of R-charges, the chirality of the squarks must be the ones shown in the diagrams. Only right-handed slepton flavor mixing diagrams are shown, while left-handed slepton flavor mixing diagrams are obtained by swapping $L \leftrightarrow R$ everywhere.

Note that the Z-penguin effective vertex does not explicitly depend on $1/M_{\text{SUSY}}^2$ as in the case of all other amplitudes. This corresponds to an operator of dimension-4. This is perfectly fine, because the weak symmetry is broken, so the weak current is not conserved. However, it is required that in the limit of unbroken electroweak symmetry, this effective vertex vanishes. This is easy to check in the limit $M_Z \to 0$. In this limit, the neutralinos we consider do not mix [c.f., Eq. (A.2)]. But the amplitude for the Z-penguin contain at least two powers of the neutralino mixing matrix elements, regardless of whether it is bino-like or Higgsino-like. Therefore this operator vanishes in the limit $M_Z \to 0$, when the electroweak symmetry is unbroken.

For left-handed sleptons, the Z amplitude can be obtained by replacing the appropriate hypercharges and slepton masses, as well as an additional factor of (-1). This sign change arises from the NNZ coupling, in contrast to $N^c N^c Z$ in the case of right-handed sleptons.

3.2.2.4. Box Diagram

For the box diagram, the dominant term is the one containing bino couplings at all four vertices,

$$A_{box}^{qR} = \frac{(Y_R^l)^2 g'^4 \sin 2\theta_{\tilde{l}}}{64\pi^2 e^2 m_{\tilde{l}_1}^2}\left[(Y_R^q)^2 j_4\left(\frac{M_1^2}{m_{\tilde{l}_1}^2}, \frac{M_1^2}{m_{\tilde{l}_1}^2}, \frac{m_{\tilde{q}_R}^2}{m_{\tilde{l}_1}^2}\right)\right] - (m_{\tilde{l}_1} \to m_{\tilde{l}_2}), \qquad (3.28)$$

where

$$
\begin{aligned}
j_4(x_i, x_j, y) &= \frac{x_i^2 \ln x_i}{(1-x_i)(x_i-x_j)(x_i-y)} - \frac{x_j^2 \ln x_j}{(1-x_j)(x_i-x_j)(x_j-y)} \\
&+ \frac{y^2 \ln y}{(1-y)(x_i-y)(x_j-y)}.
\end{aligned}
\qquad (3.29)
$$

We can compare the box amplitude with $A_\gamma^{L,R}$ by approximating $V^{(p)} \simeq V^{(n)}$, giving

$$\left|\frac{A_{box}^R}{A_\gamma^R}\right| = \frac{9(g')^2}{e^2}\frac{j_4(x,x,y)}{f_\gamma(x)}[3(Y_R^d)^2 + 3(Y_R^u)^2] \simeq 19\frac{j_4(x,x,y)}{f_\gamma(x)}, \qquad (3.30)$$

where $x = M_1^2/m_{\tilde{l}_1}^2$ and $y = m_{\tilde{q}}^2/m_{\tilde{l}_1}^2$. The right hand side is plotted in Fig. 3.8. We can see that the box can give a large contribution the total amplitude when the squarks are not far heavier than the sleptons.

3.2.2.5. Numerical Results

We took $\tan \beta = 3$ for our analysis. The amplitudes contributing to $\mu \to e$ conversion in gold are shown in Fig. 3.9 for right-handed slepton mixing, and in Fig. 3.10 for left-handed slepton mixing. The slepton mixing angles are taken to be maximal. For comparison, we also drew the line where the experimental bound on

63
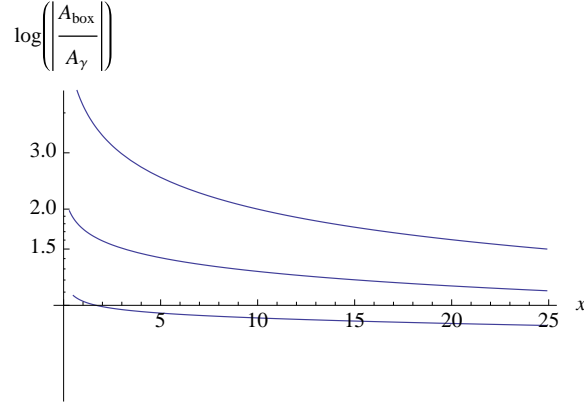
FIGURE 3.8: A plot of the right hand side of Eq. (3.30), $19j_4(x, x, y)/f_\gamma(x)$, where $x = M_1^2/m_{\tilde{l}_1}^2$ and $y = m_{\tilde{q}}^2/m_{\tilde{l}_1}^2$. The contours are $y = 1, 10, 25$ from top to bottom. The box amplitude is larger than the electromagnetic term when the contour is above the x-axis.

the amplitude would be, as if only one amplitude were contributing to the conversion rate.

For right-handed sleptons, either the charge radius or the box diagram dominate over other contributions. Each of these amplitudes exceeds the bound alone and they interfere constructively with each other. Therefore, maximal right-handed slepton mixing is excluded throughout the parameter space we explore. The magnetic dipole destructively interferes with the box and the charge radius diagrams, at small slepton masses before the magnetic dipole vanishes. However, this cancellation is insufficient to bring the amplitudes below the bound.

In the left-handed slepton mixing case, the box diagram is suppressed by the left-handed quark hypercharge, and is much smaller. Also, the two largest amplitudes, the charge radius and the magnetic dipole, destructively interfere with each other, resulting in the funnel region shown in Fig. 3.12.

For both right-handed and left-handed slepton mixing, the Z-penguin is sub-dominant. Moreover, for larger values of $\tan \beta$, the Z-penguin will be even more

suppressed, since it is directly proportional to $\cos^2 \beta = 1/(1 + \tan^2 \beta)$ to lowest order, in the limit $M_Z \ll M_N$. We show the exclusion plots for $\mu \to e$ conversion in Figs. 3.11 and 3.12.

3.2.3. $\mu \to 3e$

Finally, we investigate the decay $\mu^- \to e^- e^+ e^-$. The diagrams that contribute to this decay are similar to the process $\mu \to e$ in a nucleus. While the amplitudes for this decay are not enhanced by nuclear factors as in the case of $\mu \to e$ conversion, there is a log enhancement proportional to $\log m_\mu/m_e$, arising from an infrared divergence cutoff by the electron mass.

All of the diagrams in $\mu \to 3e$ can be obtained from the $\mu \to e$ conversion diagrams by replacing the quark line by an electron line with outgoing e^+ and e^-. All diagrams except the box are the same and will not be discussed here. For the box, conservation of R-charges enforces that both sleptons in the loop be of the same "chirality". The box amplitude for $\mu \to 3e$ for right-handed sleptons is

$$B_{box}^R = \frac{(g' Y_l^R)^4}{16\pi^2 e^2} \sin 2\theta_{\tilde{l}} \sum_{i,k=1}^{2} \frac{(-1)^{i+1}}{m_{\tilde{l}_i}^2} U_{kj4} \left(\frac{M_1^2}{m_{\tilde{l}_i}^2}, \frac{M_1^2}{m_{\tilde{l}_i}^2}, \frac{m_{\tilde{l}_k}^2}{m_{\tilde{l}_i}^2} \right), \qquad (3.31)$$

(a) $\mu_d = 100$ GeV, $m_{\tilde{l}} = 200$ GeV

(b) $\mu_d = 200$ GeV, $m_{\tilde{l}} = 200$ GeV

(c) $M_1 = \mu_d = 100$ GeV

(d) $M_1 = \mu_d = 200$ GeV
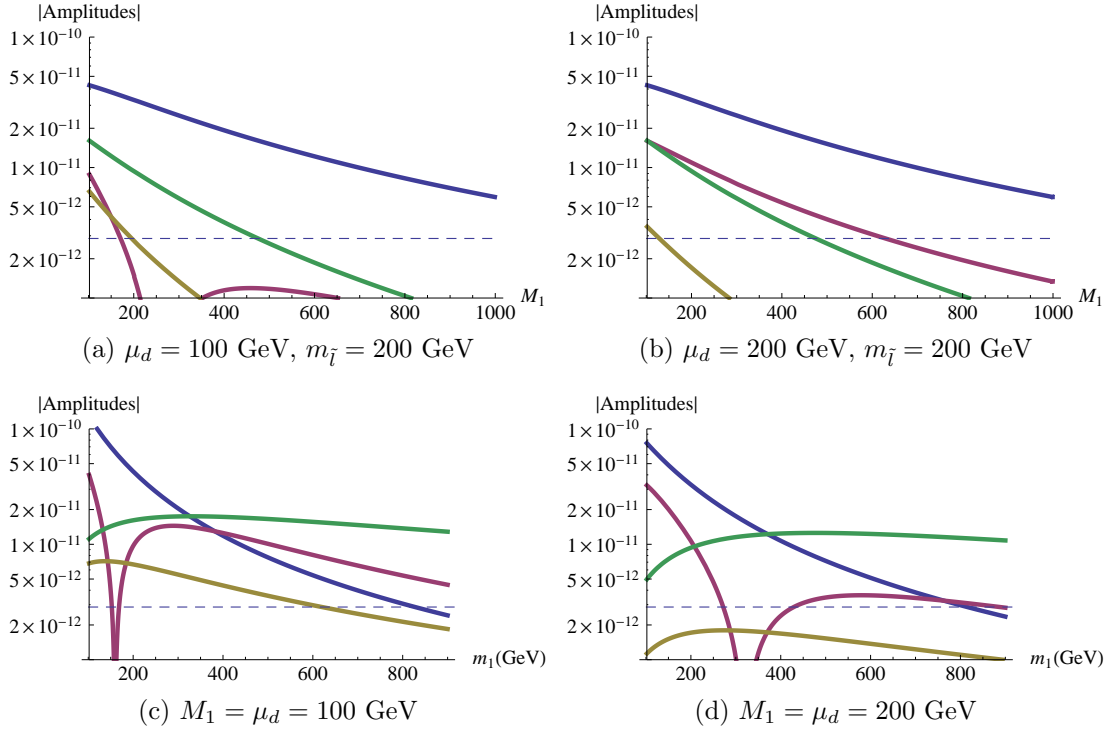
FIGURE 3.9: The magnitudes of various amplitudes at maximal mixing of right-handed sleptons with degenerate squark masses of 1 TeV (i.e., the terms in Eq. (3.17) before taking the square). The contours are, $\mathscr{A}_\gamma^R$ (blue), $\mathscr{A}_{box}^R$ (green), $|\mathscr{A}_{\gamma\mathrm{dip}}^R|$ (red), and $-\mathscr{A}_Z^R$ (brown). The dashed line corresponds to the bound on $\mu \to e$ conversion as if only one amplitude were contributing. One can see that there are regimes where only the box and the charge radius amplitudes contribute significantly [subfigures (a) and (b), especially in the high M_1 regions in these figures], and where all four amplitudes contribute significantly [subfigure (c)]. In subfigure (d), the magnetic dipole amplitude reaches zero near $m_{\tilde{l}_1} \sim 330$ GeV. This coincides with the "funnel" region in the parameter space plot for $\mu \to e\gamma$, Fig. 3.2(b).

(a) $\mu_d = 100$ GeV, $m_{\tilde{l}} = 200$ GeV

(b) $\mu_d = 200$ GeV, $m_{\tilde{l}} = 200$ GeV

(c) $M_1 = \mu_d = 100$ GeV

(d) $M_1 = \mu_d = 200$ GeV
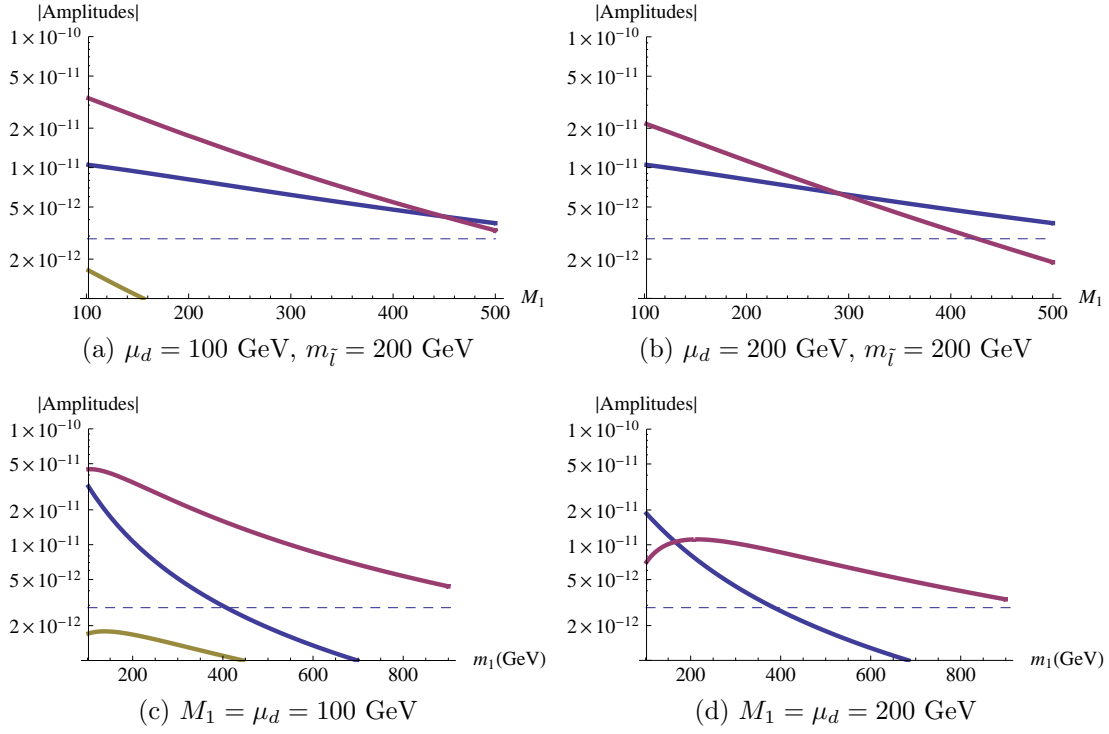
FIGURE 3.10: Same as Fig. 3.9 but with left-handed slepton mixing instead. The contours are, $\mathscr{A}_\gamma^L$ (blue), $-\mathscr{A}_{box}^L$ (green), $-\mathscr{A}_{\gamma\mathrm{dip}}^L$ (red), and $\mathscr{A}_Z^L$ (brown). The magnetic dipole and the charge radius amplitudes interfere destructively with each other, opening up a large region in the parameter space that satisfies $\mu \rightarrow e$ conversion. This forms the funnel regions in Fig. 3.12.
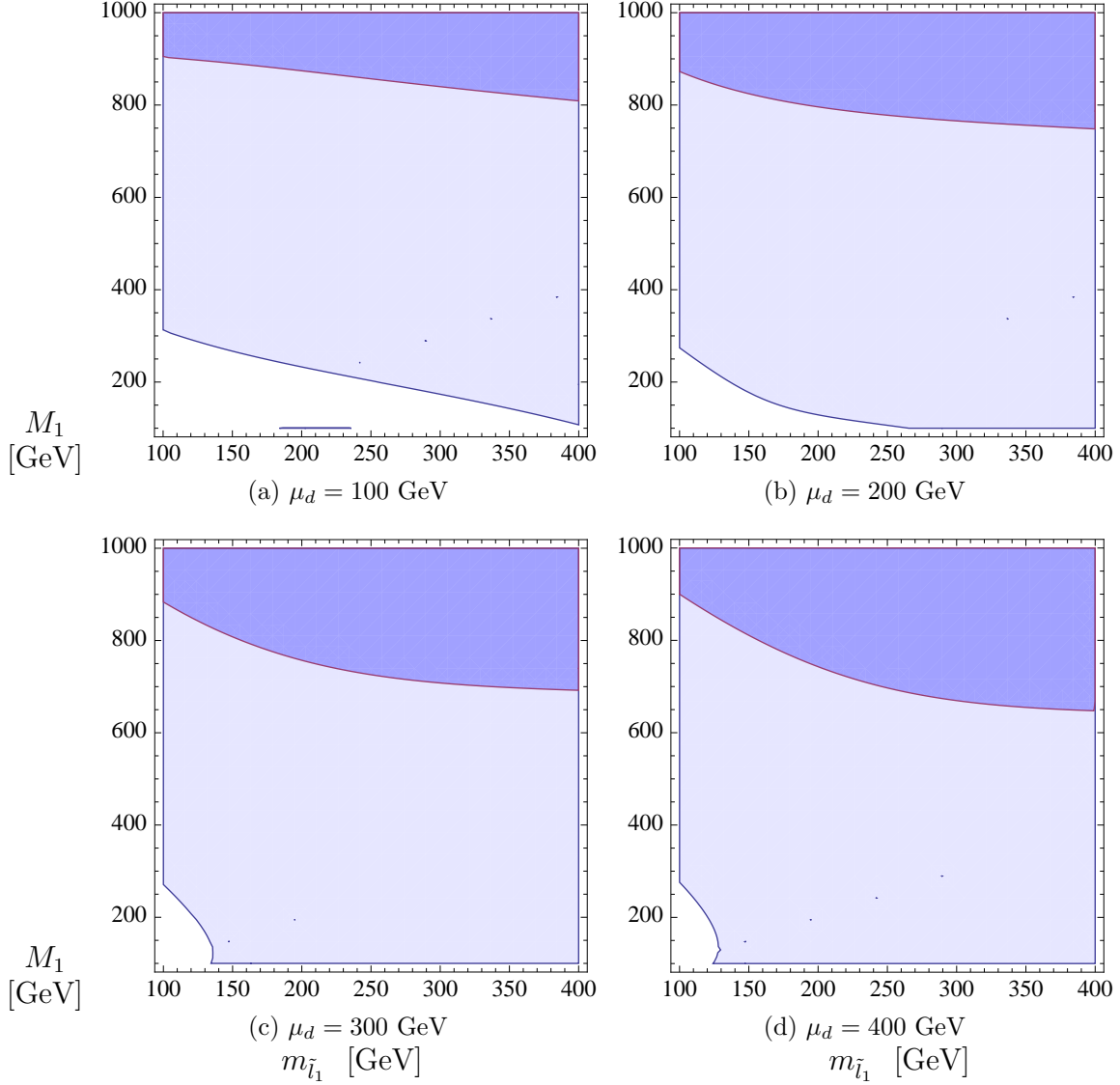
FIGURE 3.11: Allowable regions for $\mu \to e$ conversion in a gold nucleus with right-handed slepton mixing. From light to dark, the shaded areas denote mixing with $\sin 2\theta_{\tilde{l}} = 0.1, 0.5$ respectively. The squark masses are set to be degenerate at 1 TeV. Note that this completely rules out maximal mixing for right-handed sleptons in the sub-TeV range.

(a) $\mu_d = 100$ GeV

(b) $\mu_d = 200$ GeV

(c) $\mu_d = 300$ GeV

(d) $\mu_d = 400$ GeV

$m_{\tilde{l}_1}$ [GeV]

$m_{\tilde{l}_1}$ [GeV]

M_1 [GeV]
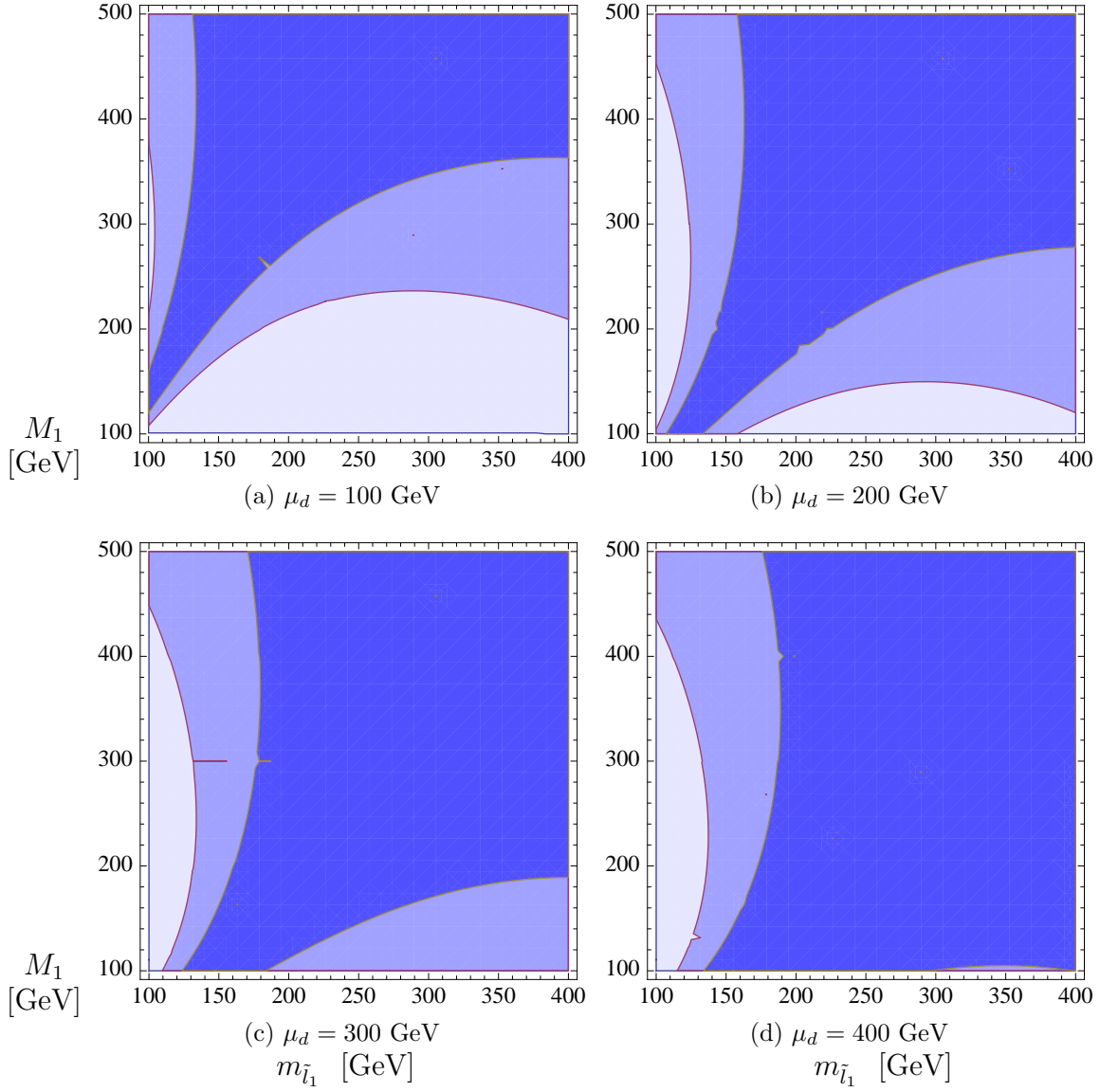
FIGURE 3.12: Same for Fig. 3.11 but with left-handed slepton mixing instead.

where $U_1 = \cos^2 \theta_{\tilde{l}}$ and $U_2 = \sin^2 \theta_{\tilde{l}}$. The factor $(-1)^{i+1}$ comes from the super-GIM mechanism. The rate for the decay $\mu \to 3e$ is

$$
\begin{aligned}
\Gamma_{\mu \to 3e} = \ &\frac{\alpha^2 m_\mu^5}{32\pi} [(A_\gamma^R)^2 - 4 A_\gamma^R A_{\gamma\text{dip}}^L + (A_{\gamma\text{dip}}^L)^2 \left(\frac{16}{3} \log \frac{m_\mu}{m_e} - \frac{22}{3} \right) \\
&+ \frac{1}{6} (B_{\text{box}}^R)^2 + \frac{2}{3} A_\gamma^R B_{\text{box}}^R - \frac{4}{3} A_{\gamma\text{dip}}^L B_{\text{box}}^R + \frac{2}{3} F_{RR}^2 + \frac{1}{3} F_{RL}^2 \\
&+ \frac{2}{3} B_{\text{box}}^R F_{RR} + \frac{4}{3} A_\gamma^R F_{RR} + \frac{2}{3} A_\gamma^R F_{RL} - \frac{8}{3} A_{\gamma\text{dip}}^L F_{RR} - \frac{4}{3} A_{\gamma\text{dip}}^L F_{RL}],
\end{aligned}
$$

(3.32)

where $F_{R\alpha} = A_Z^R Z_\alpha^l$, with $\alpha =$ L,R. The quantity Z_α is part of the electron-Z coupling; $Z_L = -1/2 + \sin^2 \theta_w$, and $Z_R = \sin^2 \theta_w$. The branching ratio of this process is obtained by dividing the rate by the muon decay rate. Note that the term proportional to $(A_{\gamma\text{dip}}^L)^2$ is enhanced by the log term, which is divergent in the limit of massless electrons. Our result for this divergent term agrees with [82].

In Figs. 3.13,3.14 we show the bounds on the MRSSM parameter space arising from satisfying the existing experimental bound $BR(\mu \to 3e) < 1.0 \times 10^{-12}$ from SINDRUM [50]. The bounds on the MRSSM parameter space from $\mu \to 3e$ are weaker than the combined bounds from $\mu \to e\gamma$ and $\mu \to e$ conversion.

3.3. Implications for Flavor Violation Signals at LHC

One of the most interesting implications of the MRSSM is that flavor mixing could be at or near maximal throughout virtually the entire slepton and squark sector [58] (save only perhaps for $\tilde{d}$-$\tilde{s}$ mixing [83]). For sleptons, this opens up the possibility of observing large μ-e mixing at colliders. Slepton mixing at colliders has been extensively studied [78, 84–102], though analyses have generally been relegated to
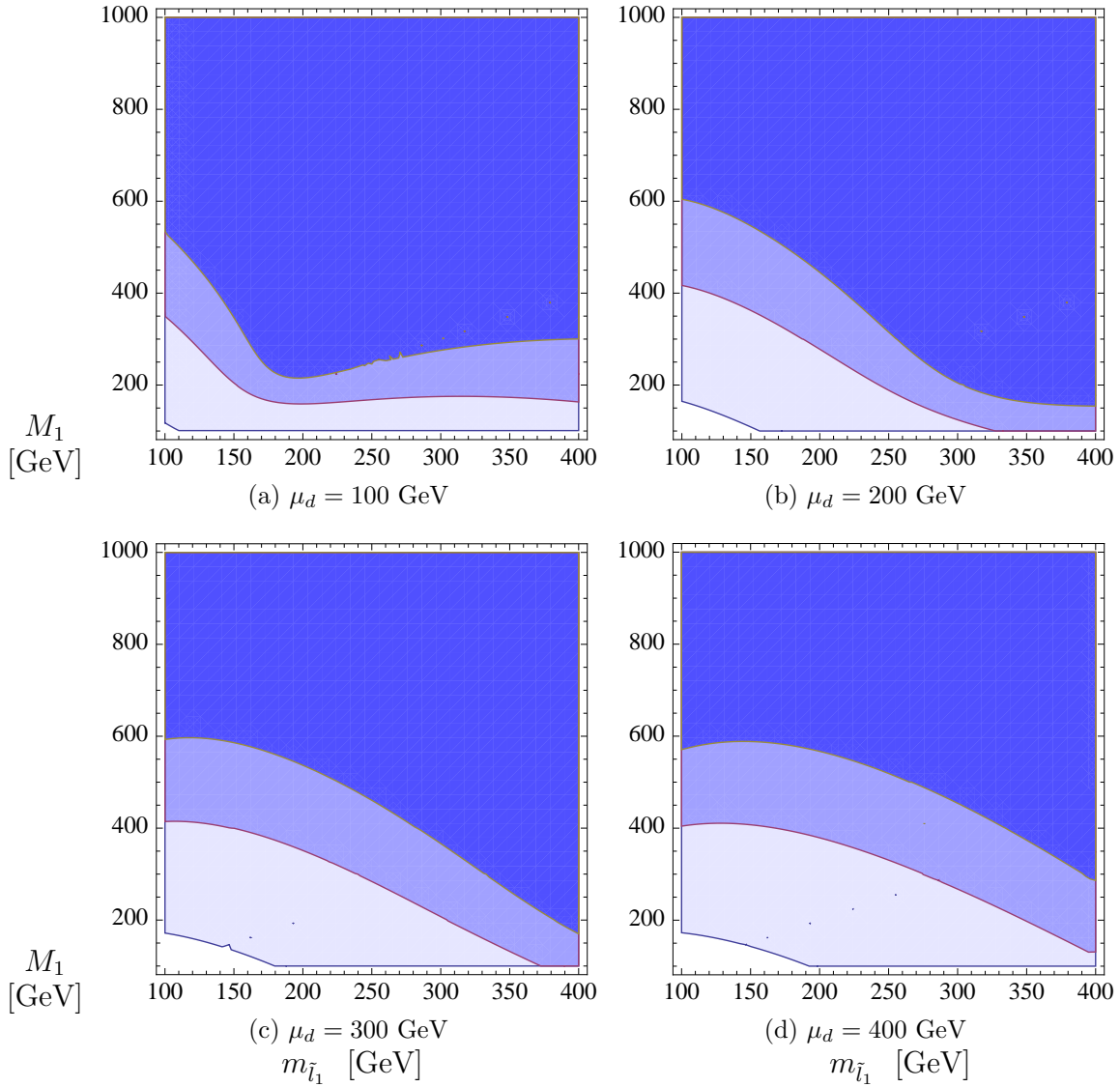
FIGURE 3.13: Regions of the parameter space that satisfy the $\mu \to 3e$ bound at different mixing angles of right-handed sleptons. The values of $\sin 2\theta_{\tilde{l}}$ are, from light to dark, 0.1, 0.5, 1.

71

(a) $\mu_d = 100$ GeV

(b) $\mu_d = 200$ GeV

(c) $\mu_d = 300$ GeV

(d) $\mu_d = 400$ GeV

$m_{\tilde{l}_1}$ [GeV]

$m_{\tilde{l}_1}$ [GeV]

M_1 [GeV]
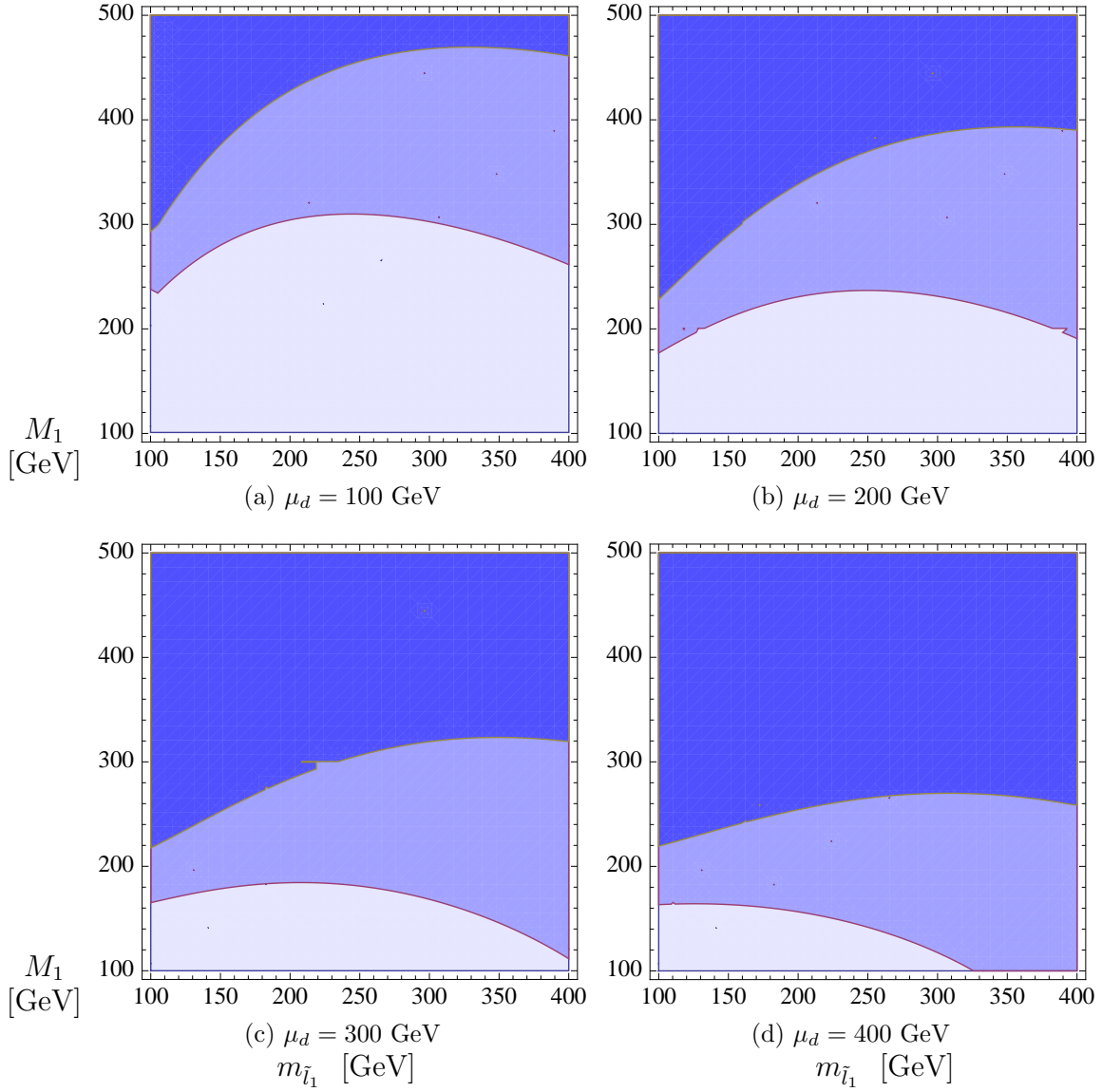
FIGURE 3.14: Same as Fig. 3.13 but with left-handed slepton mixing.

MSSM scenarios where the splitting between the e,μ eigenstates is very small, so as to satisfy the stringent LFV constraints. One of the most sensitive techniques to search for μ-e mixing is through the decay of a heavier neutralino to a lighter one through an on-shell slepton. This decay can arise at a large rate at the LHC starting with squark and/or gluino production, where the squark decays to the heavier neutralino and so on, such as

$$\tilde{q} \to q N_i \ ; \ N_i \to e^{\pm}/\mu^{\pm}\tilde{l}^{\mp} \ ; \ \tilde{l}^{\mp} \to \mu^{\mp}/e^{\mp}N_j \ . \tag{3.33}$$

The distinctive kinematic features in this cascade of 2-body decays can be utilized to extract the mass of the slepton through a kinematic edge (e.g. [103–108]).

In light of the bounds on the MRSSM parameter space that we have found from LFV processes, it is interesting to consider whether large mixing could still be seen at the LHC. A detailed collider study is beyond the scope of this chapter, nevertheless we can use our results to uncover characteristic regions of parameter space where $\sin 2\theta_l \sim 1$ simultaneous with several-hundred GeV sparticles, and thus, where large $\mu \leftrightarrow e$ mixing remains within reach of the LHC.

Closely examining Figs. 3.3(d),3.12(d),3.14(d), we discover one (small) region in the MRSSM parameter space where the left-handed slepton mixing angle can be maximal, $\sin 2\theta_l = 1$. For this region, and given first and second generation squark masses to be 1 TeV (consistent with what was assumed for the $\mu \to e$ conversion numerical results), we compute the leading order production cross sections and decay rates. We take the wino mass and the right-handed slepton masses to be 2 TeV for simplicity. The other gaugino masses in this region are $M_1 = 500$ GeV, $\mu_d = 400$ GeV, $\mu_u = 100$ GeV. The mass spectrum is shown in Table 3.1.

Particle	$\tilde{q}_{L,R}$	$\tilde{g}$	$N_3 \simeq \tilde{B}$	$C_2 \simeq \tilde{H}_d$	$N_2 \simeq \tilde{H}_d$	$\tilde{l}_{L2}$	$\tilde{l}_{L1}$	N_1
Mass (GeV)	1000	1000	502	400	400	270	180	100

TABLE 3.1: Mass spectrum

$M_{\tilde{g}}$ (TeV)	$\tilde{g}$-$\tilde{q}_{L,R}$	$\tilde{q}_R$-$\tilde{q}_L$	$\tilde{q}$-$\tilde{q}^*$	$\tilde{g}$-$\tilde{g}$	$\sigma(fb)$
1	810	120	50	330	1300
2	36	31	27	1.0	95
3	2.6	11	22	0.007	35

TABLE 3.2: Leading order production cross sections for squarks and gluinos at the LHC with $\sqrt{s} = 14$ TeV in the MRSSM.

Using MADGRAPH [109], we calculated the leading order squark and gluino production cross sections at LHC with $\sqrt{s} = 14$ TeV center of mass energy for several values of the Dirac gluino mass for those production modes allowed by R-symmetry in Table 3.2. One important observation made in Ref. [78] is that, for gluinos less than about 2 TeV, associated gluino-squark production gives the largest production rate of squarks.

The decay rates of the squarks, neutralinos, and charginos, computed using BRIDGE [110], can also be computed as a function of the mixing angle θ_l, shown in Table 3.3. For the particular point we considered, the first two generations of squarks decay overwhelmingly into the bino-like neutralino, N_3. The subsequent cascade decays into opposite flavor leptons have the rates $BR(N_3 \to e\mu N_1) = 0.14\sin^2 2\theta_l$, $BR(N_3 \to (ee/\mu\mu)N_1) = 0.27(\sin^4\theta_l + \sin^4\theta_l)$. If the gluino mass is 1 TeV, for example, then the $\tilde{g}\tilde{q}$ production leads to a total cross section of about 1 pb. With maximal slepton mixing, the cross section for opposite sign $e\mu$ events is expected to be of order 100 fb. Extracting this signal from background, particularly given the potentially problematic technique of flavor-subtraction, remains challenging. (See

Decaying particle	Decay modes	Branching ratios
$\tilde{q}$	qN_3	0.99
N_3	ZN_2	8×10^{-4}
	ZN_1	0.12
	$C_2^- W^+$	0.02
	$C_1^+ W^-$	0.22
	$\nu \tilde{\nu}_1$	0.19
	$\nu \tilde{\nu}_2$	0.13
	$e^- \tilde{l}_{L1}^+$	$0.19 \cos^2 \theta_l$
	$\mu^- \tilde{l}_{L1}^+$	$0.19 \sin^2 \theta_l$
	$e^- \tilde{l}_{L2}^+$	$0.13 \sin^2 \theta_l$
	$\mu^- \tilde{l}_{L2}^+$	$0.13 \cos^2 \theta_l$
$\tilde{l}_{L1}^+$	$C_1^+ \bar{\nu}$	0.11
	$N_1 e^+$	$0.88 \cos^2 \theta_l$
	$N_1 \mu^+$	$0.88 \sin^2 \theta_l$
$\tilde{l}_{L2}^+$	$C_1^+ \bar{\nu}$	0.16
	$N_1 e^+$	$0.84 \sin^2 \theta_l$
	$N_1 \mu^+$	$0.84 \cos^2 \theta_l$

TABLE 3.3: Decay branching ratios of the particles involved in the cascade decay $N_3 \to l^- \tilde{l}_L^+ \to l^- l'^+ N_1$ given the MRSSM parameters given in Table 3.1.

Ref. [78] for a discussion of signal plus background analysis of a non-minimal R-symmetric model.)

Just as in the MSSM, one can search for the kinematic endpoint in the invariant mass distribution of the leptons. In the MRSSM, however, the two slepton mass eigenstates are not near one another, and so two distinct and well-separated kinematic edges could in principle be extracted. This would be a striking signal of slepton flavor violation in the MRSSM. Note also that the electric charges of the leptons in this decay are fixed by the conversation of R-charges. For example, the anti-neutralino N_3^c can decay into $l^+ \tilde{l}_L^-$, the decay into the same final state for N_3 is forbidden. We show the overlapping regions allowed by all constraints in Figs. 3.15,3.16.
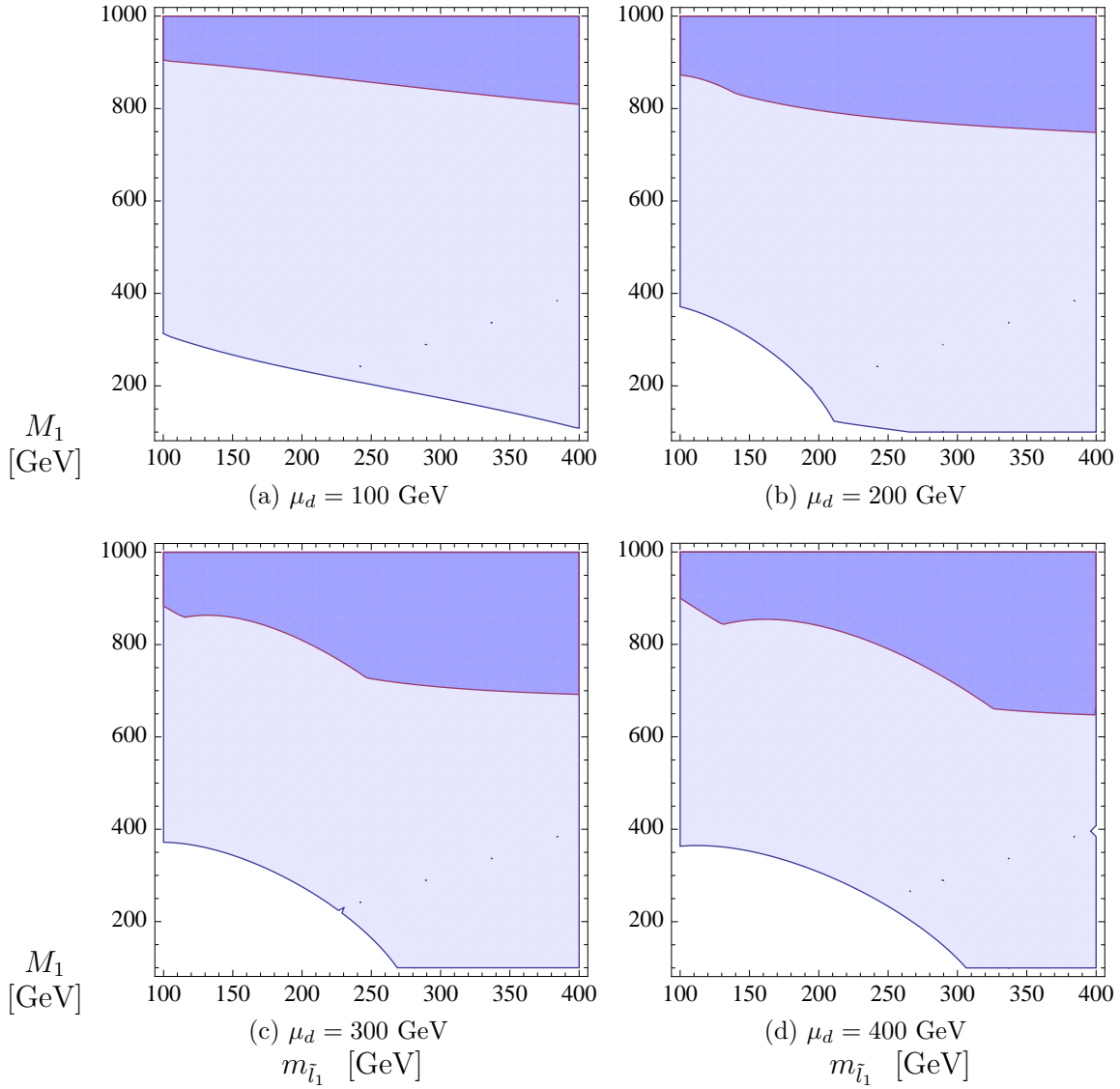
FIGURE 3.15: Regions allowed in the parameter space by combining the three constraints for right handed sleptons. The constraint from $\mu \to 3e$ is always less severe than the other two processes in the parameter space shown.
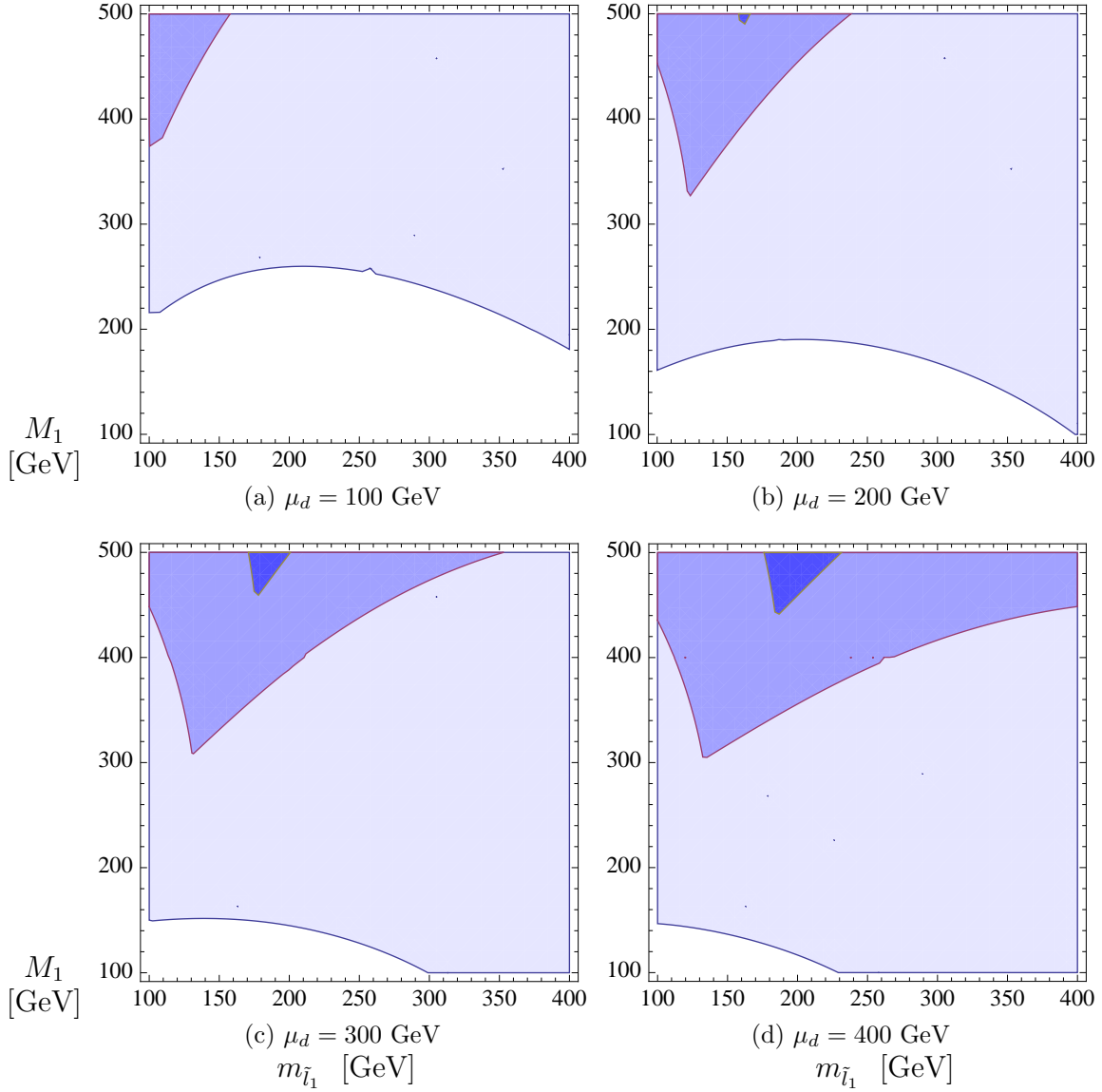
FIGURE 3.16: Same as Fig. 3.15 but for left handed sleptons. Similar to the right handed case, the constraint from $\mu \to 3e$ is also less severe than the other two processes in the parameter space shown.

CHAPTER IV

QUIRKONIUM DECAYS

This chapter includes unpublished material co-authored with Graham Kribs. Graham Kribs initiated this project; Ricky Fok performed all the calculation and produced the tables and plots that appear in this chapter.

Quirks are fermions transforming under the SM gauge group along with a new strongly-coupled "infracolor" group $SU(N)_{ic}$ [15]. (Related ideas were also considered in Ref. [13].) The infracolor confinement scale, Λ_{ic}, is assumed to be much smaller than the masses of all quirks. Since the infracolor-string breaking rate is proportional to $\exp(-m_q^2/\Lambda_{ic}^2)$, the infracolor string does not break. Quirk pairs remain in a bound state even when they are produced with high kinetic energies. This leads to several interesting collider physics and dark matter applications [15, 16, 111–120]. (Models with quirks can be considered to be hidden valley models, with the quirks being the barrier and the quirky glueballs being the light states. Other work on hidden valley models can be found in [121–123].) Certain kinds of quirks have already been searched for at the Tevatron by the D0 collaboration [124].

In this chapter, we consider quirks that acquire their mass through electroweak symmetry breaking. This is unlike the original proposal [15], and was motivated in part by the suggestion that asymmetric dark matter could arise as baryons made up of chiral quirks [16]. We do not, however, restrict ourselves to the specific theory or detailed parameter choices of [16]. Moreover, unlike Ref. [16], we are interested in the *mesons* of this theory, specifically, their decay branching ratios. While our results are general for $SU(N)_{ic}$, we illustrate our results numerically for the specific choice

$N = 2$, which is motivated both by Ref. [16] as well as minimizing the additional contributions to the electroweak precision observables. Nevertheless, our analytic results are applicable to mesons in the S and P states for arbitrary N.

At this point we should emphasize that only some aspects of quirky physics can be calculated (or simulated) with standard collider tools. In general, quirks can be produced in a standard collider physics process (for us, weak production), but then the p_T of the quirks must be shed before the quirks settle down into a low-angular-momentum state. This "spin-down" (or "wanga-wanga" [125]) process is in general non-perturbative, with the resulting radiation dependent on the relative strengths of infracolor and other couplings of the quirks. After spin-down, the quirks annihilate, causing quirky mesons to decay. It is solely this last step that is our interest in this paper.

The annihilation rate of quirky mesons is proportional to the lowest non-vanishing radial derivative of the meson wavefunction at zero relative quirk displacement. This is entirely analogous to positronium and quarkonium [126]. For an S state, this is $|\psi(0)|^2$, while for a P state, $|\psi'(0)|^2$. At high orbital angular momentum L, this wavefunction factor is suppressed. Ref. [15] estimated the suppression factor in the annihilation probability scaling as $(\beta/L)^{L+1}/L$, where β is the quirk relative velocity and $L > 0$. Therefore, instead of annihilating immediately, the mesons will emit soft radiation to shed its angular momentum. The radiation may be in the form of soft photons [113] that could be detected as rings in the $\eta - \phi$ plane in colliders. Such signals provide a smoking gun for discovery of quirks. Quirky glueballs can also be radiatively emitted, but they will most likely escape the detector before decaying. As the quirky bound state reaches a low angular momentum state ($L \sim 1$), it will ultimately annihilate, and in many cases, producing

observable signals. Some annihilation branching ratios for certain vector-like quirks were discussed before in [112].

This chapter is organized as follows. We will describe our quirk model in Sec. 4.1. We present the formalism to calculate the decay amplitudes in Sec. 4.2. Then, we present and discuss our results for two-body quirky meson decay in Secs. 4.4. and 4.5. Much of our results for neutral quirkonia can be obtained from earlier results on heavy quarkonia [126], which we have compared extensively, and thus we relegate the analytic results in our formalism and notation to Appendix B. We conclude with a discussion of the comparison between chiral quirkonium decays and vector-like quirkonium decays in Sec. 4.6.

4.1. Model and Setup

The model we consider is $SU(N)_{ic}$ with two flavors in the representations given in Table 4.1. This is the generalization of the model of Ref. [16] to N infracolors. We assume $\Lambda_{ic} \ll m_q$, and neglect the infracolor confinement contribution to the quirky meson masses. The Lagrangian that gives mass to the quirks is simply

$$\mathcal{L} \;\; = \;\; \lambda_U Q H u^c + \lambda_d Q H^\dagger d^c \;. \tag{4.1}$$

Despite the abuse of notation (Q, u^c, d^c), we emphasize that our quirks are color *singlets*. After electroweak symmetry breaking, the quirks acquire masses $M_{U,D} \equiv \lambda_{U,D} v$. Writing the electroweak doublet as $Q = (u, d)$, we can write the quirks in

	$SU(N)_{ic}$	$SU(2)_L$	$U(1)_Y$
Q	**N**	**2**	0
u^c	$\bar{\mathbf{N}}$	**1**	$-1/2$
d^c	$\bar{\mathbf{N}}$	**1**	$+1/2$

TABLE 4.1: Quirk quantum numbers.

terms of four-component Dirac spinors U, D

$$U = \begin{pmatrix} u \\ u^{c\dagger} \end{pmatrix} \qquad D = \begin{pmatrix} d \\ d^{c\dagger} \end{pmatrix} \tag{4.2}$$

where U, D have electric charge $q = \pm 1/2$. The quirky mesons formed from these objects include

$$(U\bar{U}), (D\bar{D}) \qquad \text{neutral mesons} \tag{4.3}$$

$$(U\bar{D}), (D\bar{U}) \qquad q = \pm 1 \text{ charged mesons .} \tag{4.4}$$

There are two interesting regions of parameter space satisfying the requirement $M_{U,D} \gg \Lambda_{ic}$. One occurs when $M_U \gg M_D$ or $M_D \gg M_U$, such that there is one set of heavy neutral mesons, one set of intermediate-mass electrically charged mesons, and one of set of light mesons. In this regime, the heavier mesons generically weak decay to the lightest mesons (microscopically the heavier quirks are weak decaying into the lighter quirks) *before* the quirks themselves have time to annihilate. In this regime, the relevant annihilation channels consist solely of the lightest neutral mesons.

The second regime, and the main focus of this paper, is when $M_U \simeq M_D$. When the two flavors of quirks are very nearly degenerate in mass, all of the mesons given in (4.3) and (4.4) are stable against weak decay. All of the quirk–anti-quirk pairs

within the mesons therefore annihilate faster than the kinematically-suppressed 3-body weak decay occurs. This leads to four distinct "towers" of mesons: two sets of neutral mesons and two sets of (oppositely) charged mesons.

The neutral mesons $(U\bar{U})$ and $(D\bar{D})$ can mix with each other through infragluon box diagrams that are superficially similar to the W-box diagrams within the SM that lead to mixing among the neutral mesons of QCD. However, unlike QCD, all of the quirks are heavy, while the gauge bosons being exchanged in the box diagram are massless. This small mixing is an interesting effect for further study. Our meson decay rates are invariant under $U \leftrightarrow D$, and we simply compute $(Q\bar{Q})$ as if it were an exact $(U\bar{U})$ or $(D\bar{D})$ eigenstate. In practice, there may be either a small admixture between these states, in which case the mixing angle cancels out in our width calculations, or otherwise for maximal mixing, we treat $(Q\bar{Q})$ as the $[(U\bar{U}) + (D\bar{D})]/\sqrt{2}$ eigenstate.

The infracolor confining potential in the Coulombic approximation is [16]

$$V(r) = -\frac{\bar{\alpha}_{ic}}{r} , \tag{4.5}$$

where $\bar{\alpha}_{ic} \equiv C_2(\mathbf{N})\alpha_{ic} = (N^2 - 1)/(2N)\alpha_{ic}$. Analogous to a hydrogen atom, the Schrödinger wave function can be solved analytically. The decay widths we calculate are proportional to the meson wavefunction when the two constituent quirks overlap. The wavefunction factors that appear in the decay widths, for S and P states respectively, are

$$|R_S(0)|^2 = 4\left(\frac{1}{4}\bar{\alpha}_{ic}M\right)^3 \tag{4.6}$$

$$|R'_P(0)|^2 = \frac{1}{24}\left(\frac{1}{4}\bar{\alpha}_{ic}M\right)^5 , \tag{4.7}$$

where M is the mass of the meson.

4.2. Matrix Elements of Bound State Decays

This section reviews the procedures to evaluate the decay amplitudes of different angular momentum bound states following the method in [127]. We work in the non-relativistic limit, where the relative momentum of the constituents, $\mathbf{q} \ll M$, where M is the mass of the bound state. We also ignore the contribution to the meson mass from the binding potential, i.e. $M = 2m_Q$, with m_Q being the mass of the individual quirks.

Calculations of the matrix element involving an incoming bound state and an outgoing free state, $\langle X|iT|B \rangle$, are needed to evaluate different bound state decay rates. This is most conveniently done by writing the bound state as a superposition of free fermion states with spins (s_1, s_2) and momenta (p_1, p_2):

$$
\begin{aligned}
|B\rangle = |^{2s+1}l_j\rangle &= \sum_{MS_z} \langle lmss_z|jj_z\rangle |lmss_z\rangle \\
&= \sqrt{\frac{2}{M}} \int \frac{d^3\mathbf{q}}{(2\pi)^3} \psi^{lm}(\mathbf{q}) \left[\sum_{ms_z} \langle lmss_z|jj_z\rangle \right] \times \\
&\quad \left[\sum_{s_1 s_2} \langle s_1, \frac{1}{2}, s_2, \frac{1}{2}|ss_z\rangle \right] |s_1 p_1 s_2 p_2\rangle,
\end{aligned}
\tag{4.8}
$$

where ψ is the Schroedinger wavefunction of the bound state. In its rest frame, $p_1 = Q/2 + q$, and $p_2 = Q/2 - q$, where Q is the 4-momentum of the meson, and q is the relative 4-momentum of quirks. Then, the quantity $\langle X|iT|s_1 p_1 s_2 p_2\rangle = i\bar{v}_{s_2}(p_2) \mathcal{M} u_{s_1}(p_1)$ is the usual fermion-antifermion annihilation matrix element into

83

the outgoing state f. The amplitude A of a bound state decaying into final state X is defined in the same way as the matrix element

$$\langle X|iT|B\rangle = iA(B)(2\pi)^4\delta^4(p_X - p_B).\tag{4.9}$$

Expanding the above to the lowest non-vanishing order in $\mathbf{q}$, we found the following decay amplitudes for S and P states,

$$A(^1S_0) = \sqrt{\frac{N}{16\pi M}}R_S(0)\,Tr[\mathcal{M}\gamma^5(-\mathcal{Q} + M)],\tag{4.10}$$

$$A(^3S_1) = \sqrt{\frac{N}{16\pi M}}R_S(0)\,Tr[\mathcal{M}\not{\epsilon}(-\mathcal{Q} + M)],\tag{4.11}$$

$$A(^1P_1) = -i\sqrt{\frac{3N}{4\pi M}}R'_P(0)\,Tr[\frac{1}{2}\epsilon_\mu\mathcal{M}^\mu\gamma^5(-\mathcal{Q} + M) + \mathcal{M}\not{\epsilon}\frac{\mathcal{Q}}{M}\gamma^5],\tag{4.12}$$

$$A(^3P_0) = i\sqrt{\frac{N}{4\pi M}}R'_P(0)\,Tr[\frac{1}{2}\mathcal{M}^\alpha\left(\frac{Q_\alpha\mathcal{Q}}{M^2} - \gamma_\alpha\right)(-\mathcal{Q} + M) - 3\mathcal{M}],\tag{4.13}$$

$$A(^3P_1) = i\sqrt{\frac{3N}{8\pi M}}R'_P(0)Tr[2\mathcal{M}\not{\epsilon}\gamma^5 - \frac{i}{2M}\epsilon^{\rho\alpha\beta\delta}Q_\rho\mathcal{M}_\alpha\gamma_\beta\epsilon_\delta(-\mathcal{Q} + M)],\quad\text{and}\tag{4.14}$$

$$A(^3P_2) = -i\sqrt{\frac{3N}{4\pi M}}R'_P(0)Tr[\frac{1}{2}\mathcal{M}_\alpha\epsilon^{\alpha\beta}\gamma_\beta(-\mathcal{Q} + M)],\tag{4.15}$$

where $R(0)$ and $R'(0)$ are the radial wavefunction of the meson and its derivative at the origin, respectively. The quantity $\mathcal{M}_\alpha = \partial\mathcal{M}/\partial q^\alpha$ is the derivative of the matrix element with respect to the relative momentum q. The meson polarizations in the rest frame, ϵ^μ for spin-1, and $\epsilon^{\mu\nu}$ for spin-2, are chosen to be

$$
\begin{aligned}
\epsilon_{\mp}^{\mu} &= \left(0, \mp\frac{1}{\sqrt{2}}, -\frac{i}{\sqrt{2}}, 0\right), \\
\epsilon_L^{\mu} &= (0, 0, 0, 1), \\
\epsilon_{J_z}^{\alpha\beta} &= \sum_{M, S_z} \langle 1M, 1S_z | 2J_z \rangle,
\end{aligned}
\tag{4.16}
$$

with $J_z \in \{-2, -1, 0, 1, 2\}$. A factor of $\sqrt{2}$ comes from the fact that the meson is in its quirky color singlet state. The P and C parities of the above angular momentum states are manifest in each of the decay amplitudes above. For example, with $Q^{\mu} = (M, 0, 0, 0)$ in the rest frame, the P and C parities of the bilinear constructed from the projector appearing in $A(^1S_0)$, $\bar{\psi}\gamma^5(-\slashed{Q} + M)\gamma^0\psi$, are $-$ and $+$, respectively. Thus $J^{PC} = 0^{-+}$ for $^1S_0$, as expected. One can check that the other amplitudes give the expected J^{PC} using the same procedure. From equations 4.10 to 4.15, we rederived all of the two body decay rates listed in [126][1].

4.3. Radiative Transitions

In a quirky meson, the binding potential is dominated by the contributions from the quirky strong interaction. The Lyman alpha transition rate for neutral quirkonia has been estimated by [16]

$$
\Gamma_{L\alpha} = \frac{4}{9}q^2\alpha_{em}E_{L\alpha}^3|\langle 0|r|1\rangle|^2 = \frac{1}{4}\left(\frac{8}{81}\right)^2\alpha_{em}\bar{\alpha}_{ic}^4M,
\tag{4.17}
$$

---

[1]We found a relative sign difference between the two terms in the amplitude $A(^3P_1)$. We attribute this to our definition of $\epsilon^{0123} = 1$.

where M is the meson mass. Charged quirkonia have the same rate, due to the fact that the electromagnetic correction to the potential is of order α_{em}/α_{ic} and is negligible. The wavefunctions of the quirkonia, therefore, remains unchanged, and so does the transition rate.

4.3.1. $g'g'$

As the mesons are color singlets, only t and u channels contribute to the decay amplitudes of $B \to g'g'$. Then the decay rate should be proportional to that of $B \to \gamma\gamma$. A simple calculation shows that, for an $SU(N)$ color gauge group,

$$\Gamma(B \to g'g') = \frac{N^2 - 1}{4N^2}\Gamma(B \to \gamma\gamma)\bigg|_{\alpha e_Q \to \alpha_s,} \tag{4.18}$$

where e_Q is the quirk electric charge. Setting $N = 3$ reproduces the results in [126]. The $^3S_1$ state cannot decays into $g'g'$. Its decay into $g'g'g'$ for any N is listed in [112],

$$\Gamma(^3S_1 \to g'g'g') = \frac{(N^2 - 1)(N^2 - 4)}{N^2}\frac{\alpha_{ic}^3}{9\pi M^2}(\pi^2 - 9)|R_S(0)|^2. \tag{4.19}$$

This vanishes for $SU(2)$, as three gluons cannot form a color singlet state in this case.

4.4. Quirkonium Decays

Apart from a color factor of N, decay rates of neutral quirkonia that do not involve any gluons are the same as listed in [126]. The decay rates of charged quirkonia will be discussed in this section.

Charged quirkonia are expected to have larger partial widths than their neutral counterparts. This is because charged particles do not have a well-defined charge conjugate parity, hence loosening the constraints posed by CP conservation. Here, we list the partial widths of charged quirky mesons with positive unit electric charge, i.e. $Q_U - Q_D = 1$, where Q is the electric charge of either the up-type or down-type quirks. The mass ratio squared R_i and the relative velocity $\beta_{i,f}$ appearing in the formulas below are defined as

$$
\begin{aligned}
R_i &= \frac{m_i^2}{M^2}, \qquad \text{and} & (4.20) \\
\beta_{i,j} &= \sqrt{1 + (R_i - R_j)^2 + 2(R_i + R_j)}, & (4.21)
\end{aligned}
$$

respectively.

4.4.1. $W^+\gamma$

The charged quirkonium decay widths into $W^+\gamma$ is qualitatively different to the widths of neutral quirkonia into $Z\gamma$. There are two reasons for the differences; the decay into $W^+\gamma$ can go through an s-channel with a W exchange. The corresponding diagram is absent for $Z\gamma$; the photon does not couple to a electrically neutral Z. Another reason is that the photon couples to quirks of different electric charges in the t and u channel diagrams, due to the emission of a charged W. It is illuminating to write the chiral projection operators as $P_{L,R} = (v_W \mp a_W \gamma^5)/2$, with $a_W = v_W = 1$, so that the vector and axial-vector contributions from the W current are manifest.

The partial widths into $W^+\gamma$ are

$$\Gamma(^1S_0^+ \to W^+\gamma) = \frac{N\alpha\alpha_W v_W^2}{4M^2}(Q_U + Q_D)^2(1 - R_W)|R_S(0)|^2,$$

(4.22)

$$\Gamma(^3S_1^+ \to W^+\gamma) = \frac{N\alpha\alpha_W a_W^2}{12m_W^2}(Q_U + Q_D)^2(1 - R_W^2)|R_S(0)|^2,$$

(4.23)

$$\Gamma(^1P_1^+ \to W^+\gamma) = \frac{N\alpha\alpha_W}{M^2m_W^2}[a_W^2(Q_U + Q_D)^2(1 - R_W^2)$$
$$+v_W^2(Q_U - Q_D)^2 R_W(1 - R_W)]|R_P'(0)|^2,$$

(4.24)

$$\Gamma(^3P_0^+ \to W^+\gamma) = \frac{N\alpha\alpha_W(1 - R_W)}{M^4}\left[a_W^2(Q_U - Q_D)^2\right.$$
$$\left.+v_W^2(Q_U + Q_D)^2\left(1 + \frac{2}{1 - R_W}\right)^2\right]|R_P'(0)|^2,$$

(4.25)

$$\Gamma(^3P_1^+ \to W^+\gamma) = \frac{N\alpha\alpha_W}{2M^2m_W^2}\left[a_W^2(1 - R_W)\right.$$
$$\left.+4v_W^2(Q_U + Q_D)^2 R_W^2\frac{1 + R_W}{1 - R_W}\right]|R_P'(0)|^2,$$

(4.26)

$$\Gamma(^3P_2^+ \to W^+\gamma) = \frac{N\alpha\alpha_W(1 - R_W)}{10M^2m_W^2}\left[a_W^2(Q_U - Q_D)^2(3 + 4R_W)\right.$$
$$\left.+\frac{4v_W^2(Q_U + Q_D)^2 R_W(6 + 3R_W + R_W^2)}{(1 - R_W)^2}\right]|R_P'(0)|^2.$$

(4.27)

Interestingly, all but one term in $\Gamma(^3P_1^+ \to W^+\gamma)$ are proportional to either the hypercharge $Y = (Q_U + Q_D)/2$ or the isospin $T_{3U} = (Q_U - Q_D)/2$ of the quirks.

4.4.2. W^+H

In the limit degenerate quirk masses, their coupling constants to the Higgs boson are the same. As a consequence, the decay matrix elements has the same form as that for the decay into ZH, and can be obtained by the replacements $g_Z \to g/\sqrt{2}$ and vector and axial vector couplings by $1/2$; $a, v \to 1/2$. This gives a conversion factor of $1/(2\sqrt{2})$ converting the ZH matrix elements to WH:

$$\mathcal{M}_{W^+H} = \frac{1}{2\sqrt{2}}\mathcal{M}_{ZH}. \tag{4.28}$$

Therefore, the partial widths into W^+H, have exactly the same form as those for ZH, aside from a factor of $1/8$. The analysis for ZH in [126] applies to W^+H as well. The partial widths are

$$\Gamma(^1S_0^+ \to W^+H) = \frac{N\alpha_W^2\beta_{WH}^3}{32M^2}\frac{1}{R_W^2}|R_S(0)|^2, \tag{4.29}$$

$$\begin{aligned}
\Gamma(^3S_1^+ \to W^+H) =\ &\frac{N\alpha_W^2\beta_{WH}}{384}\frac{M^2}{m_W^4}\frac{1}{(1-R_W)^2(1-R_H-R_W)^2} \\
&\times\bigg(8R_W[(1-R_W)^2 + R_H(1-3R_W)]^2 \\
&+[R_H^2(1-3R_W) - \\
&2R_H(1-R_W(2+R_W))(1-R_W)(1-R_W^2-\beta_{WH}^2)]^2\bigg)|R_S(0)|^2,
\end{aligned} \tag{4.30}$$

$$\Gamma(^1P_1^+ \to W^+H) = \frac{N\alpha_W^2\beta_{WH}^3}{4M^2m_W^2(1 - R_H - R_W)^2}|R_P'(0)|^2, \tag{4.31}$$

$$\Gamma(^3P_0^+ \to W^+H) = 0, \tag{4.32}$$

$$\Gamma(^3P_1^+ \to W^+H) = \frac{N\alpha_W^2\beta_{WH}}{8m_W^4}\left(\frac{2[1 - R_H + R_W]^2[1 + R_W(2 - R_H + R_W)]^2}{(1 - R_H - R_W)^2(1 - R_W)^2}\right.$$
$$\left. + R_W\left[\frac{4R_W}{1 - R_W} + \frac{\beta_{WH}^2 - 4(1 - R_H - R_W)}{(1 - R_H - R_W)^2}\right]^2\right)|R_P'(0)|^2, \tag{4.33}$$

$$\Gamma(^3P_2^+ \to W^+H) = \frac{3N\alpha_W^2\beta_{WH}^5}{40M^2m_W^2(1 - R_H - R_W)^4}|R_P'(0)|^2. \tag{4.34}$$

4.4.3. WZ

Notice that double longitudinal modes are allowed from the decay of a charged quirkonium in the $^1S_0$ state. This is impossible for the neutral quirkonium case, where it decays into ZZ or WW. To see this, the $^1S_0$ state has $J^{PC} = 0^{-+}$, but at zero angular momentum, the double longitudinal state has $J^{PC} = 0^{++}$. The decay into double longitudinal modes for neutral quirkonia in $^1S_0$ is forbidden by CP conservation. For charged states, the charge parity is irrelevant, and the decay into double longitudinal mode is allowed by CP conservation. Naively, one would expect that the $^1S_0$ decay rate is longitudinal from appearance of the $1/(R_ZR_W)$ term. However, this decay width vanishes at large quirkonium mass M because the diagram with an s-channel Goldstone Boson cancels the other diagrams in this regime.

$$\Gamma(^1S_0^+ \to W^+Z) = \frac{N\alpha_W\alpha_Z\beta_{WZ}}{32M^2}\left(1 - \frac{c_W^2 R_Z}{R_W}\frac{1}{1 + R_W - R_Z}\right)^2$$
$$\times \left(\frac{8}{(1 - R_W - R_Z)^2} + \frac{1}{R_W R_Z}\right)|R_S(0)|^2,$$

$$(4.35)$$

$$\Gamma(^3S_1^+ \to W^+Z) = \frac{N\alpha_W\alpha_Z\beta_{WZ}^3}{64M^2}\frac{1}{(1 - R_W)^2(1 - R_W - R_Z)^2}\Big\{8c_W^4 R_Z^2$$
$$+2(1 - R_W - 2c_W^2 R_Z)^2\left(\frac{1}{R_W} + \frac{1}{R_Z}\right)$$
$$+\frac{1}{R_W R_Z}(1 - R_W - c_W^2 R_Z(1 + R_W + R_Z))^2\Big\}|R_S(0)|^2,$$

$$(4.36)$$

$$\Gamma(^1P_1^+ \to W^+Z) = \frac{N\alpha_W\alpha_Z\beta_{WZ}}{4M^4(1 - R_W - R_Z)^2}\Big\{\frac{(1 + R_W - R_Z)^2}{R_W} + \frac{(1 - R_W + R_Z)^2}{R_Z}$$
$$+4\left(1 - \frac{c_W^2\beta_{WZ}^2}{1 - R_W - R_Z}\right)^2\Big\}|R_P'(0)|^2,$$

$$(4.37)$$

$$\Gamma(^3P_0^+ \to W^+Z) = \frac{N\alpha_W\alpha_Z\beta_{WZ}^3}{M^4(1 - R_W - R_Z)^4}[1 - c_W^2(1 - R_W + R_Z)]^2|R_P'(0)|^2,$$

$$(4.38)$$

$$\Gamma(^3P_1^+ \to W^+Z) = \frac{N\alpha_W\alpha_Z\beta_{WZ}^3}{16M^4(1 - R_W - R_Z)^2}\Big\{\frac{32c_W^4 R_Z^2}{(1 - R_W)^2}$$
$$+\frac{2}{R_Z}\left[1 + \frac{2R_Z}{1 - R_W - R_Z} - \frac{8c_W^2 R_Z\big(1 - \frac{R_Z}{2(1 - R_W)}\big)}{1 - R_W - R_Z}\right]^2$$
$$+\frac{2}{R_W}\left[2c_W^4 R_Z\left(1 + \frac{2R_W + R_Z}{1 - R_W}\right)^2\right.$$
$$+\left.\left(1 + \frac{2R_W}{1 - R_W - R_Z} - 2c_W^2(1 - \frac{2R_Z}{1 - R_W})\right)^2\right]$$
$$\Big\}|R_P'(0)|^2$$

$$(4.39)$$

91

$$\Gamma(^3P_2^+ \to W^+Z) = \frac{N\alpha_W\alpha_Z\beta_{WZ}^3}{40M^4(1 - R_W - R_Z)^4}\left\{16[1 - c_W^2(1 - R_W + R_Z)]^2\right.$$
$$+\frac{3}{R_Z}[1 - R_W + R_Z - 4c_W^2 R_Z]^2$$
$$\left.+\frac{3}{R_W}[1 + R_W - R_Z - 2c_W^2(1 - R_W - R_Z)]^2\right\}|R_P'(0)|^2.$$

(4.40)

4.4.4. $f_u\bar{f}_d$

Decays into two fermions only proceed via the W^+ s-channel exchange. The non-zero widths with outgoing fermion masses $m_{1,2}$ are

$$\Gamma(^1S_0^+ \to u\bar{d}) = \frac{N\alpha_W^2\beta_{ud}}{16M^2}\frac{(R_1 - R_1^2 + R_2 + 2R_1R_2 - R_2^2)}{R_W^2}|R_S(0)|^2,$$

(4.41)

$$\Gamma(^3S_1^+ \to u\bar{d}) = \frac{N\alpha_W^2\beta_{ud}}{48M^2}\frac{2 - R_1 - R_1^2 - R_2 + 2R_1R_2 - R_2^2}{(1 - R_W)^2}|R_S(0)|^2,$$

(4.42)

$$\Gamma(^3P_1^+ \to u\bar{d}) = \frac{N\alpha_W^2\beta_{ud}}{2M^4}\frac{2 - R_1 - R_1^2 - R_2 + 2R_1R_2 - R_2^2}{(1 - R_W)^2}|R_P'(0)|^2,$$

(4.43)

where $\beta_{ud} = \sqrt{1 + (R_u - R_d)^2 + 2(R_u + R_d)}$, and $R_{u,d} = m_{u,d}^2/M^2$. As expected, the $^1S_0$ partial width is proportional to m_f^2/M^2, corresponding to a chirality flip on the outgoing fermion line.

4.5. Branching Ratios and Width Ratios

4.5.1. Charged Quirkonia

The branching ratios of charged quirkonia are presented in this section. Given a final state f, the branching ratio for f, $BR(Q\bar{Q} \to f)$, is

$$BR(Q\bar{Q} \to f) = \frac{\Gamma(Q\bar{Q} \to f)}{\sum_f \Gamma(Q\bar{Q} \to f)}, \tag{4.44}$$

where the sum is over all final states. We presents our results numerically choosing $\alpha_{ic} = 0.2$ and $N = 2$.

The charged quirkonium case is particularly simple. As the system is electrically charged, it cannot decay into $g'g'$. We ignore the binding energy of the system. Therefore, the branching ratios are independent of α'_s. The only unknowns are the masses of the Higgs boson and the quirkonium. Fig. 4.1 shows the decay branching ratios of charged quirkonium states. For all states, only the WH branching ratio is sensitive to different values of the Higgs mass. The plots shown for charged quirkonia here are also applicable to any massive bound states that only decay via the electroweak $SU(2) \times U(1)$ group, with electric charges $Q_u = -Q_d = 1/2$. Note that we only show the summed width over the massless fermions (2 quark pairs, 3 lepton-neutrino pairs), as the widths of all massless fermions are the same (see Sec. 4.4.4.). Also, we only show the decays for the $U\bar{D}$ meson. We have checked that the widths for $\bar{U}D$ decay are the same.

The branching ratios of different bound states are plotted in Fig. 4.1. For the S states, the WZ partial width dominates. For P states, radiative transition usually dominates. For $^3P_1$, the WH width becomes larger than the L_α transition width

when the meson mass is larger than $\gtrsim 600$ GeV, provided that the meson is heavier than the threshold.

4.5.2. Neutral Quirkonia

The results for neutral quirkonia is more complicated than their charged counterparts. Not only are there more decay channels, but also, in some cases, the mesons can decay into two quirky glueballs, $G'G'$. Due to the non-perturbative nature of the glueball channel, we do not attempt to calculate its decay width. Instead we present our results in terms of the width ratio

$$WR(Q\bar{Q} \to f) = \frac{\Gamma(Q\bar{Q} \to f)}{\sum_{f \neq G'G'} \Gamma(Q\bar{Q} \to f)}, \tag{4.45}$$

Also, for reasons of clarity, we do not present the plots for the branching ratios when the Higgs mass deviates from 125 GeV. Unless the final states involve Higgs bosons, a larger Higgs boson mass would only push the corresponding thresholds towards higher meson masses, leaving the other branching ratios mostly unchanged as in the case of charged quirkonia. However, there is a qualitative change in the branching ratios for the $^3P_0$ state when the Higgs mass is sufficiently large, which will be discussed below.

4.5.2.1. $^1S_0$ and $^3S_1$

The branching ratios of the S states are shown in Figs. 4.2a-4.2b. Decay into quirky-glueballs can dominate the branching ratio. The next dominant contributions are the double transverse WW and ZZ channels.
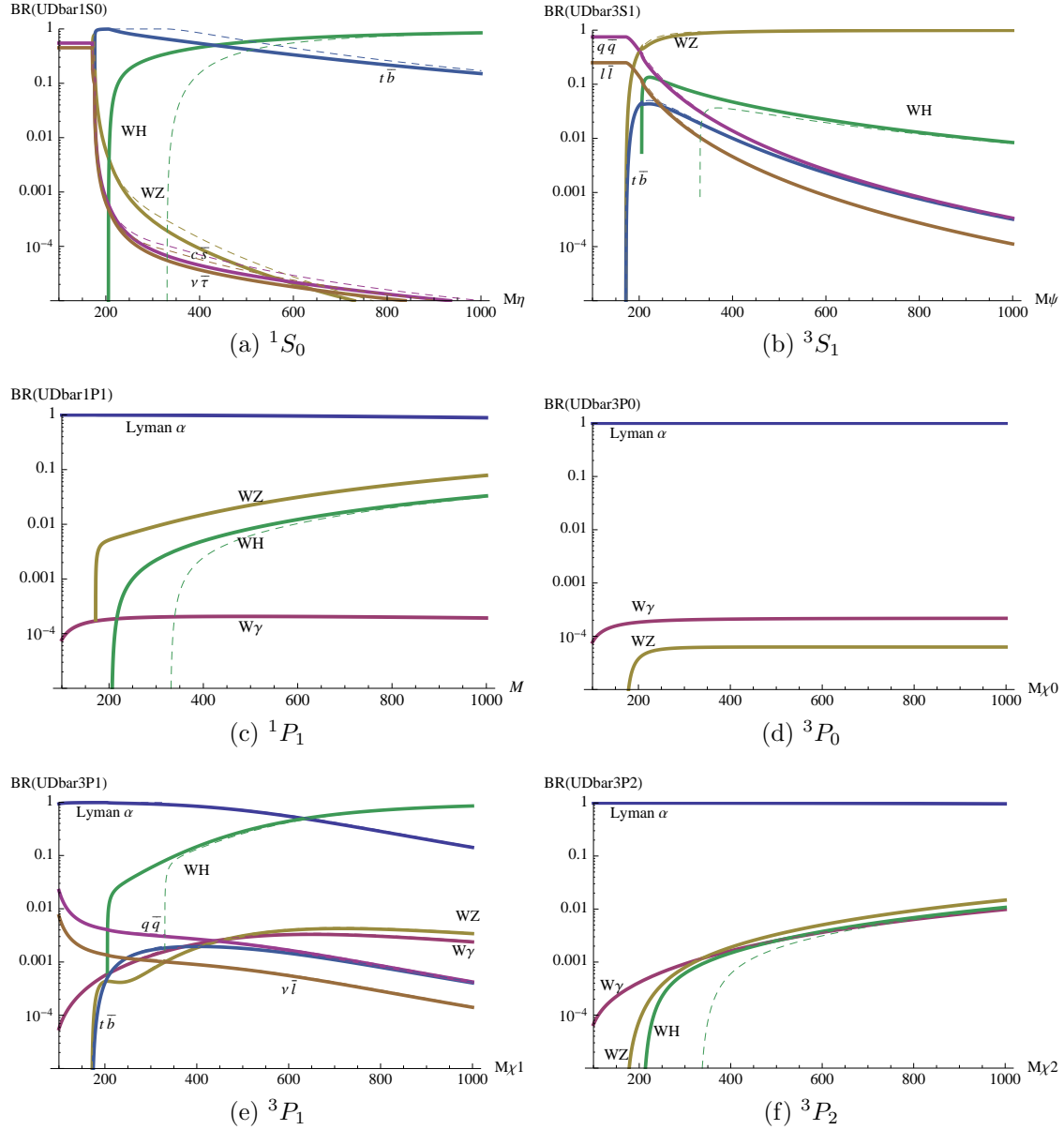
FIGURE 4.1: Decay branching ratio of quirkonia in different J^{PC} states. Solid lines are with Higgs mass $M_H = 125$ GeV, dashed lines with $M_H = 250$ GeV.

The results for the $^3S_1$ state can be discussed more precisely because the 2-glueball channel is absent (see Sec. 4.3.1.). For moderate values of M, the double longitudinal WW mode dominates. Because of Bose symmetry, the two Z's cannot be longitudinal simultaneously and the ZZ mode is suppressed.

4.5.3. $^1P_1$

The width ratios are shown in Fig. 4.2e is dominated by the L_α transition throughout the sub-TeV range. All other widths contain a single enhancement factor, from either the longitudinal mode or the quirky Yukawa.

4.5.4. $^3P_0$

The $^3P_0$ state can decay into two quirky-glueballs. The branching ratios exhibit an interesting feature when the Higgs mass is larger than $2m_W, 2m_Z$ and $2M_t$, where M_t is the top mass. The decay channels WW, ZZ, and $t\bar{t}$ involves an s-channel Higgs boson exchange. When the meson mass is near the Higgs mass $M \sim M_H$, the widths are enhanced by the s-channel Higgs resonance. This can be seen in Fig. 4.2d. There, the WW and ZZ widths has a resonance at $M = M_H = 250$ GeV when the s-channel Higgs boson is on-shell. The $t\bar{t}$ width does not exhibit this behavior because at 250 GeV, the decay into two top quarks from a single Higgs boson is forbidden by kinematics.

4.5.5. $^3P_1$

The branching ratios for the $^3P_1$ state are shown in Fig. 4.2f. The ZH channel are doubly enhanced and is dominant for $M \gtrsim 700$ GeV.
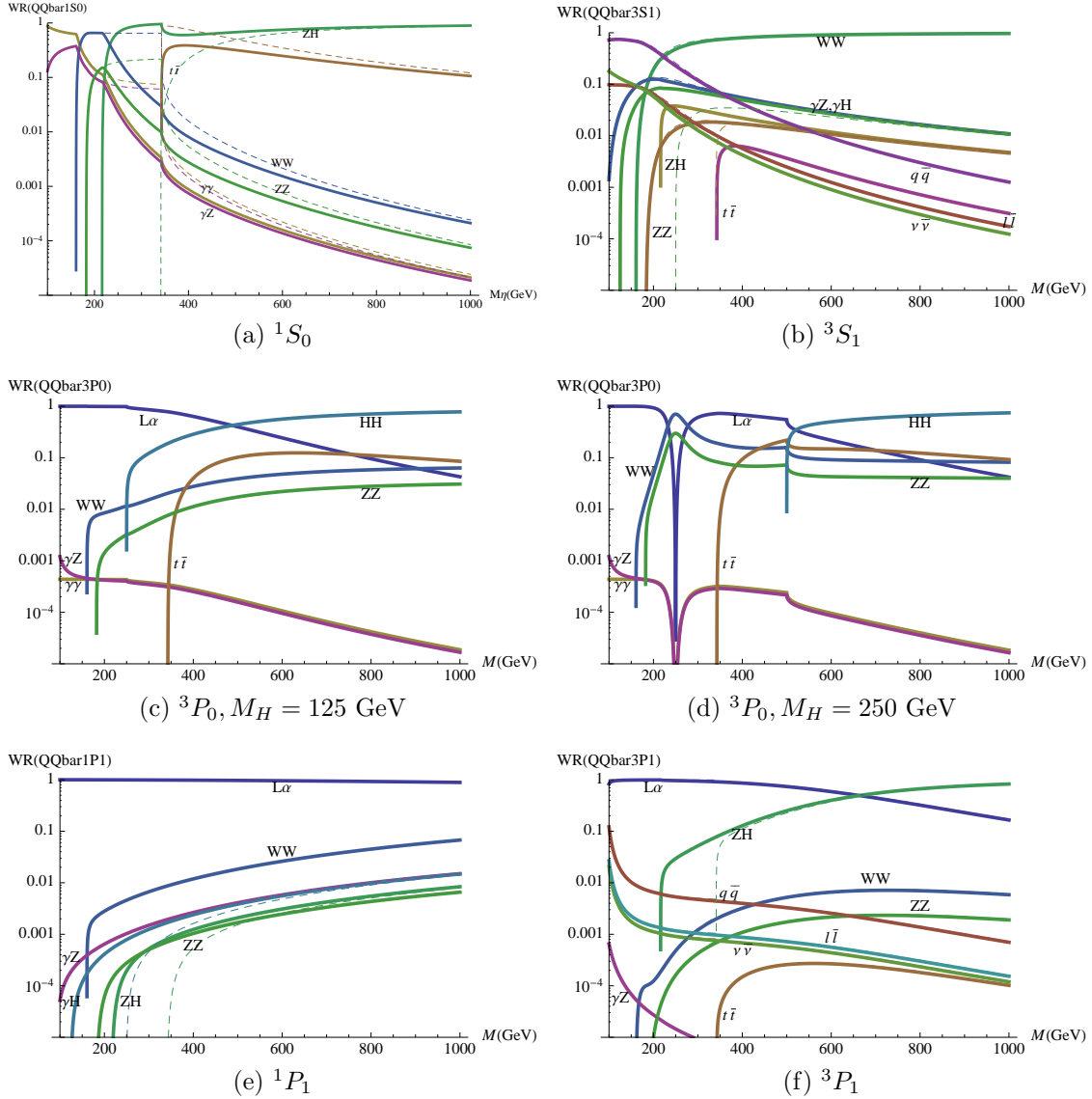
FIGURE 4.2: Decay width ratios of quirkonia in different J^{PC} states. For Figs. (a),(b),(e),(f),(g), solid lines correspond to a Higgs mass $M_H = 125$ GeV, while dashed lines correspond to $M_H = 250$ GeV. In many instances, there is no difference between the width ratios for different Higgs masses, and thus the solid lines overlap the invisible dashed lines. For Figs. (c),(d), we have presented the choices $M_H = 125$ GeV and $M_H = 250$ GeV separately due to the s-channel pole structure visible in Fig. (d).

97
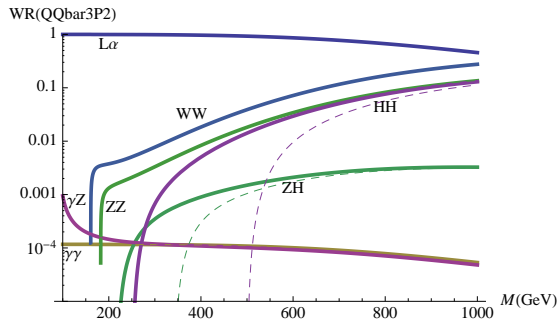
FIGURE 4.3: Same as figure 4.2 but for $^3P_2$.

4.5.6. $^3P_2$

Same as the $^3P_0$ state, the glueball channel and the radiative transition width dominates the branching ratios. As these two are of the same magnitude, the branching ratios are not drastically affected by the magnitude of the two glueball width. The presence of the glueball width can only reduce the other widths by at most a factor of ~ 2. The channels WW, ZZ and HH are doubly enhanced and will take over the radiative transition at high meson mass ($\gtrsim 1$ TeV).

4.6. Discussion and Comparison to Vector-Like Quirkonia

Annihilation rates for the case of vector-like quirks in certain other representations has been calculated in [112, 120]. There is not a general rule that relates the decay rates of vector-like quirks to chiral quirks. But in certain circumstances one can be obtained from the other, and vice versa. In this section, we will discuss differences and similarities of vector-like and chiral quirk decay rates, and give examples in cases where the decay rates are related.

We wish to compare our results for chiral quirks to a related theory with vector-like quirks. The vector-like theory we consider consists of the doublet Q given before

98
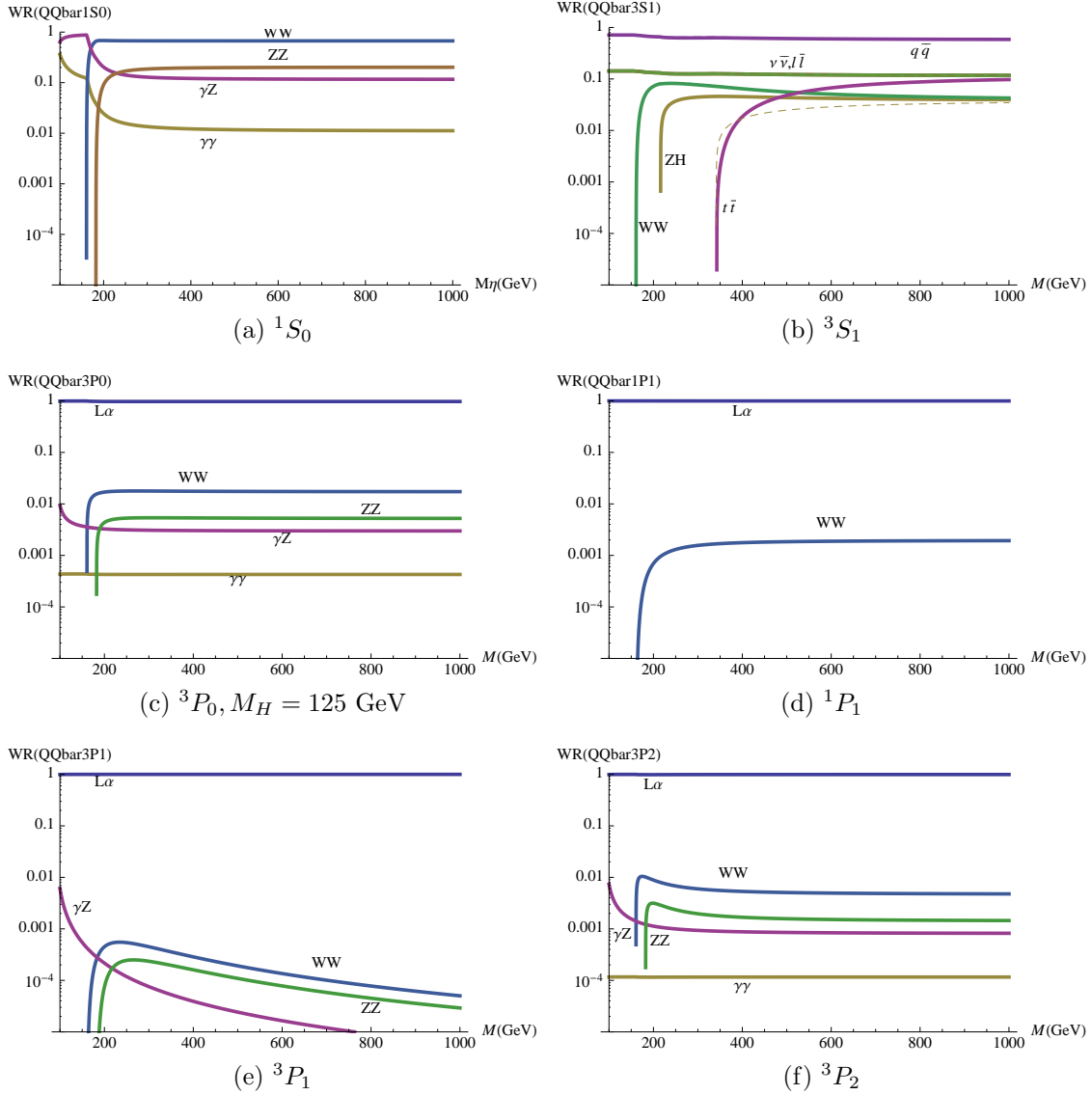
FIGURE 4.4: Decay width ratios of quirkonia with vector-like masses in different J^{PC} states. Solid lines correspond to a Higgs mass $M_H = 125$ GeV, while dashed lines correspond to $M_H = 250$ GeV. In many instances, there is no difference between the width ratios for different Higgs masses, and thus the solid lines overlap the invisible dashed lines.

99
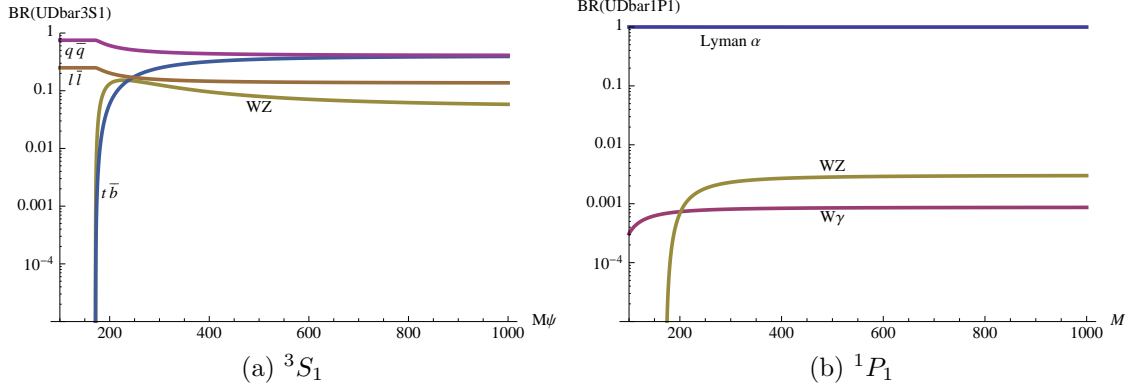
FIGURE 4.5: Same as 4.4 but for charged quirkonia. Only the two J^{PC} states shown here have nontrivial branching ratios. The state $^3S_1$ cannot decay through two-body decays. The $^3P_{0,1,3}$ states can only decay radiatively into S states.

in Table 4.1, but now replacing

$$\begin{bmatrix} u^c(\bar{\mathbf{N}}, \mathbf{1}, -1/2) \\ d^c(\bar{\mathbf{N}}, \mathbf{1}, +1/2) \end{bmatrix} \longrightarrow Q'(\bar{\mathbf{N}}, \mathbf{2}, 0) . \tag{4.46}$$

Yukawa couplings, (4.1), are not present, while we can now write the vector-like mass MQQ' where $M = M_U = M_D$. There are several differences that lead to qualitatively different decay widths.

First, the coupling of electroweak gauge bosons to left- and right-handed quirks are the same – the quirk-W/Z coupling is a purely vector interaction, and processes that proceed through the axial vector coupling in the chiral case are absent for vector-like quirks. As an example, consider the decay rate $\Gamma(^3S_1 \to f\bar{f})$, for neutral and charged quirkonia. The only diagrams are the s-channel γ/Z or W. In the neutral case, the only difference that separates vector-like and chiral is the different axial-vector and vector coupling of the Z. Therefore, the expressions for vector-like [112] and chiral [126] quirk are the same. For the charged case, the axial-vector and

vector couplings are not explicitly written in [112], but their rate is 4 times larger than in the chiral case in [126]. This is because the s-channel W couples to both left and right handed quirks in the vector-like case, whereas in the chiral case they only couple to left handed quirks. Therefore, the decay rate into a fermion-antifermion pair for a charged $^3S_1$ is four times larger than its chiral counterpart.

Second, the quirks do not couple to the Higgs and the corresponding Goldstone bosons (through the longitudinally polarized electroweak gauge bosons). Virtual Goldstone bosons can only appear in the s-channel, and since the Goldstone bosons are pseudoscalars, they only contribute to the $^1S_0$ decay rates. Vector-like quirks, by contrast, do not have couplings to the Higgs or the Goldstone bosons. In addition, Goldstone bosons can appear in the final state (appearing as longitidually polarized electroweak gauge bosons). This leads to qualitatively different decay rates into gauge bosons for all of the bound states.

For completeness, we present the width and branching ratios of vector-like quirkonia in Fig. 4.4 for neutral quirkonia and Fig. 4.5 for charged quirkonia. There are striking differences between the chiral and vector-like cases. The most prominent feature in the vector-like case is that all decay widths have the same asymptotic behavior at large quirkonium mass - there are no longitudinal enhancements of W/Z anywhere. This is expected, as the longitudinal W/Z asymptotes to the respective Goldstone bosons, which do not couple to the vector-like quirks in u- and t-channel quirk-exchange diagrams. Also, the trilinear gauge boson coupling appearing in s-channel gauge boson exchange arises from the electroweak gauge structure of $SU(2)_L$ and has no relation to the electroweak breaking mechanism. Therefore, one would not expect any enhancements in the decay widths of vector-like quirkonia. Without longitudinal enhancements, the Lyman-α transition dominates over all P-

state decays for all quirkonium masses. Whereas in the chiral case, decay channels that receives longitudinal enhancements can dominate the Lyman-α transition at large quirkonium masses. The most interesting decay channel is $^3P_0$ decay into two Higgs bosons, which begins to become the dominant decay channel for quirkonium masses $\gtrsim 500$ GeV. If chiral quirks are colored, quirkonia at low masses are expected to decay via QCD couplings, i.e. into quarks and gluons. However, neither of these can be longitudinally enhanced. Therefore, at sufficiently high quirkonium masses, the $^3P_1$ state would predominantly decay into a di-Higgs boson final state. This is a striking signal at the LHC!

In the low quirkonium mass regime, the overall behavior of both vector-like and chiral quirkonia are similar: P-states predominantly decay via the Lyman-α transition and $^3S_1$ into $q\bar{q}$. It is interesting to note that for $^1S_0$, γZ dominates the vector-like quirkonium decay, whereas $\gamma\gamma$ is dominant for chiral quirkonia. This is because the primordial electroweak gauge boson W_3^μ couples not just to the left-handed vector-like quirk, but to the right handed one also! A rough estimate indicates that this gives a factor of four increase in the γZ rate for the vector-like case. Indeed, the isospin contribution to the vector coupling of the Z to the quirks for the vector-like case is twice as much as that for chiral quirks.

CHAPTER V

CONCLUSION

In chapter II, we have calculated the strength of the electroweak phase transition in a supersymmetric model with four chiral generations. We find there is an intriguing region of parameter space, with fourth generation quarks heavier than about 300 GeV and the squark to quark mass ratio $1 \lesssim m_{\tilde{q}'}/m_{q'} \lesssim 1.1$, where $\phi_c/T_c > 1$. Within this region of parameter space we showed the Higgs can be easily heavier than the LEP bound of about 115 GeV, and the strength of the phase transition can easily exceed $\phi_c/T_c = 1$.

This suggests that a viable model of electroweak baryogenesis could indeed be a low energy supersymmetric model with a fourth generation of chiral fermions. What we have shown is the the strength of the first order phase transition can be large enough to prevent the washout of a baryon asymmetry. This model also has several new sources of CP violation, ubiquitous in low energy supersymmetry, that could be used to satisfy Sakharov's CP violation criteria. Examples of sufficient CP violation that have been employed in other supersymmetric electroweak baryogenesis scenarios [21–23] include the phase of the Higgsino mass parameter μ as well as the gaugino mass parameters $M_{1,2}$.

It is *coincidental* that the region of parameter space where the first order transition is strong enough combined with obtaining a large enough Higgs mass (taking $\tan \beta = 1$) happens to be just beyond the current Tevatron direct search bounds [40, 41]. If we are lucky, the Tevatron could begin to see evidence for new physics in the form of both an extra chiral generation as well as superpartners in the

very near future. The LHC, however, can easily cover this parameter space. Indeed, the mechanism to enhance the first order phase transition described here is expected to be found or ruled out with only modest amount of data from the LHC.

In chapter III, We have calculated the constraints on $\mu \leftrightarrow e$ mixing in the MRSSM from the flavor violating processes $\mu \to e\gamma$, $\mu \to e$ conversion, and $\mu \to 3e$. Given the simplifications stated in Sec. 3.1., we explored LFV in the MRSSM as a function of the parameters $M_1, \mu_d, m_{\tilde{l}}$, and $\sin 2\theta_{\tilde{l}}$ within the sub-TeV range. Given the heavier slepton mass set to be $m_{\tilde{l}_2} = 1.5 m_{\tilde{l}_2}$, we found that the bound from $\mu \to 3e$ is always less severe than the bounds derived from either $\mu \to e\gamma$ or $\mu \to e$ conversion.

For right-handed slepton mixing, $\mu \to e$ conversion in gold nuclei provides the most severe constraint – it completely rules out maximal mixing (compare Fig. 3.15 with Fig. 3.2). The situation is qualitatively different for left-handed mixing – the most severe bound in this case comes from $\mu \to e\gamma$, as dominant amplitudes (charge radius and magnetic dipole) of $\mu \to e$ conversion interfere destructively and opens up a large region in parameter space that satisfies the experimental bounds. From Fig. 3.3 for $\mu \to e\gamma$, one sees that maximal mixing is allowed in regions where the bino mass is ~ 500 GeV at $\mu_d = 200$ GeV, with a moderate splitting between sleptons. The results suggest that the most likely observation of large slepton flavor violation signals at the LHC will occur in the left-handed sector.

It is interesting to consider how the bounds on slepton flavor mixing angles will change as the constraints on LFV are strengthened. This is most easily understood by recognizing that all of our bounds are proportional to $\sin^2 2\theta_{\tilde{l}}$. In other words, the boundary of the allowed regions are contours of constant $BR_{\text{bound}}/\sin^2 2\theta_{\tilde{l}}$, where BR_{bound} is the bound on the branching ratio of a process. In plotting the allowed

regions of parameter space in the previous sections of the paper, we used of course the current experimental bound. Suppose that in some future experiment the bounds are improved, say by a factor of 100. Then, the boundary of the region that satisfy this new bound for $\sin^2 2\theta_{\tilde{l}} = 0.1$ is the same as the boundary for the current bound with $\sin^2 2\theta_{\tilde{l}} = 1$.

In chapter IV, we showed that there are striking differences between the chiral and vector-like cases. The most prominent feature in the vector-like case is that all decay widths have the same asymptotic behavior at large quirkonium mass - there are no longitudinal enhancements of W/Z anywhere. This is expected, as the longitudinal W/Z asymptotes to the respective Goldstone bosons, which do not couple to the vector-like quirks in u- and t-channel quirk-exchange diagrams. Also, the trilinear gauge boson coupling appearing in s-channel gauge boson exchange arises from the electroweak gauge structure of $SU(2)_L$ and has no relations to the electroweak breaking mechanism. Therefore, one would not expect any enhancements in the decay widths of vector-like quirkonia. Without longitudinal enhancements, the Lyman-α transition dominate over all P-state decays for all quirkonium masses. Whereas in the chiral case, decay channels that receives longitudinal enhancements can dominate the Lyman-α transition at large quirkonium masses. The most interesting decay channel is $^3P_0$ decay into two Higgses, which begins to become the dominant decay channel for quirkonium masses $\gtrsim$ 500 GeV. If chiral quirks are colored, quirkonia at low masses are expected to decay via QCD couplings, i.e. into quarks and gluons. However, neither of these can be longitudinally enhanced. Therefore, at sufficiently high quirkonium masses, the $^3P_1$ state would predominantly decay into di-Higgses. In other words, we could observe di-Higgs signal from strongly produced quirkonia at the LHC!

In the low quirkonium mass regime, the overall behavior of both vector-like and chiral quirkonia are similar - P-states predominantly decay via the Lyman-α transition and $^3S_1$ into $q\bar{q}$. It is interesting to note that for $^1S_0$, γZ dominates the vector-like quirkonium decay, whereas $\gamma\gamma$ is dominant for chiral quirkonia. This is because the primordial electroweak gauge boson W_3^{μ} couples not just to the left-handed vector-like quirk, but to the right handed one also. A rough estimate indicates that this gives a factor of four increase in the γZ rate for the vector-like case. Indeed, the isospin contribution to the vector coupling of the Z to the quirks for the vector-like case is twice as much as that for chiral quirks.

APPENDIX A

GAUGINO AND SLEPTON STRUCTURE

To discuss the neutralino masses and interactions more quantitatively, we define the ψ_B and $\psi_{\tilde{H}_d}$ to the be fermion R-partners of $\tilde{B}$ and $\tilde{H}_d^0$, respectively. Then we form the Dirac bino and Higgsino spinors and their charge conjugates,

$$ N_{\tilde{B}} = \begin{pmatrix} \psi_B \\ \tilde{B}^\dagger \end{pmatrix}, \quad N_{\tilde{H}_d} = \begin{pmatrix} \tilde{H}_d^0 \\ \psi_{\tilde{H}_d}^\dagger \end{pmatrix}, \quad N_{\tilde{B}}^c = \begin{pmatrix} \tilde{B} \\ \psi_B^\dagger \end{pmatrix}, \quad N_{\tilde{H}_d}^c = \begin{pmatrix} \psi_{\tilde{H}_d} \\ \tilde{H}_d^{0\dagger} \end{pmatrix}. \tag{A.1} $$

We can also see that the Dirac spinor N has an R-charge -1, whereas N^c has an R-charge $+1$. The gaugino mass matrix, M_N, is shown in the mass term below

$$ (\bar{N}_B, \bar{N}_{\tilde{H}_d}) \begin{pmatrix} M_1 & -\cos\beta\sin\theta_W M_Z \\ 0 & \mu_d \end{pmatrix} \begin{pmatrix} P_L N_B \\ P_L N_{\tilde{H}_d} \end{pmatrix} + h.c. \tag{A.2} $$

The mass matrix is diagonalized by a bi-orthogonal transformation; the diagonalized neutralino mass matrix, $M_N^D = O_L^T M_N O_R$, obey $(M_N^D)^2 = O_L M_N (M_N)^T (O_L)^T = O_R (M_N)^T M_N (O_R)^T$, where $O_{(L,R)}$ are the orthogonal matrices that diagonalize the mass matrix. In this definition, the $\tilde{B}$ and $\tilde{H}_d^0$ content of the i-th neutralino N_i are, O_{Li1} and O_{Ri2}, respectively.

We consider mixing between selectrons and smuons only, parameterized as follows:

$$ \begin{pmatrix} \tilde{l}_1 \\ \tilde{l}_2 \end{pmatrix}_{L,R} = \begin{pmatrix} \cos\theta_{\tilde{l}} & \sin\theta_{\tilde{l}} \\ -\sin\theta_{\tilde{l}} & \cos\theta_{\tilde{l}} \end{pmatrix}_{L,R} \begin{pmatrix} \tilde{e} \\ \tilde{\mu} \end{pmatrix}_{L,R}, \tag{A.3} $$

where $\tilde{l}_i$ represents the sleptons in the mass-eigenstate basis.

Then slepton flavor violation comes from the interaction terms between a sfermion, $\tilde{f}_i$, a neutralino, N_i, and a fermion f_i:

$$-\tilde{f}_{L\alpha}^* \bar{N}_i (U_{L\alpha\beta}^\dagger [O_{Li1} G_L f_{L\beta} + O_{Ri2} y_f f_{R\beta}]) - \tilde{f}_{R\alpha}^* \bar{N}_i^c (U_{R\alpha\beta}^\dagger [O_{Li1} G_R f_{R\beta} + O_{Ri2} y_f f_{L\beta}]) + h.c. \tag{A.4}$$

where $U_{L,R}$ are the slepton mixing matrices in Eq. (A.3). The coupling constants are

$$G_{L,R} = \sqrt{2} g' Y_{f_{(L,R)}}, \quad \text{and} \tag{A.5}$$

$$y_f = \frac{g' m_f}{\sqrt{2} M_Z \sin \theta_w \cos \beta}. \tag{A.6}$$

The subscript i on the (s)fermion denotes its generation, subscripts L and R denote the chirality, with α and β being the flavor indices. The hypercharge of a fermion f is denoted by Y_f. From the above interaction terms we see that $\tilde{f}_R$ and $\tilde{f}_L$ have different R-charges; -1 and $+1$, respectively.

The Z-boson only couples to Higgsinos. The ZNN interaction term is

$$\frac{g}{2 \cos \theta_w} Z_\mu [\bar{N}_i \gamma^\mu (O_{Ri2} O_{Rj2} P_L + O_{Li2} O_{Lj2} P_R) N_j]. \tag{A.7}$$

One can also write the ZNN coupling in terms of N^c,

$$-\frac{g}{2 \cos \theta_w} Z_\mu [\bar{N}^c_i \gamma^\mu (O_{Li2} O_{Lj2} P_L + O_{Ri2} O_{Rj2} P_R) N_j^c]. \tag{A.8}$$

Examining the neutralino mixing matrix in Eq. (A.2), the lightest gaugino receives a negative shift, $-\Delta < 0$, and so the lightest neutralino has mass $M_{N_1} = \mu_d - \Delta < m_{C_1}$, and thus the lightest gaugino is a neutralino.

APPENDIX B

DECAY RATES OF NEUTRAL QUIRKONIA

This appendix summarizes the decay rates of neutral quirkonia. The decay rates differ with [126] by just a factor of 2/3 due to a different color group. We also attempt to rewrite the decay rates so that the origins of the terms in the expression are manifest. In the expressions below, a t-channel quirk exchange with outgoing particles i and j corresponds to the factor $(1 - R_i - R_j)^{-1}$, with $R_i = m_i^2/M^2$, and M is the quirkonium mass. An s-channel diagram exchanging particle ϕ corresponds to $(1 - R_\phi)^{-1}$. The relative velocity between i and j is $\beta_{ij} = \sqrt{1 + (R_i - R_j)^2 - 2(R_i + R_j)}$.

B.1. $f\bar{f}$

The decays into a fermion-antifermion pair, only the s-channel γ, Z and Higgs diagram contribute. The decay of the $^1S_0$ state requires a chirality flip on the outgoing fermion line, resulting in the dependence on the fermion mass squared, M_f^2, in its decay rate - similar to pseudoscalar decay.

$$\Gamma(^1S_0 \to f\bar{f}) = 8N\alpha_Z^2 a_f^2 a_Q^2 \beta_f \frac{m_f^2}{m_Z^4} |R_S(0)|^2, \tag{B.1}$$

$$\Gamma(^3S_1 \to f\bar{f}) = \frac{4N\alpha_{EM}^2 \beta_f}{3M^2} \left\{ (1 + 2R_f) \left(e_Q e_f + \frac{v_f v_Q}{c_W^2 s_W^2 (1 - R_Z)} \right)^2 \right.$$
$$\left. + \frac{a_f^2 v_Q^2 \beta_f^2}{c_W^4 s_W^4 (1 - R_Z)^2} \right\} |R_S(0)|^2, \tag{B.2}$$

$$\Gamma(^1P_1 \to f\bar{f}) = 0, \tag{B.3}$$

$$\Gamma(^3P_0 \to f\bar{f}) = \frac{9N\alpha_Z^2 \beta_f^3}{8M^2 (1 - R_H)^2} \frac{m_f^2}{m_Z^4} |R_P'(0)|^2, \tag{B.4}$$

$$\Gamma(^3P_1 \to f\bar{f}) = \frac{32N\alpha_Z^2 a_Q^2 \beta_f}{M^4 (1 - R_Z)^2} [a_f^2 \beta_f^2 + (1 + 2R_f) v_f^2] |R_P'(0)|^2, \tag{B.5}$$

$$\Gamma(^3P_2 \to f\bar{f}) = 0, \tag{B.6}$$

where M is the quirkonium mass, $\alpha_Z = \alpha_{EM}/(c_W^2 s_W^2)$, c_W and s_W are the cosine and sine of the Weinberg angle, respectively, $a_i = T_{3i}/2$ and $v_i = a_i - e_i s_W^2$ are the axial-vector and vector couplings of the Z to fermion i, with $i = \{Q, f\}$ for the quirk and the outgoing fermion, respectively, $R_j = m_j^2/M^2$, and $\beta_f = \sqrt{1 - 4R_f}$ is the relative velocity between the two outgoing fermions.

B.2. $Z\gamma$

Only the t-channel diagram contributes decays into $Z\gamma$,

$$\Gamma(^1S_0 \to Z\gamma) \;=\; \frac{8N\alpha_{EM}\alpha_Z e_Q^2 v_Q^2}{M^2}(1 - R_Z)|R_S(0)|^2, \tag{B.7}$$

$$\Gamma(^3S_1 \to Z\gamma) \;=\; \frac{8N\alpha_{EM}\alpha_Z e_Q^2 a_Q^2}{3m_Z^2}(1 - R_Z^2)|R_S(0)|^2, \tag{B.8}$$

$$\Gamma(^1P_1 \to Z\gamma) \;=\; \frac{32N\alpha_{EM}\alpha_Z e_Q^2 a_Q^2}{M^2 m_Z^2}(1 - R_Z^2)|R'_P(0)|^2, \tag{B.9}$$

$$\Gamma(^3P_0 \to Z\gamma) \;=\; \frac{32N\alpha_{EM}\alpha_Z e_Q^2 v_Q^2}{M^4(1 - R_Z)}(3 - R_Z)^2|R'_P(0)|^2, \tag{B.10}$$

$$\Gamma(^3P_1 \to Z\gamma) \;=\; \frac{64N\alpha_{EM}\alpha_Z e_Q^2 v_Q^2}{M^2 m_Z^2(1 - R_Z)}(1 + R_Z)R_Z^2|R'_P(0)|^2, \tag{B.11}$$

$$\Gamma(^3P_2 \to Z\gamma) \;=\; \frac{64N\alpha_{EM}\alpha_Z e_Q^2 v_Q^2}{5M^2 m_Z^2(1 - R_Z)}(R_Z^2 + 3R_Z + 6)|R'_P(0)|^2, \tag{B.12}$$

where the definitions of various quantities can be found in the paragraph below (B.6).

B.3. W^+W^-

$$\Gamma(^1S_0 \to W^+W^-) = \frac{N\alpha_W^2\beta_W^3}{8M^2(1-2R_W)^2}|R_S(0)|^2, \tag{B.13}$$

$$\Gamma(^3S_1 \to W^+W^-) = \frac{NM^2\alpha_W^2\beta_W^3}{48m_W^4}\left\{\frac{R_W(2-R_W)}{(1-2R_W)^2}\right.$$
$$-\frac{4R_W(5+6R_W)}{1-2R_W}\left(e_Qs_W^2 + \frac{v_Q}{1-R_Z}\right)$$
$$\left.+4(1+20R_W+12R_W^2)\left(e_Qs_W^2 + \frac{v_Q}{1-R_Z}\right)^2\right\}|R_S(0)|^2, \tag{B.14}$$

$$\Gamma(^1P_1 \to W^+W^-) = \frac{3N\alpha_W^2\beta_W}{8M^2m_W^2(1-2R_W)^2}\left\{1+\beta_W^2\right.$$
$$\left.+2R_W\left(1+\frac{\beta_W^2}{1-2R_W}\right)^2\right\}|R_P'(0)|^2, \tag{B.15}$$

$$\Gamma(^3P_0 \to W^+W^-) = \frac{N\alpha_W^2\beta_W}{4M_W^4}\left\{\left[\frac{\pm 1}{1-2R_W}\left(1-3R_W+\frac{\beta_W^2R_W}{1-2R_W}\right)\right.\right.$$
$$\left.-\frac{3}{1-R_H}(\frac{1}{2}-R_W)\right]^2$$
$$\left.+2R_W^2\left[\frac{\pm 1}{1-2R_W}\left(1-\frac{\beta_W^2}{1-2R_W}\right)-\frac{3}{1-R_H}\right]^2\right\}|R_P'(0)|^2, \tag{B.16}$$

$$\Gamma(^3P_1 \to W^+W^-) = \frac{N\alpha_W^2\beta_W^3}{32m_W^2}\left\{[32R_W^2+(3-\beta_W^2)]^2\left(\frac{1}{1-2R_W}-\frac{1}{1-R_Z}\right)^2\right.$$
$$\left.+4R_W\left[\left(\frac{3-4R_W}{(1-2R_W)^2}-\frac{4}{1-R_Z}\right)^2+\frac{\beta_W^4}{(1-2R_W)^4}\right]\right\}|R_P'(0)|^2, \tag{B.17}$$

$$\Gamma(^3P_2 \to W^+W^-) = \frac{N\alpha_W^2\beta_W}{40m_W^2(1-2R_W)^2}\left\{\left(1-\frac{2R_W\beta_W^2}{1-2R_W}\right)^2\right.$$

$$+6R_W\left[1-\frac{2R_W\beta_W^4}{(1-2R_W)^2}+\left(1-\frac{\beta_W^2}{1-2R_W}\right)^2\right]$$

$$\left.+8R_W^2\left[6+\left(1-\frac{\beta_W^2}{1-2R_W}\right)^2\right]\right\}|R_P'(0)|^2,$$

$$(B.18)$$

where $\alpha_W = \alpha_{EM}/s_W^2$, $\beta_W = \sqrt{1-4R_W}$ is the relative velocity of the two W's, e_Q, v_Q, and a_Q are the electric charge, vector and axial-vector couplings to the Z of the quirk, respectively, and $R_W = m_W^2/M^2$. In B.16, the $\pm$ corresponds to $D\bar{D}$ for $+$, and $U\bar{U}$ for $-$.

B.4. *ZZ*

$$\Gamma(^1S_0 \to ZZ) = \frac{4N(a_Q^2 + v_Q^2)\alpha_Z^2\beta_Z^3}{M^2(1 - 2R_Z)^2}|R_S(0)|^2, \tag{B.19}$$

$$\Gamma(^3S_1 \to ZZ) = \frac{8Na_Q^2 v_Q^2 \alpha_Z^2 \beta_Z^5}{3m_Z^2(1 - 2R_Z)^2}|R_S(0)|^2, \tag{B.20}$$

$$\Gamma(^1P_1 \to ZZ) = \frac{32Na_Q^2 v_Q^2 \alpha_Z^2 \beta_Z^3}{M^2 m_Z^2 (1 - 2R_Z)^2}|R_P'(0)|^2, \tag{B.21}$$

$$\Gamma(^3P_0 \to ZZ) = \frac{N\alpha_Z^2\beta_Z}{8m_Z^4}\left\{\left(32a_Q^2 - \frac{3 - 6R_Z}{1 - R_H} - \frac{64R_Z^2 v_Q^2}{(1 - 2R_Z)^2}\right)^2\right.$$
$$+ 8R_Z^2\left(\frac{3}{1 - R_H} - \frac{32R_Z v_Q^2}{(1 - 2R_Z)^2}\right.$$
$$\left.\left. - \frac{8(3 - 4R_Z)(a_Q^2 - v_Q^2)}{(1 - 2R_Z)^2}\right)^2\right\}|R_P'(0)|^2, \tag{B.22}$$

$$\Gamma(^3P_1 \to ZZ) = \frac{16N\alpha_Z^2\beta_Z^5}{M^2 m_Z^2 (1 - 2R_Z)^2}\left(\frac{2R_Z v_Q^2}{1 - 2R_Z} - a_Q^2\right)^2|R_P'(0)|^2, \tag{B.23}$$

$$\Gamma(^3P_2 \to ZZ) = \frac{16N\alpha_Z^2\beta_Z}{5m_Z^4}\left\{\left(a_Q^2 + v_Q^2\frac{4R_Z^2}{(1 - 2R_Z)^2}\right)^2 + \frac{3R_Z}{(1 - 2R_Z)^2}\left(a_Q^2 + v_Q^2\frac{2R_Z}{1 - 2R_Z}\right)^2\right.$$
$$\left. + (v_Q^2 + a_Q^2)^2\frac{4R_Z^2}{(1 - 2R_Z)^2}\left(3 + \frac{2R_Z^2}{(1 - 2R_Z)^2}\right)\right\}|R_P'(0)|^2, \tag{B.24}$$

where $\beta_Z = \sqrt{1 - 4R_Z}$ is the relative velocity between the Z's. The definitions of other quantities can be found below equation B.6.

B.5. ZH

$$\Gamma(^1S_0 \to ZH) = \frac{N\alpha_Z^2 a_Q^2 M^2 \beta_{ZH}^3}{4m_Z^4}|R_S(0)|^2, \tag{B.25}$$

$$\Gamma(^3S_1 \to ZH) = \frac{N\alpha_Z^2 v_Q^2 \beta_{ZH}}{6m_Z^2}\Bigg\{\left(\frac{1-R_H+R_Z}{1-R_H-R_Z}\right.$$
$$\left.-\frac{2R_Z}{1-R_Z}\right)^2 + \frac{R_Z}{2}\left(\frac{1-R_H+R_Z}{1-R_Z}-\frac{2}{1-R_H-R_Z}\right)^2\Bigg\}|R_S(0)|^2, \tag{B.26}$$

$$\Gamma(^1P_1 \to ZH) = \frac{2Nv_Q^2\alpha_Z^2\beta_{ZH}^3}{M^2m_Z^2(1-R_H-R_Z)^2}|R'_P(0)|^2, \tag{B.27}$$

$$\Gamma(^3P_0 \to ZH) = 0, \tag{B.28}$$

$$\Gamma(^3P_1 \to ZH) = \frac{2Na_Q^2\alpha_Z^2\beta_{ZH}}{m_Z^4}\Bigg\{(1-R_H+R_Z)^2\left(\frac{R_Z}{1-R_Z}-\frac{1}{1-R_H-R_Z}\right)^2$$
$$+8R_Z\left(\frac{R_Z}{1-R_Z}-\frac{1}{1-R_H-R_Z}-\frac{\beta_{ZH}^2}{4(1-R_H-R_Z)^2}\right)^2\Bigg\}|R'_P(0)|^2, \tag{B.29}$$

$$\Gamma(^3P_2 \to ZH) = \frac{3Na_Q^2\alpha_Z^2\beta_{ZH}^5}{5M^2m_Z^2(1-R_H-R_Z)^4}|R'_P(0)|^2, \tag{B.30}$$

B.6. γH

$$\Gamma(^3S_1 \to \gamma H) = \frac{Ne_Q^2\alpha_{EM}\alpha_Z(1-R_H)}{6m_Z^2}|R_S(0)|^2, \tag{B.31}$$

$$\Gamma(^1P_1 \to \gamma H) = \frac{2NeQ^2\alpha_{EM}\alpha_Z(1-R_H)}{M^2m_Z^2}|R'_P(0)|^2. \tag{B.32}$$

B.7. HH

$$\Gamma(^3P_0 \to HH) \;=\; \frac{N\alpha_Z^2\beta_H}{32m_Z^4}\left(\frac{9R_H}{1-R_H} - \frac{6}{1-2R_H} + \frac{\beta_H^2}{(1-2R_H)^2}\right)^2|R_P'(0)|^2,$$

$$\text{(B.33)}$$

$$\Gamma(^3P_2 \to HH) \;=\; \frac{N\alpha_Z^2\beta_H^5}{80m_Z^4(1-2R_H)^4}|R_P'(0)|^2. \tag{B.34}$$

REFERENCES CITED

[1] G. 't Hooft, NATO Adv. Study Inst. Ser. B Phys. **59**, 135 (1980).

[2] M. Quiros, arXiv:hep-ph/9901312.

[3] A. D. Sakharov, Pisma Zh. Eksp. Teor. Fiz. **5** (1967) 32 [JETP Lett. **5** (1967 SOPUA,34,392-393.1991 UFNAA,161,61-64.1991) 24].

[4] A. G. Cohen, D. B. Kaplan and A. E. Nelson, Ann. Rev. Nucl. Part. Sci. **43**, 27 (1993) [arXiv:hep-ph/9302210].

[5] J. I. Kapusta and C. Gale, "Finite-temperature field theory: Principles and applications," *Cambridge, UK: Univ. Pr. (2006) 428 p*

[6] R. Kubo, J. Phys. Soc. Jap. **12**, 570 (1957).

[7] P. C. Martin and J. S. Schwinger, Phys. Rev. **115**, 1342 (1959).

[8] T. Matsubara, Prog. Theor. Phys. **14**, 351 (1955).

[9] S. R. Coleman and E. J. Weinberg, Phys. Rev. D **7**, 1888 (1973).

[10] N. Arkani-Hamed, Summer School on Particle Physics, Cosmology and Strings 2007, Perimeter Institute Recorded Seminar Archive.

[11] J. Wess and J. Bagger, "Supersymmetry and supergravity," *Princeton, USA: Univ. Pr. (1992) 259 p*

[12] S. Martin, A Supersymmetry Primer, arXiv:hep-ph/9709356 (1997).

[13] L. B. Okun, JETP Lett. **31**, 144 (1980) [Pisma Zh. Eksp. Teor. Fiz. **31**, 156 (1979)]; Nucl. Phys. B **173**, 1 (1980).

[14] R. Barate *et al.* [LEP Working Group for Higgs boson searches and ALEPH Collaboration and and], Phys. Lett. B **565**, 61 (2003) [arXiv:hep-ex/0306033].

[15] J. Kang and M. A. Luty, JHEP **0911**, 065 (2009) [arXiv:0805.4642 [hep-ph]].

[16] G. D. Kribs, T. S. Roy, J. Terning, K. M. Zurek, Phys. Rev. **D81**, 095001 (2010). [arXiv:0909.2034 [hep-ph]].

[17] C. Jarlskog, Phys. Rev. Lett. **55**, 1039 (1985).

[18] G. W. Anderson and L. J. Hall, Phys. Rev. D **45**, 2685 (1992).

[19] M. Dine, P. Huet and R. L. . Singleton, Nucl. Phys. B **375**, 625 (1992).

[20] P. Arnold and O. Espinosa, Phys. Rev. D **47**, 3546 (1993) [Erratum-ibid. D **50**, 6662 (1994)] [arXiv:hep-ph/9212235].

[21] G. F. Giudice, Phys. Rev. D **45**, 3177 (1992).

[22] J. R. Espinosa, M. Quiros and F. Zwirner, Phys. Lett. B **307**, 106 (1993) [arXiv:hep-ph/9303317]; A. Brignole, J. R. Espinosa, M. Quiros and F. Zwirner, Phys. Lett. B **324**, 181 (1994) [arXiv:hep-ph/9312296].

[23] M. S. Carena, M. Quiros and C. E. M. Wagner, Phys. Lett. B **380**, 81 (1996) [arXiv:hep-ph/9603420].

[24] D. E. Morrissey, "LHC Probes of (MSSM) Baryogenesis", talk given at Physics of the LHC, KITP.

[25] M. Pietroni, Nucl. Phys. B **402**, 27 (1993) [arXiv:hep-ph/9207227].

[26] J. Kang, P. Langacker, T. j. Li and T. Liu, Phys. Rev. Lett. **94**, 061801 (2005) [arXiv:hep-ph/0402086].

[27] A. Menon, D. E. Morrissey and C. E. M. Wagner, Phys. Rev. D **70**, 035005 (2004) [arXiv:hep-ph/0404184].

[28] S. W. Ham, S. K. OH, C. M. Kim, E. J. Yoo and D. Son, Phys. Rev. D **70**, 075001 (2004) [arXiv:hep-ph/0406062].

[29] M. S. Carena, A. Megevand, M. Quiros and C. E. M. Wagner, Nucl. Phys. B **716**, 319 (2005) [arXiv:hep-ph/0410352].

[30] K. Funakubo, S. Tao and F. Toyoda, Prog. Theor. Phys. **114**, 369 (2005) [arXiv:hep-ph/0501052].

[31] S. J. Huber, T. Konstandin, T. Prokopec and M. G. Schmidt, Nucl. Phys. B **757**, 172 (2006) [arXiv:hep-ph/0606298]; S. J. Huber, T. Konstandin, T. Prokopec and M. G. Schmidt, Nucl. Phys. A **785**, 206 (2007) [arXiv:hep-ph/0608017].

[32] J. Shu, T. M. P. Tait and C. E. M. Wagner, Phys. Rev. D **75**, 063510 (2007) [arXiv:hep-ph/0610375].

[33] S. Profumo, M. J. Ramsey-Musolf and G. Shaughnessy, JHEP **0708**, 010 (2007) [arXiv:0705.2425 [hep-ph]].

[34] C. Grojean, G. Servant and J. D. Wells, Phys. Rev. D **71**, 036001 (2005) [arXiv:hep-ph/0407019].

[35] W. M. Yao *et al.* [Particle Data Group], J. Phys. G **33**, 1 (2006).

[36] G. D. Kribs, T. Plehn, M. Spannowsky and T. M. P. Tait, Phys. Rev. D **76**, 075016 (2007) [arXiv:0706.3718 [hep-ph]].

[37] We thank M. Ibe for discussions on this point.

[38] J. Alcaraz *et al.* [ALEPH Collaboration and DELPHI Collaboration and L3 Collaboration and], arXiv:hep-ex/0612034.

[39] D. M. Pierce, J. A. Bagger, K. T. Matchev and R. j. Zhang, Nucl. Phys. B **491**, 3 (1997) [arXiv:hep-ph/9606211].

[40] T. Aaltonen *et al.* [CDF Collaboration], arXiv:0801.3877 [hep-ex].

[41] D0 collaboration, `http://www-d0.fnal.gov/Run2Physics/WWW/results/prelim/HIGGS/H21/H21F0_supplement.eps`

[42] M. S. Carena, H. E. Haber, S. Heinemeyer, W. Hollik, C. E. M. Wagner and G. Weiglein, Nucl. Phys. B **580**, 29 (2000) [arXiv:hep-ph/0001002].

[43] M. S. Carena, M. Quiros and C. E. M. Wagner, Nucl. Phys. B **524**, 3 (1998) [arXiv:hep-ph/9710401].

[44] M. Laine and K. Rummukainen, Nucl. Phys. Proc. Suppl. **73**, 180 (1999) [arXiv:hep-lat/9809045].

[45] We thank T. Roy for nudging us to consider counting differently.

[46] W. S. Hou, arXiv:0803.1234 [hep-ph].

[47] M. Ahmed *et al.* [MEGA Collaboration], Phys. Rev. D **65**, 112002 (2002) [arXiv:hep-ex/0111030].

[48] J. Adam *et al.* [MEG collaboration], arXiv:0908.2594 [hep-ex].

[49] W. H. Bertl *et al.* [SINDRUM II Collaboration], Eur. Phys. J. C **47**, 337 (2006).

[50] U. Bellgardt *et al.* [SINDRUM Collaboration], Nucl. Phys. B **299**, 1 (1988).

[51] R. K. Kutschke, AIP Conf. Proc. **1182**, 718 (2009).

[52] Project X and the Science of the Intensity Frontier, white paper, Fermilab, 2010. http://www.fnal.gov/pub/projectx/pdfs/ProjectXwhitepaperJan.v2.pdf

[53] J. Hisano, T. Moroi, K. Tobe and M. Yamaguchi, Phys. Rev. D **53**, 2442 (1996) [arXiv:hep-ph/9510309].

[54] J. Hisano and D. Nomura, Phys. Rev. D **59**, 116005 (1999) [arXiv:hep-ph/9810479].

[55] I. Masina and C. A. Savoy, Nucl. Phys. B **661**, 365 (2003) [arXiv:hep-ph/0211283].

[56] P. Paradisi, JHEP **0510**, 006 (2005) [arXiv:hep-ph/0505046].

[57] M. Ciuchini, A. Masiero, P. Paradisi, L. Silvestrini, S. K. Vempati and O. Vives, Nucl. Phys. B **783**, 112 (2007) [arXiv:hep-ph/0702144].

[58] G. D. Kribs, E. Poppitz and N. Weiner, Phys. Rev. D **78**, 055010 (2008) [arXiv:0712.2039 [hep-ph]].

[59] G. D. Kribs, A. Martin and T. S. Roy, JHEP **0901**, 023 (2009) [arXiv:0807.4936 [hep-ph]].

[60] P. Fayet, Phys. Lett. B **78**, 417 (1978).

[61] J. Polchinski and L. Susskind, Phys. Rev. D **26**, 3661 (1982).

[62] L. J. Hall and L. Randall, Nucl. Phys. B **352**, 289 (1991).

[63] P. J. Fox, A. E. Nelson and N. Weiner, JHEP **0208**, 035 (2002) [arXiv:hep-ph/0206096].

[64] A. E. Nelson, N. Rius, V. Sanz and M. Unsal, JHEP **0208**, 039 (2002) [arXiv:hep-ph/0206102].

[65] Z. Chacko, P. J. Fox and H. Murayama, Nucl. Phys. B **706**, 53 (2005) [arXiv:hep-ph/0406142].

[66] L. M. Carpenter, P. J. Fox and D. E. Kaplan, arXiv:hep-ph/0503093.

[67] I. Antoniadis, K. Benakli, A. Delgado and M. Quiros, Adv. Stud. Theor. Phys. **2**, 645 (2008) [arXiv:hep-ph/0610265].

[68] J. Hisano, M. Nagai, T. Naganawa and M. Senami, Phys. Lett. B **644**, 256 (2007) [arXiv:hep-ph/0610383].

[69] K. Hsieh, Phys. Rev. D **77**, 015004 (2008) [arXiv:0708.3970 [hep-ph]].

[70] S. Y. Choi, M. Drees, A. Freitas and P. M. Zerwas, Phys. Rev. D **78**, 095007 (2008) [arXiv:0808.2410 [hep-ph]].

[71] S. D. L. Amigo, A. E. Blechman, P. J. Fox and E. Poppitz, JHEP **0901**, 018 (2009) [arXiv:0809.1112 [hep-ph]].

[72] T. Plehn and T. M. P. Tait, J. Phys. G **36**, 075001 (2009) [arXiv:0810.3919 [hep-ph]].

[73] R. Harnik and G. D. Kribs, Phys. Rev. D **79**, 095007 (2009) [arXiv:0810.5557 [hep-ph]].

[74] K. Benakli and M. D. Goodsell, Nucl. Phys. B **816**, 185 (2009) [arXiv:0811.4409 [hep-ph]].

[75] M. Luo and S. Zheng, JHEP **0901**, 004 (2009) [arXiv:0812.4600 [hep-ph]].

[76] G. D. Kribs, A. Martin and T. S. Roy, JHEP **0906**, 042 (2009) [arXiv:0901.4105 [hep-ph]].

[77] A. E. Blechman, Mod. Phys. Lett. A **24**, 633 (2009) [arXiv:0903.2822 [hep-ph]].

[78] A. Kumar, D. Tucker-Smith and N. Weiner, arXiv:0910.2475 [hep-ph].

[79] S. L. Glashow, J. Iliopoulos and L. Maiani, Phys. Rev. D **2**, 1285 (1970).

[80] R. Kitano, M. Koike and Y. Okada, Phys. Rev. D **66**, 096002 (2002) [Erratum-ibid. D **76**, 059902 (2007)] [arXiv:hep-ph/0203110].

[81] V. Cirigliano, R. Kitano, Y. Okada and P. Tuzon, Phys. Rev. D **80**, 013002 (2009) [arXiv:0904.0957 [hep-ph]].

[82] A. De Gouvea, G. F. Giudice, A. Strumia and K. Tobe, Nucl. Phys. B **623**, 395 (2002) [arXiv:hep-ph/0107156].

[83] A. E. Blechman and S. P. Ng, JHEP **0806**, 043 (2008) [arXiv:0803.3811 [hep-ph]].

[84] S. I. Bityukov and N. V. Krasnikov, Phys. Atom. Nucl. **62**, 1213 (1999) [Yad. Fiz. **62**, 1288 (1999)] [arXiv:hep-ph/9712358].

[85] K. Agashe and M. Graesser, Phys. Rev. D **61**, 075008 (2000) [arXiv:hep-ph/9904422].

[86] J. Hisano, R. Kitano and M. M. Nojiri, Phys. Rev. D **65**, 116002 (2002) [arXiv:hep-ph/0202129].

[87] J. Kalinowski, Acta Phys. Polon. B **33**, 2613 (2002) [arXiv:hep-ph/0207051].

[88] F. Deppisch, J. Kalinowski, H. Pas, A. Redelbach and R. Ruckl, arXiv:hep-ph/0401243.

[89] T. Goto, K. Kawagoe and M. M. Nojiri, Phys. Rev. D **70**, 075016 (2004) [Erratum-ibid. D **71**, 059902 (2005)] [arXiv:hep-ph/0406317].

[90] K. Hamaguchi and A. Ibarra, JHEP **0502**, 028 (2005) [arXiv:hep-ph/0412229].

[91] Yu. M. Andreev, S. I. Bityukov, N. V. Krasnikov and A. N. Toropin, Phys. Atom. Nucl. **70**, 1717 (2007) [arXiv:hep-ph/0608176].

[92] Y. Grossman, Y. Nir, J. Thaler, T. Volansky and J. Zupan, Phys. Rev. D **76**, 096006 (2007) [arXiv:0706.1845 [hep-ph]].

[93] J. L. Feng, C. G. Lester, Y. Nir and Y. Shadmi, Phys. Rev. D **77**, 076002 (2008) [arXiv:0712.0674 [hep-ph]].

[94] Y. Nomura, M. Papucci and D. Stolarski, Phys. Rev. D **77**, 075006 (2008) [arXiv:0712.2074 [hep-ph]].

[95] R. Kitano, JHEP **0803**, 023 (2008) [arXiv:0801.3486 [hep-ph]].

[96] B. C. Allanach, J. P. Conlon and C. G. Lester, Phys. Rev. D **77**, 076006 (2008) [arXiv:0801.3666 [hep-ph]].

[97] M. Hirsch, J. W. F. Valle, W. Porod, J. C. Romao and A. Villanova del Moral, Phys. Rev. D **78**, 013006 (2008) [arXiv:0804.4072 [hep-ph]].

[98] S. Kaneko, J. Sato, T. Shimomura, O. Vives and M. Yamanaka, Phys. Rev. D **78**, 116013 (2008) [arXiv:0811.0703 [hep-ph]].

[99] J. Hisano, M. M. Nojiri and W. Sreethawong, JHEP **0906**, 044 (2009) [arXiv:0812.4496 [hep-ph]].

[100] J. L. Feng, I. Galon, D. Sanford, Y. Shadmi and F. Yu, Phys. Rev. D **79**, 116009 (2009) [arXiv:0904.1416 [hep-ph]].

[101] J. L. Feng *et al.*, arXiv:0910.1618 [hep-ph].

[102] A. J. Buras, L. Calibbi and P. Paradisi, arXiv:0912.1309 [hep-ph].

[103] I. Hinchliffe, F. E. Paige, M. D. Shapiro, J. Soderqvist and W. Yao, Phys. Rev. D **55**, 5520 (1997) [arXiv:hep-ph/9610544].

[104] S. Abdullin *et al.* [CMS Collaboration], J. Phys. G **28**, 469 (2002) [arXiv:hep-ph/9806366].

[105] H. Bachacou, I. Hinchliffe and F. E. Paige, Phys. Rev. D **62**, 015009 (2000) [arXiv:hep-ph/9907518].

[106] I. Hinchliffe and F. E. Paige, Phys. Rev. D **61**, 095011 (2000) [arXiv:hep-ph/9907519].

[107] B. C. Allanach, C. G. Lester, M. A. Parker and B. R. Webber, JHEP **0009**, 004 (2000) [arXiv:hep-ph/0007009].

[108] G. Aad *et al.* [The ATLAS Collaboration], arXiv:0901.0512 [hep-ex].

[109] J. Alwall *et al.*, JHEP **0709**, 028 (2007) [arXiv:0706.2334 [hep-ph]].

[110] P. Meade and M. Reece, arXiv:hep-ph/0703031.

[111] G. Burdman, Z. Chacko, H. -S. Goh, R. Harnik, C. A. Krenke, Phys. Rev. **D78**, 075028 (2008). [arXiv:0805.4667 [hep-ph]].

[112] K. Cheung, W. -Y. Keung, T. -C. Yuan, Nucl. Phys. **B811**, 274-287 (2009). [arXiv:0810.1524 [hep-ph]].

[113] R. Harnik, T. Wizansky, Phys. Rev. **D80**, 075015 (2009). [arXiv:0810.3948 [hep-ph]].

[114] H. Cai, H. -C. Cheng, J. Terning, JHEP **0905**, 045 (2009). [arXiv:0812.0843 [hep-ph]].

[115] C. Kilic, T. Okui, R. Sundrum, JHEP **1002**, 018 (2010). [arXiv:0906.0577 [hep-ph]].

[116] S. Chang, M. A. Luty, [arXiv:0906.5013 [hep-ph]].

[117] S. Nussinov and C. Jacoby, arXiv:0907.4932 [hep-ph].

[118] C. Kilic, T. Okui, JHEP **1004**, 128 (2010). [arXiv:1001.4526 [hep-ph]].

[119] L. Carloni and T. Sjostrand, JHEP **1009**, 105 (2010) [arXiv:1006.2911 [hep-ph]].

[120] S. P. Martin, Phys. Rev. **D83**, 035019 (2011). [arXiv:1012.2072 [hep-ph]].

[121] M. J. Strassler, K. M. Zurek, Phys. Lett. **B651**, 374-379 (2007). [hep-ph/0604261].

[122] T. Han, Z. Si, K. M. Zurek, M. J. Strassler, JHEP **0807**, 008 (2008). [arXiv:0712.2041 [hep-ph]].

[123] M. J. Strassler, [arXiv:0806.2385 [hep-ph]].

[124] V. M. Abazov *et al.* [D0 Collaboration], Phys. Rev. Lett. **105**, 211803 (2010). [arXiv:1008.3547 [hep-ex]].

[125] M. Luty, private communication via R. Harnik, who probably prefers that it had remained private.

[126] V. D. Barger, E. W. N. Glover, K. Hikasa, W. Y. Keung, M. G. Olsson, C. J. . Suchyta and X. R. Tata, Phys. Rev. D **35**, 3366 (1987) [Erratum-ibid. D **38**, 1632 (1988)].

[127] B. Guberina, J. H. Kuhn, R. D. Peccei and R. Ruckl, Nucl. Phys. B **174**, 317 (1980).